

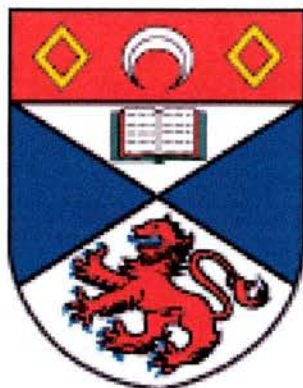
University of St Andrews



Full metadata for this thesis is available in
St Andrews Research Repository
at:

<http://research-repository.st-andrews.ac.uk/>

This thesis is protected by original copyright



LOW AND NEGATIVE THERMAL EXPANSION MATERIALS

A thesis presented for the degree of

Doctor of Philosophy

in the Faculty of Science of the University of St. Andrews

by David A. Woodcock, B.Sc. (Hons.), G.R.S.C.

October 1999

School of Chemistry

St. Andrews



π D510

DECLARATION

I, David Woodcock, hereby certify that this thesis, which is approximately 32000 words in length, has been written by me, that it is the record of work carried out by me and that it has not been submitted in any previous application for a higher degree.

25th October 1999

Signed:

I was admitted as a research student in October 1996 and as a candidate for the degree of Doctor of Philosophy in August 1997; the higher study for which this is a record was carried out in the University of St. Andrews between October 1996 and October 1999

25th October 1999

Signed:

CERTIFICATION

I hereby certify that the candidate has fulfilled the conditions of the Resolution and Regulations appropriate for the degree of Doctor of Philosophy in the University of St. Andrews and that the candidate is qualified to submit this thesis in application for that degree.

25th October 1999

Signature of supervisor:

LIBRARY DECLARATION

In submitting this thesis to the University of St. Andrews I understand that I am giving permission for it to be made available for use in accordance with the regulations of the University Library for the time being in force, subject to any copyright vested in the work not being affected thereby. I also understand that the title and abstract will be published and that a copy of the work may be made and supplied to any bona fide library or research worker.

25th October 1999

Signed:

Abstract

X-ray and neutron powder diffraction have been used to identify new low and negative thermal expansion (NTE) materials and to pinpoint the structural influences on the mechanism of their behaviour. Three main classes of material have been studied: the NZP or Nasicon family, the $\text{Sc}_2(\text{WO}_4)_3$ family and microporous materials.

The NZP phase $\text{NbTi}(\text{PO}_4)_3$, the $\text{Sc}_2(\text{WO}_4)_3$ structure phases $\text{Y}_2(\text{WO}_4)_3$ and $\text{Al}_2(\text{WO}_4)_3$, the pure silica zeolites ITQ-1, ITQ-3, SSZ-23, ITQ-4, ITQ-7, ITQ-9 and chabazite and the aluminophosphate MAPO-17 have all been found to contract on heating. Chabazite has the largest negative coefficient of thermal expansivity known for any material.

The thermal expansion within the NZP system is driven by the expansivity of the “soft” M-O bonds (M = Na, K, Sr etc.). This behaviour has been quantified in terms of rotations and distortions of linked TiO_6 and PO_4 polyhedra, and correlations within the series $\text{MTi}_2(\text{PO}_4)_3$ (M = Li, Na, K), $\text{M}_x\text{Ti}_2(\text{PO}_4)_3$ (M = Na, $\text{Sr}_{1/2}$, $\text{La}_{1/3}$) and $\text{M}_{1/2}\text{Ti}_2(\text{PO}_4)_3$ (M = $\text{Sr}_{1/2}$, $\text{Ba}_{1/2}$, $\text{K}_{1/2}$ *) have been made. The behaviour of these families has been rationalised in terms of the size, occupancy and ordering of the M sites.

Within the $\text{M}_2(\text{WO}_4)_3$ phases a correlation of NTE with the size of the M sites has been found, with $\text{Al}_2(\text{WO}_4)_3$ and $\text{Y}_2(\text{WO}_4)_3$ exhibiting extremes of behaviour. In general, negative thermal expansion in microporous structures appears to be much more widespread than previously thought. Eight of the ten samples studied have shown negative axial thermal expansion and most of these have also shown a volume contraction. A detailed study of the NTE in chabazite has shown that the behaviour is due to a contraction of the Si-O-Si bond angles both between and within the 6-membered rings. The material expanded on cooling, so the thermal contraction was not due to annealing of defects or water loss.

*actual formula $\text{K}_{1/2}\text{Nb}_{1/2}\text{Ti}_{3/2}(\text{PO}_4)_3$

Acknowledgements

The work for this project was undertaken in Dr Phil Lightfoot's laboratory in the University of St. Andrews School of Chemistry. Before presenting my experimental results I would like to extend my thanks to the following people.

Phil for his help, his patience and his red pen, without which my thesis would not be what it is.

Paul Wright for his enthusiastic help with all things microporous.

Susan who had the joy and rapture of teaching me GSAS.

Josie for her support and motivation.

Vinton for teaching me one end of a PC from the other.

Zoe and Martin for their good humour and enthusiasm, not to mention the 17&36.

Humphrey for helping sort the pages.

Luis Villaescusa, Maria-Jose Diaz Cabanas and Miguel Cambor for their willingness to make zeolites on demand.

The Argonne National Laboratory, The Rutherford Appleton Laboratory, and the Institut Laue Langevin for neutron beam time.

Ron Smith, Dennis Engberg, Clemens Ritter, Richard Ibberson, Simine Short and Jim Jorgensen for helping with the neutrons.

All the technical and support staff in the School of Chemistry.

The EPSRC for paying the bills and keeping me in Air Miles.

The Cellar Bar for being there on Fridays.

Contents

Chapter 1: Introduction	1
1.1 The Basis of Thermal Expansion	1
1.2 Applications of Low and Negative Thermal Expansion Materials	2
1.3 Calculating Coefficients of Thermal Expansion	3
1.4 Some Known Low Thermal Expansion Materials	4
1.5 Common Structural Features	6
1.6 Predictions and Calculations	6
1.7 Basis for Thermal Contraction	7
1.8 The Guitar String Analogy (Simple Phonon Modes)	9
1.9 Rocking Polyhedra (Rigid Unit Modes)	10
1.10 Phonon Density of States of ZrW_2O_8	12
1.11 Structure Types With a Two-fold Co-ordination of Oxygens	12
1.12 References	13
Chapter 2: Experimental Techniques and Instruments	15
2.1 X-ray Diffraction	15
2.1.1 Principles of Diffraction	15
2.1.2 Bragg's Law	16
2.1.3 Scattering Factor	17
2.1.4 Structure Factor	17
2.1.5 Temperature Factor	18
2.1.6 STOE Diffractometer and Furnace	19
2.2 Neutron Diffraction	19
2.2.1 Reactor Sources	21
2.2.2 Spallation Sources	21
2.2.3 Institut Laue Langevin, Grenoble	22
2.2.4 D1B	22
2.2.5 D2B	23
2.2.6 The ISIS Facility, Rutherford Appleton Laboratory	23

2.2.7	Polaris	24
2.2.8	HRPD – High Resolution Powder Diffractometer	24
2.2.9	OSIRIS	25
2.3	Rietveld Refinement	26
2.3.1	Goodness of Fit	27
2.3.2	Constraints, Restraints and Damping	28
2.4	References	28
Chapter 3: Materials with the NZP (Nasicon) Structure		29
3.1	Introduction	29
3.1.1	Structure	29
3.1.2	Thermal Expansion Anisotropy	30
3.1.3	Effect of Cation Size	32
3.1.4	The Alamo Model	32
3.1.5	Sample Preparation	34
3.2	A Neutron Powder Diffraction Study of NaTi₂(PO₄)₃ (NaTP) and Sr_{0.5}Ti₂(PO₄)₃ (SrTP)	35
3.2.1	Experimental	35
3.2.2	Results and Discussion	36
3.3	A Neutron Powder Diffraction Study of La_{0.33}Ti₂(PO₄)₃ (LaTP)	38
3.3.1	Experimental	38
3.3.2	Results and Discussion	39
3.3.3	Conclusions	46
3.4	A Neutron Powder Diffraction Study of NbTi(PO₄)₃ (NbTP)	46
3.4.1	Experimental	47
3.4.2	Results and Discussion	47
3.4.3	Conclusions	50
3.5	A Neutron Powder Diffraction Study of Ba_{0.5}Ti₂(PO₄)₃ (BaTP), K_{0.5}Nb_{0.5}Ti_{1.5}(PO₄)₃ (KNTP) and Ca_{0.25}Sr_{0.25}Zr₂(PO₄)₃(CaSrZP)	51
3.5.1	Experimental	51
3.5.2	Results and Discussion	53
3.5.3	Conclusions	60
3.6	A Neutron Powder Diffraction Study of KTi₂(PO₄)₃ (KTP) and	

LiTi ₂ (PO ₄) ₃ (LiTP)	60
3.6.1 Experimental	60
3.6.2 Results and Discussion	62
3.6.3 Conclusions	69
3.7 Overall Conclusion	70
3.8 References	71
3.9 Publications Arising from this Chapter	72
Chapter 4: Materials with the Scandium Tungstate Structure	73
4.1 Introduction	73
4.2 Experimental	75
4.3 Results and Discussion	76
4.4 Conclusion	80
4.5 References	80
4.6 Publications Arising from this Chapter	80
Chapter 5: Microporous Materials	81
5.1 Introduction	81
5.2 Experimental	82
5.3 X-ray Diffraction Study	83
5.3.1 Structure Descriptions	84
5.3.2 Results and Discussion	86
5.3.3 Conclusions (from X-ray Diffraction)	89
5.4 Neutron Diffraction	90
5.4.1 Experimental	91
5.4.2 Results and Discussion	92
5.4.3 Conclusions (Neutron Diffraction Experiments Part One)	99
5.5 Further Neutron Diffraction Experiments	101
5.5.1 Experimental	103
5.5.2 Results and Discussion	104
5.6 Chabazite: A Further Experiment	109
5.7 Overall Conclusion	110

5.8 References	111
5.9 Publications Arising from this Chapter	112
Chapter 6: Studies of $\text{NaTi}_2(\text{PO}_4)_3$ Under Elevated Pressure	113
6.1 Introduction	113
6.2 Experimental	113
6.3 Results and Discussion	114
6.4 Conclusion	118
6.5 References	118
Chapter 7: Conclusions and Further Work	119
7.1 Conclusions	119
7.2 Further Work	120
Appendices	122
Appendix 1: Materials with the NZP (Nasicon) Structure	124
Appendix 2: Materials with the Scandium Tungstate Structure	135
Appendix 3: Microporous Materials	138

Chapter 1: Introduction

The vast majority of materials expand on heating. Some materials, however, do not. Although the chemical bonds within such a material themselves expand normally, due to a structural anomaly the bulk may contract on heating, or expand only slightly. The main aim of this work is to identify the key influences on materials which show either an axial or a volume contraction using the complementary techniques of X-ray and neutron powder diffraction. Although lattice dynamics and molecular modelling studies have enjoyed recent success in predicting thermal contraction, these techniques are beyond the scope of this work. Experimental verification of some of these predictions is provided in some cases. The three main structure types studied have been those with the NZP (Nasicon) structure (Chapter 3), the scandium tungstate structure (Chapter 4) and microporous AlPO_4 's and zeolites (Chapter 5). A more detailed discussion of the literature for each case can be found in their respective chapters.

1.1: The Basis of Thermal Expansion

All solids when heated or cooled undergo reversible dimensional changes on a macroscopic level because of a change in thermal vibrations always present in a crystal - this is thermal expansion or dilatation. The expansion of chemical bonds is due to the asymmetric shape of a typical interatomic potential well (figure 1.1).

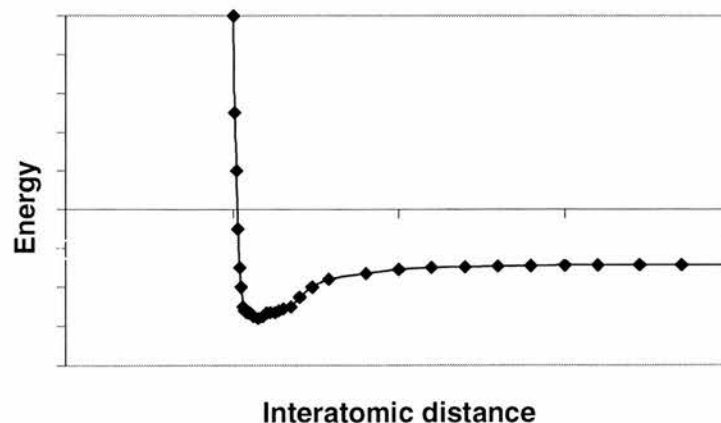


Figure 1.1: Potential energy curve for a typical chemical bond

For a simple diatomic molecule as temperature increases, the higher energy vibrational levels become gradually more populated, resulting in an increased bond length. The entire phonon density of states must be considered as the structure becomes more complicated, but generally the chemical bonds will still expand. However, low or negative thermal expansion of the structure can occur when a structural feature or anomaly makes a contribution which outweighs the simple bond expansion.

1.2: Applications of Low and Negative Thermal Expansion Materials

Low thermal expansion materials have found widespread use in high antithermal shock applications such as cookware for oven to freezer use, electronic devices, heat engine components, automotive applications such as spark plugs and catalyst supports and telescope technology on earth and in space¹.

Negative thermal expansion materials can be used to make zero expansion composites. These are used in high precision optical mirrors – thin metallic layers can be coated on the substrate allowing the optical properties to remain the same should the temperature change. This same effect can be applied to fibre optic systems.

There are also electronic and biomedical applications. It is advantageous to match the thermal expansivity of printed circuit boards to silicon and that of dental fillings to teeth. Negative thermal expansion materials have been envisaged as low temperature sensors².

The key requirements of these materials are that they should have dimensional integrity and not develop microcracks when the operational thermal environment changes. A low bulk expansivity as well as low anisotropy is important for maximum use. These materials are amongst the highest volume advanced ceramic products in use. Cordierite in particular is used in substrates for automotive catalytic converters, insulation for spark plugs, refractory coatings for metals, honeycomb particulate filters for diesel engines and selected parts in gas turbines e.g. heat exchangers³.

1.3: Calculating Coefficients of Thermal Expansion

It is important to be able to quantify any thermal changes in a cell volume or unit cell axis length. This is achieved by calculating the coefficient of linear thermal expansion, which is defined as per unit change in T and is normally expressed as follows, where L is the length of the unit cell axis:

$$\text{CTE } (\alpha) = (L-L_0)/L_0(T-T_0) \quad (1.1)$$

This is an average coefficient of thermal expansion and is different from the differential form (dl/ldt of α). In general α is a function of T and when referring to α of a particular material, the T range in which it was measured should be given. Usually however, an average value is sufficient. Ceramic materials are arbitrarily divided into three classes dependent on their coefficient of thermal expansion.

High expansion group $\alpha > 8 \times 10^{-6} \text{ } ^\circ\text{C}^{-1}$

Intermediate Group $2 < \alpha < 8 \times 10^{-6} \text{ } ^\circ\text{C}^{-1}$

Very Low Expansion Group $\alpha < 2 \times 10^{-6} \text{ } ^\circ\text{C}^{-1}$

This study is generally confined to those materials in the third group, which also includes negative thermal expansion (NTE or contraction) materials.

Not all the materials studied exhibit a linear expansion or contraction. In some cases it is necessary to use a polynomial coefficient in order to fit such curvature. These are calculated using equations 1.2 and 1.3 as follows, where α is the coefficient of thermal expansion: ($\alpha = 1/p \text{ } dp/dT$) and p represents the unit cell parameter at temperature T.

$$p = p_2 T^2 + p_1 T + p_0 \quad (1.2)$$

$$\alpha = \frac{p_1 + 2p_2 T}{p} \quad (1.3)$$

Powder materials can exhibit different bulk CTE's to those of single crystals. A material can have a negative α in one direction and a positive α in another - this is known as anisotropy. When the crystals or grains of a material are joined

together, the bulk thermal expansion will have an average value and in general is reduced as a result of a compensation effect. This anisotropy of α of grains of a single phase polycrystalline ceramic may create internal stresses large enough to generate microcracks, modifying the apparent bulk α .

1.4: Some Known Low Thermal Expansion Materials

Before World War II, most of the low thermal expansion materials used were based on cordierite, zircon and silica glass. In 1948 Hummel⁴ developed the lithium aluminium silicates β -eucryptite and β -spodumene. For the following forty years these formed the basis of low TE applications from dinnerware to space telescope mirror substrates. It was in the 1980's that the NZP series of materials⁵ was developed in response to a demand for a more versatile alternative. The structural basis for the thermal contraction in these materials is the subject for discussion in Chapter 3.

ZrP_2O_7 ⁶ was identified by Sleight et al in 1995. It is a cubic material which exhibits NTE (negative thermal expansion) above its phase transition temperature of 375K. Structural analogues are possible for this AM_2O_7 structure type with substitutions at A (Ti, Zr, Hf, Sn) and M (P, V). NTE occurs in most of these analogues.

ZrW_2O_8 ⁷ has been discovered to contract over the full temperature range below its melting point. Hf can be substituted for Zr and Mo for W to give similar behaviour.

$\text{Sc}_2(\text{WO}_4)_3$ has been known to exhibit negative thermal expansion for some time: its axial contraction was reported by Balashov⁸ in 1975 with $\alpha_a = -5.83$, $\alpha_b = +4.03$, $\alpha_c = -1.91$ and $\alpha_v = -3.64 \times 10^{-6} \text{C}^{-1}$. Since then dilatometric and X-ray diffraction studies have been carried out on many members of the $\text{A}_2\text{M}_3\text{O}_{12}$ family (A = Al, Fe, Sc, Lu, In, Y, M = Mo, W)⁹. Experiments on materials with this structure type are detailed in Chapter 4.

A large number of microporous zeolites and AlPO_4 's have been found to contract, many of which are detailed in this work in Chapter 5.

Other low TE materials include Invar¹⁰, which is an alloy of 65% Fe and 35% Ni, and is virtually zero expansion at room temperature. It is used in television

screens. Ferroelectric relaxors with the perovskite structure such as $\text{Pb}(\text{Mg}_{1/3}\text{Nb}_{2/3})\text{O}_3$ (PMN) and $\text{Pb}(\text{Zn}_{1/3}\text{Nb}_{2/3})\text{O}_3$ (PZN) are also low TE, finding uses in the electroceramics field for their relaxation and super electrostrictive properties (i.e. actuators, micropositioners and multilayer capacitors).

β -cristobalite is one of the natural forms of SiO_2 (along with tridymite and β -quartz) and is also known to be highly resistant to thermal shock. It has been studied by Thomas¹¹ and Saltzberg¹² who have shown that its structure can be stabilised by stuffing Na, Ca, Cu and Sr cations into the structural cavities.

Table 1.1 below shows the coefficients of thermal expansion for some known low and negative thermal expansion materials.

Table 1.1: Some known low and negative TE materials

Material	α ($\times 10^{-6} \text{ } ^\circ\text{C}^{-1}$)	T range ($^\circ\text{C}$)	ref
α -quartz	42	-50-100	13
β -quartz	0	300-627	13
fused quartz	0.5	27	14
SiO_2 faujasite	-4.2	-250-300	15
SiO_2 glass	0.5	25-1000	16
SiO_2 / TiO_2 glass	0.05 to -0.03	25-800	17,18
$\text{NaTi}_2(\text{PO}_4)_3$ (NaTP)	4.2	27-727	19
ZrW_2O_8	-9.1	-273-27	7
ZrMo_2O_8	-5	-273-227	20
ZrV_2O_7	-7.1	127-227	6
$\text{Sc}_2\text{W}_3\text{O}_{12}$	-2.2	-263-177	21
$\text{Lu}_2\text{W}_3\text{O}_{12}$	-6.8	300-627	22
AlPO-17	-11.4	-255-27	23
β -eucryptite	-6.2	25-1000	24
β -spodumene	0.9	25-1000	4
Ice	-5	-218	25
Cordierite	1.4	25-800	3
PMN	1.0	-100-100	26
Invar	0.01	5-30	10

1.5: Common Structural Features

In general there are three types of structural features which are found in most cases of materials exhibiting low or negative TE.

- 1) Strongly bonded polyhedra which are linked in three dimensions, compensating for any changes in bond lengths.
- 2) Open structures with large openings or channels in the structure (i.e. a low packing density as in zeolites), enabling the lattice to absorb the thermal energy in transverse vibrations perpendicular to the bond directions.
- 3) Structures with ferromagnetic or ferroelectric microdomains, the distribution of which changes over a temperature range, thus compensating for dimensional changes caused by increasing thermal energy.

1.6: Predictions and Calculations

Until recently the search for new materials was based on the criteria of an open structure with both a relatively rigid framework and strongly bonded polyhedra. The expansivity would then be tested using either dilatometric or diffraction methods.

Lattice dynamics have been used to predict the expansivity of some materials. This has become possible due to the introduction of several key assumptions which have made the complex calculations involved significantly less expensive of computer processing time. Firstly, the Gruneisen equation²⁷.

$$\alpha_v = \gamma K_o C_v / V \quad (1.4)$$

where α_v is the volume CTE, γ is the Gruneisen constant, K_o is the compressibility, C_v the specific heat capacity at constant volume and V the molar volume. The Gruneisen constant γ is defined as $-d(\ln \nu)/d(\ln V)$, thus in some cases if vibrational modes soften (frequency decreases), as V decreases the Gruneisen parameter becomes negative and contributes to NTE.

Materials with strong bonds have a lower TE which can be assumed to approach zero when the bonds are very strong. The melting point can also be an indicator

of expansivity. For a large range of cubic and close packed materials the product αT_m^{28-31} is constant.

Hazen and Prewitt³² noted that M-O bonds with cations of the same charge had approximately the same α (e.g. divalent, octahedrally co-ordinated cations Fe, Mg, Ni, Mn, Co, Ca, Sr and Ba have an M-O expansivity of approximately $14 \times 10^{-6} \text{ } ^\circ\text{C}^{-1}$). These ideas were extended by Hazen and Finger³³ who proposed an empirical crystal chemical relationship between α and the crystal structure.

$$\alpha = (4.0 \times 10^{-6}) \text{ CN} / (S^2 Z_c Z_a) \quad (1.5)$$

where CN is the co-ordination number of the cation, S the ionicity factor, Z_c the valence of the cation and the valence of the Z_a anion.

However in complex structures the linkage and rotation of the polyhedral network become the determining factor for the bulk TE of the materials, rendering these equations unhelpful. In fact, these equations would predict the same TE for α and β quartz and would not predict the low TE of fused silica, cordierite etc. This is where studies of the crystal structure can offer explanations of thermal contraction, this being the prime motivation behind this work.

Predictions of thermal contraction have been very useful, especially those by Tschaufeser and Parker³⁴ on some zeolites and AlPO_4 's. An experimental verification of these is discussed in Chapter 5.

A "maximum volume network" has been suggested by Sleight³⁵ as another key feature. This can be demonstrated most easily in structures with an M-O-M linkage angle of 180° . This is the lowest energy configuration and the most open form of the structure, maximising cation-cation distances and minimising cation-anion distances. This is also possible if the angle is less than 180° . In a network at maximum volume bending of the M-O-M angle to smaller values is easier than bending it to large values.

1.7: Basis for Thermal Contraction

The basis for the low thermal expansion in the LAS (lithium aluminium silicate) compounds is the unique character of spodumene and eucryptite structures. β -

spodumene has a 3D aluminosilicate framework. $(\text{Si}, \text{Al})\text{O}_4$ tetrahedra form five membered rings connected to common tetrahedra, creating zeolite-like channels. These rings are strained. The thermal energy relieves the strain, increasing the minimum O-T-O angle, moving the oxygens and causing the c axis to expand. As the orientation of the oxygens changes, the a and b axes contract.

β -eucryptite consists of a tetrahedral spiral network which can be compared to the springs of a coil mattress. As it is heated, the spiral is put under stress resulting in contraction.

As mentioned earlier, silica glass has long been known to have low thermal expansivity. However, adding other oxides to SiO_2 glass can change this property. On adding B_2O_3 the TE increases¹⁶, due to the weaker bonds in boric oxide-silica glass as B is surrounded by only three oxygens rather than four as in vitreous silicas. An optimised composition was developed using this effect to make Pyrex. Conversely, addition of TiO_2 ¹⁷⁻¹⁸ has the opposite effect, with some compositions exhibiting small NTE. This is thought to be because TiO_2 forms networks and can occupy the fourfold Si equivalent sites. However an addition of too much TiO_2 (> 10 mole %) can lead to phase separation and a higher TE.

Addition of most oxides to silica glass causes enhanced expansion. The low TE is thought to be due to the transverse vibrations of oxygen atoms. The frequency decreases as the structure shrinks. At present little is understood about the mechanism of low TE in these glasses. Besides, most such glasses exhibit a high TE.

Invar, as mentioned in section 1.4 has low TE at room temperature. This is a thermal expansion anomaly near its Curie temperature. Thermal energy is absorbed into developing magnetic domains within the structure. As the temperature increases, thermal motion is sufficient to overcome the magnetic alignment forces. The system becomes paramagnetic and then continues to expand normally on increasing the temperature. PMN is a ferroelectric material and has a series of phase transitions which occur 50°C above and below room temperature. It is believed that the thermal energy within this system is absorbed in a series of electrostatic rearrangements of the microdomain structure.

Orthorhombic polyethylene has been modelled by Bruno et al³⁶. They have found highly anisotropic thermal expansivity with a contraction of the axis, along

which the carbon chains run continuously and an expansion of both the a and b axes which are perpendicular to the chains. α_a and α_b are an order of magnitude greater than α_c . There is tension within the structure caused by vibrations with components away from the interaction directions which cause a contraction of the polymer chains and which contribute significantly to the expansion perpendicular to the chains.

Other mechanisms can involve a phase change. PbTiO_3 changes from a tetragonal to a cubic form with a decrease in volume³⁷ and the structure of zeolite A³⁸ collapses on heating, also resulting in a lower volume of the unit cell.

There are two main mechanisms due to vibrational modes within a structure. The first is the “guitar string” contraction as in ice which is outlined in section 1.8. ZrW_2O_8 is believed to contract due to the “rocking polyhedra” mechanism as outlined below. The polyhedra rock back and forth with no change in shape as the WO_4 groups are not directly connected to each other.

1.8: The Guitar String Analogy (Simple Phonon Modes)

Phonons are high frequency vibrational modes which interact according to the Gruneisen equation. The process involved may be appreciated using a “guitar string” analogy: the transverse motion of a heavy mass suspended between two strings will tend to pull in the string supports, leading to a contraction of the overall structure (figure 1.2).

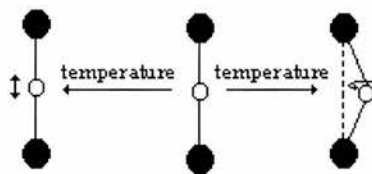


Figure 1.2: The Guitar String explanation for negative thermal expansion. A transverse vibration of the mass at the centre will pull in the string supports.

This tends to apply in the case of single bonds or groups of bonds. These particular phonons are vibrational modes which, when the frequency decreases as the volume decreases, have negative Gruneisen parameters and hence contribute to NTE (equation 1.4). Generally transverse modes are at lower energy than

longitudinal modes and are excited at low temperature. They are therefore only responsible for NTE at very low temperatures. At such temperatures the negative Gruneisen parameter is populated e.g. in ice. It is for this reason that it was previously believed that NTE was enhanced at low temperatures.

β -eucryptite has been studied by Lichtenstein et al³⁹. It has anisotropic TE and the structure is similar to stuffed quartz. There are 1D channels which are occupied by Li^+ ions which compensate for the charge imbalance of the Si^{4+} and Al^{3+} ions. In this case the NTE has been found to be due to the existence of phonons with negative Gruneisen parameters and to the behaviour of the Li^+ ions. The ions become disordered and are the subject of further modelling studies. The authors reported that there was a good correlation between their experimental and modelled data.

1.9: Rocking Polyhedra (Rigid Unit Modes)

For the rocking polyhedra mechanism to occur an open framework structure is required with each framework oxygen co-ordinated to only two metal atoms. The behaviour of the M-O-M linkage angle is crucial. It is weak, having a stiffness of only $1/100^{\text{th}}$ of normal polyhedra, and thus acts as a hinge. If the M-O-M linkage angle is 180° , transverse thermal motion of the oxygen pulls the metal atoms closer together, on the condition that the M-O bonds are strong enough so as not to expand significantly themselves. It was previously believed by Sleight³⁴ that this could only happen over limited temperature ranges not including room temperature. Within ZrW_2O_8 it has been shown that this mechanism can give very strong NTE over a temperature range including RT. Motion in one linkage can fit in with vibrations of the other O atoms in the M-O-M linkages in the network. Each MO_x polyhedron is considered to be rigid or semi-rigid. Rocking of linked polyhedra back and forth creates transverse thermal motion of the M-O-M linkages in a correlated manner. This applies in a so called “flexible network” where polyhedra can easily rotate back and forth with little or no change in shape. Such rocking is called a Rigid Unit Mode (figure 1.3)

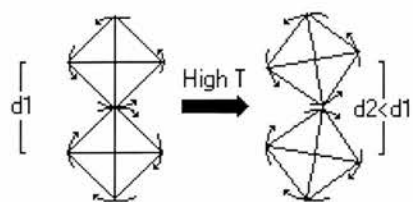


Figure 1.3 As the temperature increases, anharmonic thermal vibration occurs (curved arrows), leading to an atomic displacement, decreasing the M-O-M angle and shortening the M-M distance. The polyhedra remain rigid.

Rigid Unit Modes (RUMs) are rocking motions of polyhedra that do not change shape. Quasi-rigid Unit Modes (qRUMs) are rocking motions where small changes in the polyhedral shape are required. The existence of RUMs and qRUMs is believed to be essential for NTE and were found to be present in ZrW_2O_8 by Pryde et al⁴⁰.

Giddy et al⁴¹ have developed a method for predicting the occurrence of RUMs by computer using the program CRUSH. This program is suitable for both simple and more complex structures. The predictions had previously been done by hand for quartz, which involved testing of special points, symmetry lines and planes of symmetry in reciprocal space. The phonons are predicted to have zero frequency and hence zero energy.

The RUM spectrum of zeolite RHO has been calculated by Bieniok and Hammonds⁴² and compared to experimentally derived structures. They report that studies of RUMs can be used to quantify the flexibility of polyhedral framework structures. Yamahara⁴³ has carried out a molecular dynamics study on MFI (silicalite) SiO_2 . It has also been predicted to show NTE of between -2.3 and $-4.9 \times 10^{-6} \text{ }^\circ\text{C}^{-1}$ depending on the initial structure.

Swainson and Dove⁴⁴ have modelled β -quartz over the temperature range 300-1300 $^\circ\text{C}$. They reported that RUMs exist within the material and have been detected. The RUMs enable an orientational disorder to exist without significant distortion of the SiO_4 tetrahedra. These rotations cause the lattice parameter to be reduced. Although the material does not contract there is a decrease in α until it becomes virtually constant at high temperature.

1.10: Phonon Density of States of ZrW_2O_8

Ernst et al⁴⁵ have calculated the phonon density of states for ZrW_2O_8 and calculated its Gruneisen parameter (the relative change of mode frequency with volume). They used the equation $\gamma = 3\alpha B / C_V$, with C_V being known specific heat data, α the coefficient of thermal expansion and B being $4.8 \times 10^{10} \text{ Nm}^{-2}$ measured from the longitudinal and transverse sound velocity of ZrW_2O_8 at RT. The phonon modes were found using inelastic neutron scattering and those making contributions to the NTE were isolated. As the temperature increased, the modes with high energy were occupied and would normally make a contribution to the TE. However α did not increase so there was no contribution to the TE from the phonons with energy above $\sim 10 \text{ meV}$.

1.11: Structure Types With a Two-fold Co-ordination of Oxygens

As mentioned above a twofold co-ordination of the oxygens is necessary for the rocking polyhedra and hence NTE to occur. There are several structure types where this is possible, although not all of these actually show NTE.

With corner sharing octahedra only – AO_3 e.g. ReO_3

With corner sharing tetrahedra only – MO_2 e.g. SiO_2

With both corner sharing octahedra and tetrahedra – AM_2O_7 , $\text{A}_2\text{M}_3\text{O}_{12}$, AMO_5 (e.g. NbOPO_4).

In AM_2O_7 e.g. ZrV_2O_7 , the NTE is enhanced with a larger unit cell edge. Rocking motion of the tetrahedra and octahedra cannot occur without changes in their shape. As the polyhedra become larger they can change shape more easily as the anion-anion distances increase.

Examples of $\text{A}_2\text{M}_3\text{O}_{12}$ are $\text{NbTiP}_3\text{O}_{12}$ discussed in Chapter 3, and $\text{Sc}_2\text{W}_3\text{O}_{12}$ discussed in Chapter 4. As in cubic AM_2O_7 the coupled rocking cannot occur unless the polyhedra change shape while rocking. Again a large cation will give a larger unit cell and stronger NTE.

1.12: References

- 1) R. Roy, D.K. Agrawal and H.A. McKinstry: *Annu. Rev. Sci.* 1989, **19**:59
- 2) J.S. O. Evans, *J. Chem. Soc. Dalton Trans.*, 1999, 3317
- 3) M.F. Hochella Jr. and G.E. Brown, *J. Amer. Ceram. Soc.*, 1986, **69**, 13
- 4) F.A. Hummel, *Footprints*, 1948 **20**, 3
- 5) J. P. Boilot, J. P. Salanie, G. Desplanches and D. Le Potier, *Mater. Res. Bull.*, 1979, **14**, 1469
- 6) V. Korthuis, N. Khosrovani, A. W. Sleight, N. Roberts, R. Dupree and W. W. Warren, *Chem. Mater.*, 1995, **7**, 412.
- 7) T.A. Mary, J.S.O. Evans, T. Vogt and A.W. Sleight, *Science*, 1996, **277**, 90
- 8) V.A. Balashov, G.I. Vorona, A.A. Maier and O.P. Proshina, *Inorg. Mater.*, 1975, **11**, 1469
- 9) J.S.O. Evans, T.A. Mary, and A.W. Sleight, *J. Solid State Chem.*, 1997, **133**, 580
- 10) W.F. Schlosser, G. M. Graham and P.P.M. Meincke, *J. Phys. Chem. Solids*, 1971, **32**, 927
- 11) E.S. Thomas, J.G. Thompson, R.L. Withers, M. Sterns, Y. Xiao, R.J. Kirkpatrick, *J. Am. Ceram. Soc.*, 1994, **77**, 49
- 12) M.A. Saltzberg, S.L. Bors, H. Bergna and S.C. Winchester, *J. Am. Ceram. Soc.*, 1992, **75**, 89
- 13) D. Taylor, *Br. Ceram. Trans. J.*, 1984, **83**, 129
- 14) T. H. K. Barron, J.G. Collins and G.K. White, *Adv. Phys.*, 1980, **29**, 609
- 15) M. P. Attfield and A. W. Sleight, *Chem. Commun.*, 1998, 601
- 16) J. Bischof, C.S. Robinson Jr and B.E. Warren, *J. Am. Ceram. Soc.*, 1939, **2**, 180
- 17) M. E. Nordberg, *U.S. Patent No. 2326059*, 1943
- 18) K. Kamiya and S. Sakka, *J. Non-Cryst. Solids*, 1982, **52**, 357
- 19) D. Taylor, *Br. Ceram. Trans. J.*, 1991, **90**, 64
- 20) C. Lind, A.P. Wilkinson, Z. Hu, S. Short and J.D. Jorgensen, *Chem. Mater.*, 1998, **10**, 2335
- 21) J. S. O. Evans, T. A. Mary and A. W. Sleight, *J. Solid State Chem.*, 1998, **137**, 148
- 22) P. M. Forster, A. Yokochi and A. W. Sleight, *J. Solid State Chem.*, 1998, **140**, 157
- 23) M. P. Attfield and A. W. Sleight, *Chem. Mater.*, 1998, **10**, 2013

- 24) F. A. Hummel, *J. Am. Ceram. Soc.*, 1951, **34**, 235
- 25) K. Rottger, A. Endriss, J. Ihringer, S. Doyle and W. F. Kuhs, *Acta Crystallogr., Sect.B.*, 1994, **50**, 644
- 26) G.A. Smolenskii, V.A. Isupov, A.I. Agranovskaya and N.N. Krainik, *Sov. Phys. – Solid State*, 1961, **2**, 2584
- 27) E. Gruneisen, *Handb. Phys.*, 1926, **10**, 1
- 28) L.G. Van Uitert, H. M. O’Bryan, M.E. Lines, H.J. Guggenheim and G. Zydzik, *Mater. Res. Bull.*, 1977, **12**, 261
- 29) L.G. Van Uitert, H. M. O’Bryan, M.E. Lines, H.J. Guggenheim and G. Zydzik, *Mater. Res. Bull.*, 1977, **12**, 307
- 30) L.G. Van Uitert, *Mater. Res. Bull.*, 1977, **12**, 315
- 31) L.G. Van Uitert, *J. Appl. Phys.*, 1979, **50**, 8052
- 32) R.M. Hazen and C.T. Prewitt, *Am. Mineral.* 1977, **62**, 309
- 33) R.M. Hazen and L.W. Finger, *Comparative Crystal Chemistry*, 1981, New York, Wiley, pp115
- 34) P. Tschaufeser and S. C. Parker, *J. Phys. Chem.*, 1995, **99**, 10609
- 35) A.W. Sleight, *Inorg. Chem.*, 1998, **37**, 2854
- 36) J.A.O. Bruno, N.L. Allan, T.H.K. Barron and A.D.Turner, *Phys. Rev. B.*, 1998, **58**, 13, 8416
- 37) G.A. Rossetti, J.P. Cline and A. Navrotsky, *J. Mater. Res.*, 1998, **13**, 3197
- 38) A. Colantuano, S. Dal Vecchio, G. Mascolo and M. Pansini, *Thermochimica Acta*, 1997, **29**, 659
- 39) A. I. Lichtenstein, R.O. Jones, H. Xu and P.J. Heaney, *Phys. Rev. B.*, 1998, **58**, 10, 6219
- 40) A.K.A. Pryde, K. D. Hammonds, M.T. Dove, V. Heine, J.D. Gale and M.C. Warren, *Phase Transitions*, 1997, **61**, 141
- 41) A.P. Giddy, M.T. Dove, G.S. Pawley and V. Heine, *Acta. Cryst A.*, 1993, **A49**, 697
- 42) A. Bieniok and K. D. Hammonds, *Microporous Mesoporous Mater.*, 1998, **25**, 193
- 43) K. Yamahara, K. Okazaki and K. Kawamura, *Catalysis Today*, 1995, **23**, 397
- 44) I. P. Swainson and M. T. Dove, *Phys. Chem. Minerals*, 1995, **22**, 61
- 45) G. Ernst, C. Broholm, G.R. Kowach and A. P. Ramirez, *Nature (London)*, 1998, **396**, 147

Chapter 2: Experimental Techniques and Instruments

This chapter is concerned with the techniques of powder X-ray and neutron diffraction which have been used to determine the structure and thermal expansivity of all the materials studied. In general powder X-ray diffraction was used in-house to determine the behaviour of unit cell parameters only and powder neutron diffraction was used to obtain precise structural information. This chapter will outline the theory behind the techniques and the characteristics and limitations of the diffractometers used. Details of sample preparation can be found in subsequent chapters.

2.1: X-ray Diffraction

The fact that X-rays are diffracted by crystals is the basis for this experimental technique which underpins a large part of solid state and crystal chemistry. The diffractogram produced is a characteristic pattern of the crystal structure¹.

2.1.1: Principles of Diffraction

Figure 2.1 overleaf shows diffraction from a point source. X-rays originating from the point source are propagated through space as a series of electromagnetic waves, radiating from the point as a concentric series of sinusoidal crests and troughs. In the diagram the crests are represented as rings. When the waves reach the disc, they are diffracted, but only if the wavelength of the radiation is of the same order as the scatterer. This is the case for X-rays and atomic spacings. On the right of the disc the diffracted waves recombine, exhibiting both constructive and destructive interference. The interference is dependent on both the wavelength of the radiation and the diameter of the disc.

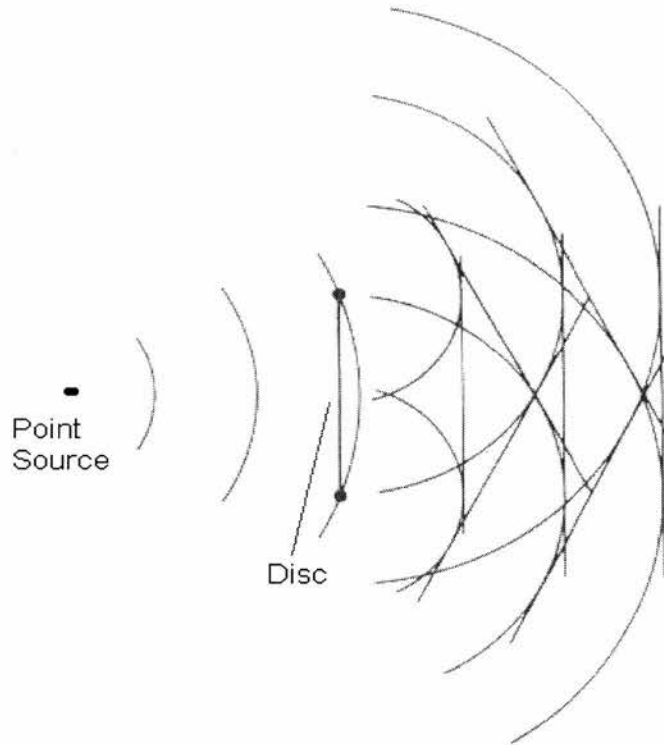


Figure 2.1 : Diffraction of light from a point source

2.1.2: Bragg's Law

Scattering from a crystal can be described in terms of diffraction from a set of lattice planes, each acting as a semi-transparent mirror. Some X-rays are reflected off a plane with the angle of incidence equal to the angle of reflection, but the rest are transmitted to be successfully reflected by succeeding planes. The derivation is shown below.

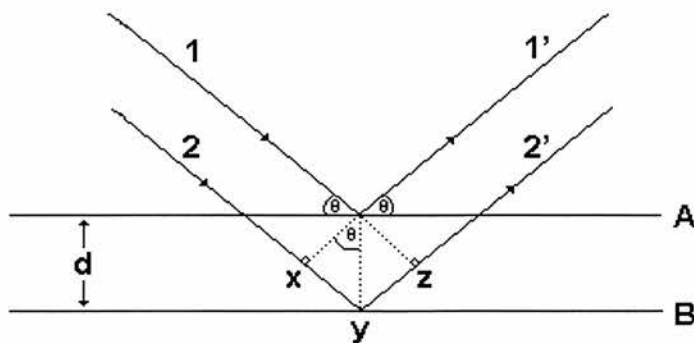


Figure 2.2: Derivation of Bragg's Law

The difference in “path” between wave 1’ and 2’ is equal to $xy + yz = 2d \sin\theta$. If it is a multiple of λ then the reflected beams are in phase and interfere constructively. Bragg’s Law (equation 2.1) is satisfied.

$$n\lambda = 2d \sin\theta \quad (2.1)$$

At angles of incidence other than the Bragg angle, reflected beams are out of phase and destructive interference or cancellation occurs. Since X-rays penetrate deeply, reaching thousands of planes in real crystals, Bragg’s Law imposes a stringent condition on the angles at which reflection can occur. Away from this angle, cancellation is complete.

It is these observations which can be used in the analysis of crystals and powders which have regular packing and long range order. Most of the useful peaks in an X-ray pattern occur between 5° and $80^\circ 2\theta$. The d spacings of the peaks may be calculated from Bragg’s Law.

The pattern obtained has three main features: d -spacings, intensities and peak shapes, all of which give information on the structure. Together, they make up a characteristic fingerprint of the sample, giving information on the size and shape of the unit cell and the atomic number and position of the atoms in the cell.

2.1.3: Scattering Factor

X-rays are scattered by their interactions with atomic electrons and interference takes place between X-rays scattered from different parts of the atom. As a consequence, scattering power or scattering factor f_x decreases with increasing scattering angle 2θ resulting in a tail off of intensities on a diffraction pattern.

At $\sin \theta/\lambda = 0$, f_x is proportional to atomic number and is therefore very small for light atoms such as hydrogen or lithium, giving rise to a difficulty in detection. The diffraction patterns will tend to be dominated by heavy atoms, which are more powerful scatterers.

2.1.4: Structure Factor

Determination of the crystal structure requires a more complicated analysis than the simple Bragg law. If the unit cell contains several atoms with scattering

factors f_i and co-ordinates (x_i, y_i, z_i) the overall amplitude of a wave diffracted by the hkl planes is as below (equation 2.2).

$$F_{hkl} = \sum_i f_i \exp -2\pi(hx_i + ky_i + lz_i) \quad (2.2)$$

The sum is over all the atoms in the unit cell. F_{hkl} is the structure factor and $|F_{hkl}|^2$ is proportional to the intensity of reflections from the hkl planes. The structure of the unit cell is contained in the structure factor because it depends on the atoms present through the scattering factor, f_i , and on their locations (x_i, y_i, z_i) . The electron density $\rho(xyz)$ can be constructed using equation 2.3 below as the structure factors for all the reflections can be derived from their intensities.

$$\rho(xyz) = \sum_{hkl} F_{hkl} e^{-2\pi i(hx + ky + lz)} \quad (2.3)$$

2.1.5: Temperature Factor

Atoms within crystal structures tend not to remain still: if disturbed they oscillate as they try to return to an energy minimum. These oscillations modify their electron density distribution and hence the nature of their scattering. The temperature factor is a means of correcting the measured scattering for these oscillations. It is directly dependent on temperature and inversely dependent on both atomic mass and chemical bond forces. In its simplest case (although not generally in reality) the temperature factor is isotropic i.e. the thermal motion of the atom has spherical symmetry and is defined as B , the atomic temperature factor (equation 2.4) where U is the square mean shift of the atom with respect to its position of equilibrium.

$$B = 8\pi^2 U(\text{\AA})^2 \quad (2.4)$$

The majority of temperature factors quoted in this work are quoted as U_{iso} . In general though, an atom is not free to vibrate equally in all directions and therefore its motion must be described in three dimensions using thermal ellipsoids. This is the anisotropic temperature factor and is derived from the Debye-Waller factor, $q(r^*)$, which in turn is the Fourier transform of the electron density corresponding to the thermally agitated atom:

$$[q(r^*) = \exp [-2\pi^2 (U^*_{11}x^{*2} + U^*_{22}y^{*2} + U^*_{33}z^{*2} + 2 U^*_{12}x^*y^* + 2 U^*_{13}x^*z^* + 2 U^*_{23}y^*z^*)]] \quad (2.5)$$

The six parameters U_{ij} define the orientation of the thermal ellipsoid with respect to the crystallographic axes and the lengths of the three ellipsoid axes.

2.1.6: STOE diffractometer and furnace

In-house structural characterisation was carried out on a STOE STADI-P powder diffractometer using monochromatic $\text{CuK}_{\alpha 1}$ radiation ($\lambda = 1.54056\text{\AA}$). The X-rays are generated by bombarding the copper target with high-energy electrons. These incoming electrons have sufficient energy to reach some of the inner shell (Cu 1s) electrons. A collision expels an electron, and an electron of higher energy drops into the vacancy, emitting the energy as an X-ray photon. The transition energies have fixed values and so a few, high intensity sharp peaks appear in the continuum of radiation generated from the incoming electrons decelerating. In copper the 2p-1s transition, called $\text{K}\alpha$ has a wavelength of 1.5418\AA and the 3p-1s transition $\text{K}\beta$ 1.3922\AA . It is usually $\text{K}_{\alpha 1}$ which is used in diffraction experiments. Other wavelengths than $\text{K}_{\alpha 1}$ are removed using a monochromator. The beam operates in transmission mode and is defined by a collimator. The STOE diffractometer has a moving detector, set to scan over a range of 2θ values at a constant angular velocity.

A furnace attachment was available using a graphite element which allowed high temperature studies of samples ($\text{RT} < T < 950^\circ\text{C}$), although usually data was not collected above 600°C for ceramic materials and 500°C for microporous materials. Long acquisition times were required due to the necessity of mounting the samples in a quartz capillary, allowing only a small volume of sample to be used. This was a particular issue for low scattering microporous materials. The STOE diffractometer was therefore only used for studies of the behaviour of unit cell parameters vs. temperature rather than full structural characterisations vs. temperature.

2.2: Neutron Diffraction

Neutrons, like X-rays have wavelengths similar to atomic spacings, thus permitting diffraction measurements to be performed. They scatter from materials via interaction with the nucleus rather than the electron cloud. This means that the neutron scattering length, b , of an atom is not strongly related to

its atomic number, unlike the cases of X-rays and electron scattering. This has three advantages:

- i) It is easier to see light atoms, such as O, in the presence of heavier ones. This is particularly relevant in our studies where accurate determination of the positions of the O atoms is essential to fully understand the mechanism of low and negative thermal expansivity.
- ii) Neighbouring elements in the Periodic Table can have very different scattering cross sections and can be distinguished, in particular those in the first Transition Series.
- iii) The nuclear dependence of scattering allows isotopes of the same element to have substantially different scattering lengths for neutrons. Isotopic substitution can thus be examined.

Neutrons are a highly penetrating probe, allowing the investigation of the interior of materials. This makes the use of complex sample environments (e.g. cryostats, furnaces and pressure cells) routine, and enables the measurement of bulk processes under realistic conditions. A beam energy of 40meV for a wavelength of 1.5Å c.f. 8keV for Cu K α radiation means that radiation damage is much less likely. The low absorption cross-section allows the use of furnaces and cryostats, and there is no angular dependence of peak intensities as in X-ray diffraction. This is because the scattering power does not fall over the range of angles as neutrons interact with the nucleus (section 2.1.3).

The disadvantages of the method are its huge expense (large facilities have high running and maintenance costs) therefore accessibility to experimental facilities is severely limited and that large samples are required (the beams are of lower intensity and the scattering factors are lower).

There are two types of neutron generation: reactor sources and spallation sources. Both have been used in this study, and each type has its own characteristics.

2.2.1: Reactor Sources

Neutrons can be produced in nuclear reactors. However, these are known as fast neutrons and are of too high an energy to be used in diffraction experiments. They must first be retarded by collisions in a moderator of heavy water or graphite to become thermal neutrons. Such a neutron would then be diffracted by a monochromator (usually a single crystal of Ge, Ca, Zn or Pb) to select the correct wavelength before reaching the sample where it would be diffracted in the same manner as an X-ray. A continuous beam of neutrons is produced and the diffracted intensities measured by sweeping a counter through a range of scattering angles. This is a fixed wavelength (angle dispersive) experiment.

2.2.2: Spallation Sources

Neutrons can also be produced in a pulsed manner by spallation. High energy protons (~800MeV) strike a target such as uranium or tungsten, releasing several tens of neutrons per proton. Higher fluxes are produced than those in reactors, as the pulsed flux is only present for a short time making heat removal much easier. Neutrons with a range of wavelengths are produced as in a reactor source but a monochromator is not used to select one specific wavelength. Instead the whole range of neutrons reach the sample. The detector is fixed and the diffraction pattern collected by a time-of-flight (energy-dispersive) method. For a given reflection the Bragg condition is satisfied at a given wavelength rather than an angle. Results from successive pulses are accumulated and summed until the quantity is sufficient for analysis. This simultaneous collection of the whole diffraction pattern is an advantage of time-of-flight powder methods and is thanks to the different λ neutrons all being diffracted simultaneously. A further advantage of this method is that the fixed detector allows pressure cells and furnaces with only a small window.

2.2.3: Institut Laue Langevin, Grenoble

The Institut Laue-Langevin contains a high flux reactor source. A plan of the instruments available is shown below, the two instruments being used by us being D1B and D2B.

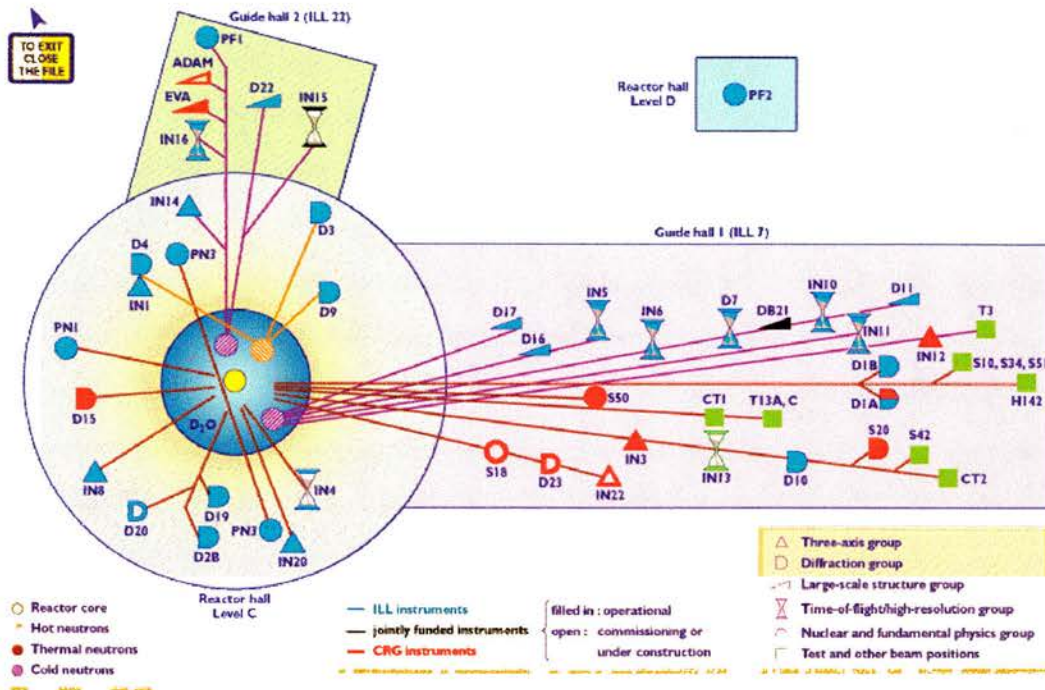


Figure 2.3: The instruments at ILL

2.2.4: D1B

D1B is a two-axis spectrometer dedicated to diffraction experiments requesting a high neutron flux. Both its high flux (at $\lambda = 2.52 \text{ \AA}$) and its large multidetector allow a very fast acquisition time. Our experiments on samples with the NASICON structure (Chapter 3) were able to be run with an acquisition time of around ten minutes at each temperature, whilst still having sufficient statistics for full structural refinements. This resulted in measurements being possible at a much larger number of temperatures. However, these experiments were restricted to a limited d-spacing range.

2.2.5: D2B

D2B is a very high resolution 2 axis diffractometer. We were able to use this diffractometer for full structural refinements of materials with both the NASICON and scandium tungstate structure. High temperature studies used a niobium lined furnace and samples placed in a niobium can, which required excluding 6-7 peaks from each diffraction pattern.

2.2.6: The ISIS Facility, Rutherford Appleton Laboratory

The ISIS facility is the major resource at the Rutherford Appleton Laboratory near Oxford, UK. It is a spallation source generating neutrons, muons and neutrinos for condensed matter research in physics, chemistry, materials science, geology, engineering and biology. A plan of the instruments available is shown below, the main instruments used by us being Osiris, Polaris and HRPD, all of which are discussed later. The long path length for HRPD, which has significant resolution effects, can be clearly seen.

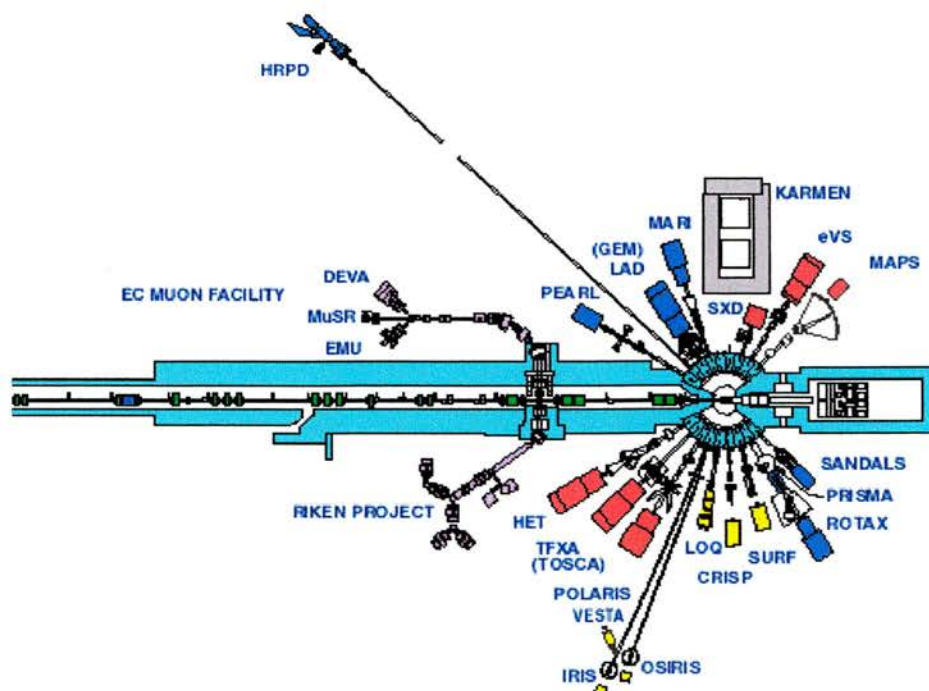


Figure 2.4: Plan of the instruments at the Rutherford Appleton Laboratory

2.2.7: Polaris

Polaris was used for both variable temperature and pressure studies on materials with the NASICON structure. It is a medium resolution, high intensity instrument allowing characterisation of very small amounts of sample ($\sim 1\text{mm}^3$) and very short acquisition times. Its small sample requirement makes collection of data at very high pressure possible.

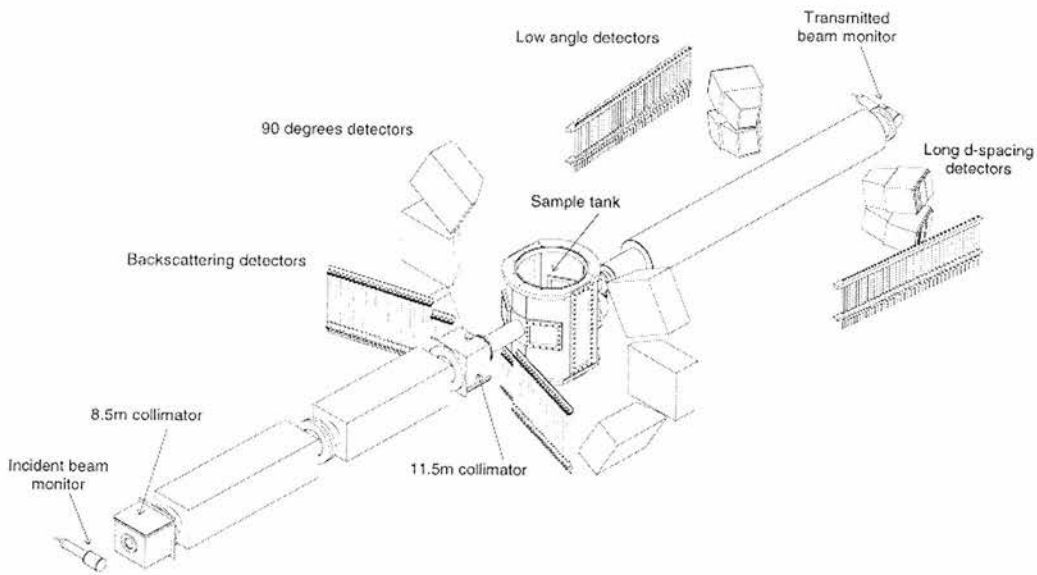


Figure 2.5 – The Polaris Diffractometer

2.2.8: HRPD – High Resolution Powder Diffractometer

HRPD was used for studies of materials with the NASICON structure. It is the highest resolution neutron powder diffractometer in the world, making it particularly effective for studies of subtle structural details. From all of our studies, this diffractometer gave us the highest precision results.

HRPD works on a time-of-flight principle as explained in section 2.2.2. The resolution, $\Delta d/d$, is a function of the spread in the Bragg reflection for a given d-spacing and is probably the most important factor in defining diffractometer quality. There are three contributions to uncertainty in the resolution: a timing

uncertainty, ΔT ; an angular uncertainty, $\Delta\theta$ and a flight path uncertainty, ΔL . Their relationship is shown in equation 2.6 below.

$$R(d) = \Delta d/d = [\Delta\theta^2 \cot^2\theta + (\Delta t/t)^2 + (\Delta L/L)^2]^{1/2} \quad (2.6)$$

HRPD has been designed specifically to minimise the errors as much as possible. The backscattering detector situated at 168° to the beam, minimises the $\Delta\theta^2 \cot^2\theta$ term. The data from this detector, which is one of three, was the principal data used by us in our studies.

Both the timing uncertainty and flight path uncertainty are minimised by increasing the path length to 95m.

2.2.9: OSIRIS

OSIRIS was used for all of our neutron diffraction studies of microporous materials. It is currently scheduled for 50% use as a large d-spacing diffractometer and is being developed for polarisation and spectrometry.

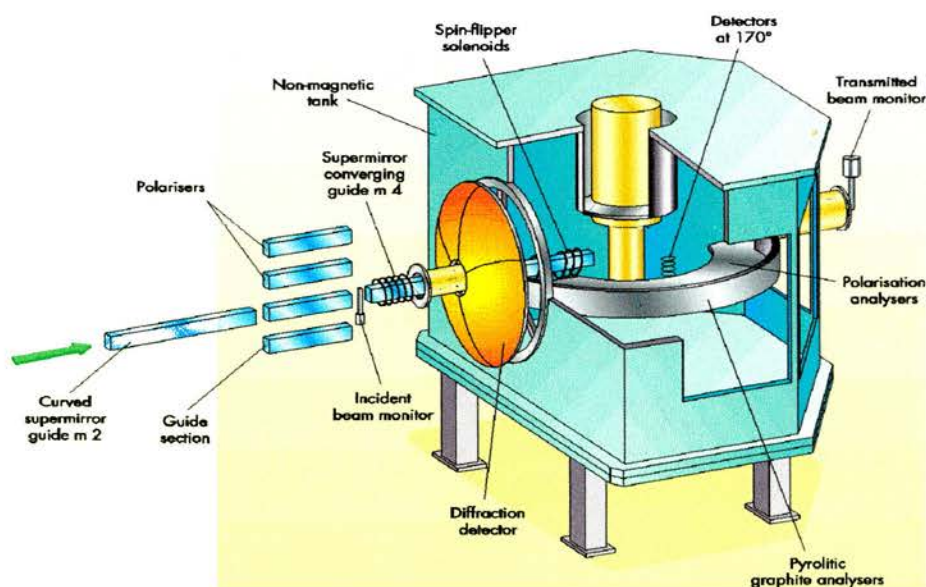


Figure 2.6: The OSIRIS instrument at ISIS

2.3: Rietveld Refinement

An X-ray diffraction experiment on a single crystal would commonly be used to solve its structure. A preliminary examination would establish its perfection and determine lattice parameters and symmetry information. Collection of individual intensities of peaks leads to determination of accurate atomic positions (the intensities are dependent on electron density $\rho(xyz)$, equation 2.3, as before).

$$\rho(xyz) = \sum_{hkl} F_{hkl} e^{-2\pi i(hx + ky + lz)} \quad (2.3)$$

Extending this technique to powders becomes much harder. It can be fine for simple structures, but in low symmetry systems there is an overlap of Bragg reflections.

Rietveld has devised a method where rather than split the pattern into individual peak intensities; the pattern is treated as a whole². Accurate determination of atomic positions from powder X-ray and neutron diffraction data becomes possible, by a refinement of the structure. A starting model is entered and the powder pattern for this model calculated and compared to the powder pattern observed from the experimental data. Equation 2.7 shows the function minimised and equation 2.8 the equivalent minimised for single crystal data.

$$M = w(y_o - y_c)^2 \quad (2.7)$$

$$D = w(|F_o| - |F_c|)^2 \quad (2.8)$$

The difference between the observed and calculated powder pattern is minimised by using a least squares method to alter the structural parameters. A key feature is feedback during refinement between improved knowledge of the structure and improved allocation of observed intensity to partially overlapping individual Bragg reflections. For the refinement to work, a good starting model is needed and within this model, the following parameters to be refined: atom positions, thermal parameters, site occupancy, background, lattice parameters and peak shape. Within our laboratory the program used is GSAS³, the Generalised Structure Analysis System. This works with both X-ray and neutron data from both angle dispersive (fixed λ) and energy dispersive (Time-of-flight) data.

2.3.1: Goodness of Fit

There are several indicators of the goodness of fit⁴. These are the profile difference plot, χ^2 and the R factors R_p and R_{wp} . Once the refined and experimental data converge these are quoted.

The difference plot, such as figure 2.7 below is simply a line showing the difference between the observed and calculated diffraction patterns. A good fit would show little difference.

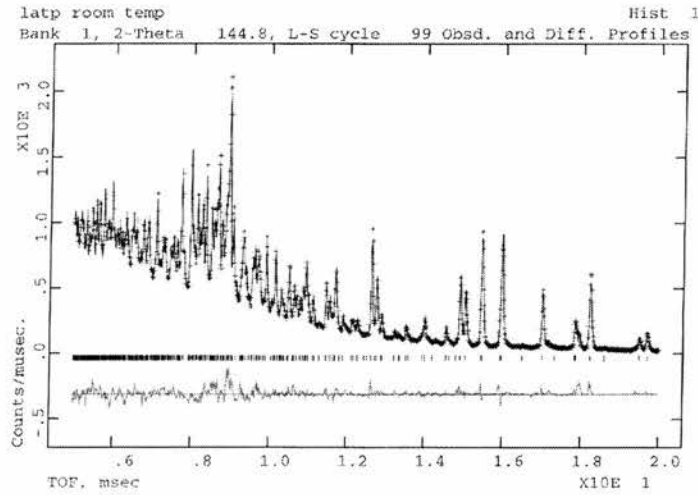


Figure 2.7: Typical neutron Rietveld difference plot.

The line below shows the goodness of fit.

The R factor R_p is defined in equation 2.9 below, as where y_{io} is the observed intensity at each x value and y_{ic} the calculated intensity.

$$R_p = \frac{\sum |y_{io} - y_{ic}|}{\sum y_{io}} \quad (2.9)$$

R_{wp} (equation 2.10) assigns a weighting w_i (equation 2.11), where σ_{ip} is the standard deviation associated with the peak (usually based on counting statistics) and σ_{ib} is that associated with the background intensity y_{ib} .

$$R_{wp} = \left[\frac{\sum w_i (y_{io} - y_{ic})^2}{\sum w_i y_{io}^2} \right]^{1/2} \quad (2.10)$$

$$(w_i)^{-1} = \sigma_i^2 = \sigma_{ip}^2 + \sigma_{ib}^2 \quad (2.11)$$

Both R_p and R_{wp} should be as low as possible. χ is the ratio between the weighted R factor R_{wp} and expected R factor R_e (equation 2.12)

$$R_e = \left[\frac{N-P}{\sum w_i y_{io}^2} \right]^{1/2} \quad (2.12)$$

If $\chi > 1.5$ this is an indicator of a poor model or a false minimum and if it is less than 1 there are too many parameters in the calculation compared to the quality

of data available. Generally it is χ^2 which is quoted and values of below seven are considered to be acceptable.

2.3.2: Constraints, Restraints and Damping

It is often the case that a refinement does not converge successfully at a first attempt. Either divergence or convergence at a false minimum can occur. There are several solutions to this problem.

The first is to damp a particular parameter which is proving unstable, which will allow smaller incremental steps towards the minimum. The second is to introduce soft constraints which would hold e.g. a particular range of bond lengths close to a theoretical value to give a more realistic result.

A rigid body refinement would require a particular cluster of atoms to librate as a fixed unit rather than being able to adopt a minimum energy configuration. This involves defining a special co-ordinate system to which the atom positions can be specified and rigid body motion tensors defined. Three positional parameters define the origin of the special co-ordinate system relative to the origin of the unit cell and three more define the orientation with respect to the the crystallographic axes. Expressions for thermal parameters can also be defined using a TLS matrix, but this was beyond the scope of the refinements carried out in this work.

Both rigid body and soft constrained models offer a large reduction in the numbers of adjustable parameters resulting in a great simplification of the refinement.

2.4: References

- 1) W. Clegg, *Crystal Structure Determination*, 1998, New York, Oxford University Press.
- 2) H. M. Rietveld, *Acta. Crystallogr.*, 1966, 21, A228
- 3) A.C. Larson, R.B. Von Dreele; Los Alamos National Laboratory Report No. LA-UR-86-748, 1987
- 4) R. A. Young, *The Rietveld Method*, 1993, New York, Oxford University Press.

Chapter 3: Materials with the NZP (Nasicon) Structure

3.1 Introduction

By far the most widely studied of the low thermal expansion structure types have been the Nasicon or NZP family, based on the $\text{NaZr}_2(\text{PO}_4)_3$ structure. There are several interesting features of the thermal expansion in this system. The first is the thermal expansion anisotropy, detailed in section 3.1.2 between members of the family crystallising in R-3 and R-3c – they show an opposite anisotropy. The second is that substitution of different cations for Na can result in vastly different TE behaviour. The work in this chapter constitutes the largest single part of the work undertaken in this thesis and has been broken down into five different experiments which are each considered separately, and the conclusions summarised at the end of the chapter.

They are all neutron powder diffraction studies and are of the materials listed below:

Section 3.2: $\text{NaTi}_2(\text{PO}_4)_3$ (NaTP) and $\text{Sr}_{0.5}\text{Ti}_2(\text{PO}_4)_3$ (SrTP) – anisotropy analysis

Section 3.3: $\text{La}_{0.33}\text{Ti}_2(\text{PO}_4)_3$ (LaTP) – analysis of effect of partial occupancy of MI sites

Section 3.4: $\text{NbTi}(\text{PO}_4)_3$ (NbTP) - analysis of effect of zero occupancy of MI sites

Section 3.5: $\text{Ba}_{0.5}\text{Ti}_2(\text{PO}_4)_3$ (BaTP), $\text{K}_{0.5}\text{Nb}_{0.5}\text{Ti}_{1.5}(\text{PO}_4)_3$ (KNTP) and $\text{Ca}_{0.25}\text{Sr}_{0.25}\text{Zr}_2(\text{PO}_4)_3$ (CaSrZP) – analysis of effect of disorder of cations and vacancies across MI sites

Section 3.6: $\text{KTi}_2(\text{PO}_4)_3$ (KTP) and $\text{LiTi}_2(\text{PO}_4)_3$ (LiTP) – effect of cation size on thermal expansion

3.1.1 Structure

The NZP structure is chemically the most versatile of all the currently known low and negative thermal expansion phases. From the basic $\text{NaZr}_2(\text{PO}_4)_3$ unit, substitutions are possible at the Na site ($A = \text{Li}, \text{K}, \text{Ca}_{0.5}, \text{La}_{0.33}$ etc.), at the Zr site ($M = \text{Ti}, \text{Hf}$) and at the P site ($X = \text{Si}, \text{S}$). Such substitutions allow tailoring of thermal expansion properties¹. NZP crystallises in the rhombohedral space group R-3c, having only one crystallographically distinct Na site. It forms a three-dimensional lattice consisting of corner sharing ZrO_6 octahedra and PO_4

tetrahedra forming a $[\text{Zr}_2(\text{PO}_4)_3]^-$ unit which aligns in chains up the c axis. Na^+ cations fill interstitial trigonal anti-prismatic MI sites within these chains. Figure 3.1 shows the Ti substituted phase.

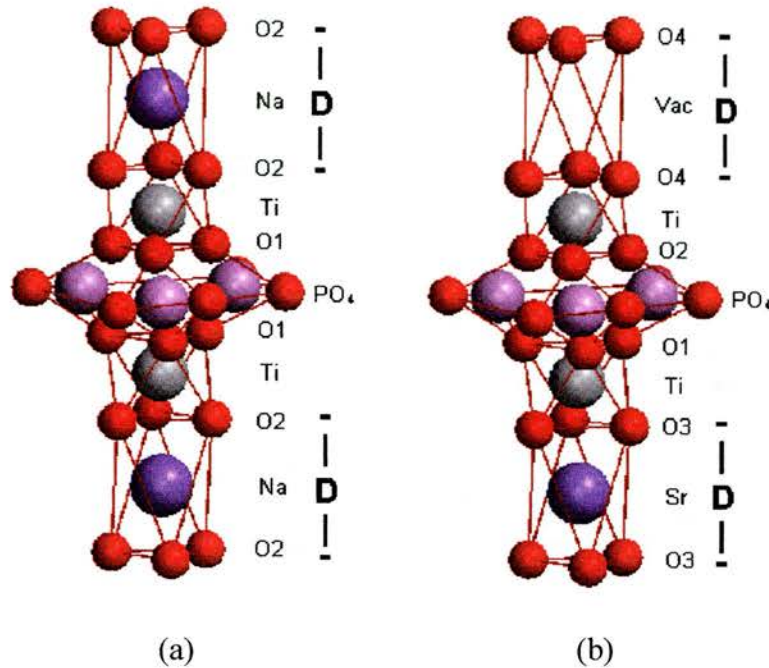


Figure 3.1. (a) Portion of the ideal (R-3c) NZP structure showing packing of polyhedral units along the c -axis. (b) In SrTP the MIa site (0,0,0) is fully occupied containing a Sr cation, while the MIb site (0,0,1/2) is vacant, leading to space group R-3. The parameter D refers to the distance between adjacent O2 or O3/O4 planes along the c -axis.

The MI sites can be made partially or completely vacant as in the case of $\text{Sr}_{0.5}\text{Zr}_2(\text{PO}_4)_3$ (50% vacancy), $\text{La}_{0.33}\text{Zr}_2(\text{PO}_4)_3$ (67% vacancy) or $\text{NbZr}(\text{PO}_4)_3$ (100% vacancy). In the case of Sr and other such materials, the substitution of the divalent cation not only results in the formation of the aforementioned vacancies but that these vacancies order alternately with the cations along the c -axis, leading to crystallographically distinct MIa and MIb sites and a symmetry change to the lower symmetry R-3 space group.

3.1.2: Thermal Expansion Anisotropy

Measurements of lattice parameter evolution versus temperature by X-ray powder diffraction have shown that, in general, the thermal expansivity behaviour of the

R-3c and R-3 families is different, with the former showing a positive coefficient of the c-axis expansivity (α_c) and a negative coefficient of the a-axis expansivity (α_a), while the situation for the R-3 family is reversed^{2,3}. The material $\text{Ca}_{0.5}\text{Zr}_2(\text{PO}_4)_3$ (CaZP) is an exception, it crystallising in space group R-3 yet exhibiting R-3c style thermal expansion properties. Limaye et al⁴ synthesised the material $\text{Ca}_{0.25}\text{Sr}_{0.25}\text{Zr}_2(\text{PO}_4)_3$ (CaSrZP), which combined the behaviour of CaZP with the more conventional R-3 behaviour of SrZP to create an essentially zero expansion material. Other materials such as $(\text{Sr}_{1-x}\text{K}_{2x})\text{Zr}_4(\text{PO}_4)_6$ ⁵, result by forming solid solutions between end member phases having R-3 and R-3c space groups.

Although a very elegant general model has been proposed to describe the thermal behaviour of these materials, in terms of co-operative rotations of linked polyhedra, the specific issue of the contrasting behaviour of the R-3c and R-3 series has not been satisfactorily addressed. The first experiment compares NaTP and SrTP to look at this.

Recent studies by Kutty et al⁶ varied the framework composition of the system and mentioned disorder from the MI site onto the extra framework MII sites as a possible explanation of the c axis contraction. This was not backed up by a structural study and is also investigated in this work. The position of the MII sites is shown in figure 3.2 below.

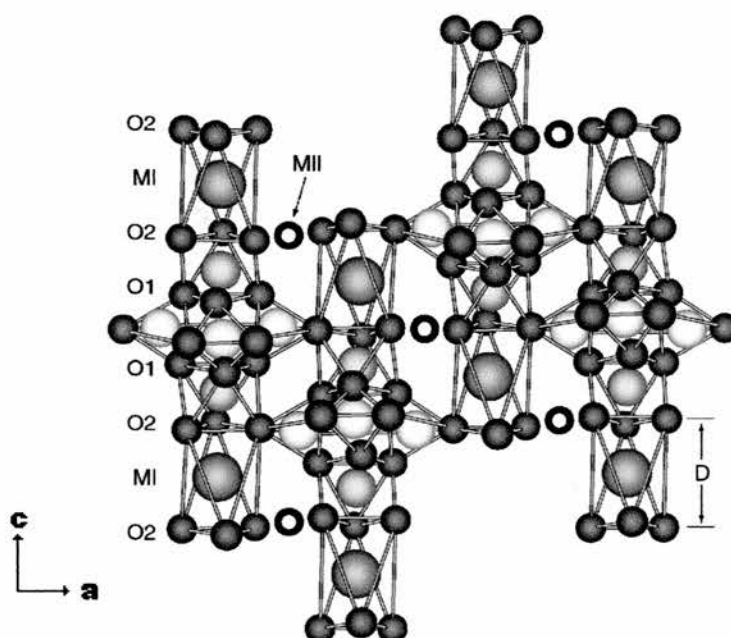


Figure 3.2: The NZP structure showing the position of MII sites.

3.1.3: Effect of Cation Size

Oota et al⁷ have studied a series of NZP materials such as LiZP, KZP and NZP, all of which showed a negative α_a and positive α_c , and showed a decrease in anisotropy when substituting larger ions for Na. Huang et al³ were the first to carry out a systematic study of MTP materials (Ti substituted for Zr in NZP), substituting Li, Na, K, Cs and Mg, Ca, Sr, Ba into the system. Huang's results also showed a correlation between ionic size and the thermal expansion properties. LiTP, NaTP and KTP are compared later.

3.1.4: The Alamo Model

Alamo⁸ first proposed a model of the thermal expansivity of the system based on the expansion and contraction of the MI site leading to coupled rotations of the polyhedral network. He had previously suggested the same model to explain the contraction of the a axis when substituting a larger cation into the room temperature structure. Lenain and Alamo et al⁹ had developed the model to include Li, Na, K, Rb and $\text{Cs}_{0.5}\text{Zr}_2(\text{PO}_4)_3$ and Rodrigo et al¹⁰ had studied a sample of NaTP using high temperature X-ray powder diffraction to confirm the model. It was also extended to include $\text{Ca}_{0.5}\text{Zr}_2(\text{PO}_4)_3$, $\text{LiGe}_2(\text{PO}_4)_3$ ¹¹ and $\text{NaSn}_2(\text{PO}_4)_3$ ¹² in high temperature powder neutron diffraction studies, although these studies were limited with the X-ray powder diffraction study of $\text{NaTi}_2(\text{PO}_4)_3$ (NaTP) at only five temperatures between 25°C and 800°C, the neutron powder diffraction study of $\text{Ca}_{0.5}\text{Zr}_2(\text{PO}_4)_3$ (CaZP) at only two temperatures, and the neutron powder diffraction study of $\text{NaSn}_2(\text{PO}_4)_3$ at four temperatures. Extensive use of this model has been used throughout this chapter and it is applied to many more materials over a greater temperature range.

The model is based on changing the size of the trigonal anti-prism around the Na position, and was originally proposed to explain the variation of lattice parameters between different members of the NZP series. When a substitution of Na by a larger ion is made (e.g. K, forming KZP) the unit cell contracts in the a -direction and expands in the c -direction. Similarly, when the Na-O bond length increases with T , coupled rotations of the TiO_6 and PO_4 polyhedra lead to an expansion in c

and a contraction in a .

As mentioned earlier, it is the expansion and contraction of the occupied and vacant MI sites which drives the co-operative rotations of linked tetrahedra and octahedra. The Alamo model breaks down the overall expansivity along both the c and the a axes into individual contributions from the TiO_6 and PO_4 polyhedra. Very little change in the bond lengths within these polyhedra is observed with temperature, and the expansivity is therefore described in terms of rotations and distortions of the polyhedra. The TiO_6 octahedron lies on a 3-fold axis along c , and its projection is shown in figure 3.3.

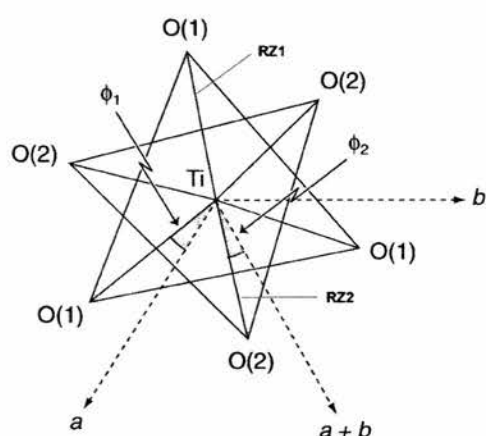


Figure 3.3: Projection of a TiO_6 octahedron along the 3-fold axis (c -axis).

RZ1 and RZ2 define Ti-O distances projected onto the ab plane, while ϕ_1 and ϕ_2 define rotations of the "upper" and "lower" O_3 planes around the c -axis. The PO_4 tetrahedron lies on a 2-fold axis in space group R-3c. Corresponding projected distances and rotation angles in this polyhedron are shown in figure 3.4 - RP1, RP2, θ_1 and θ_2 .

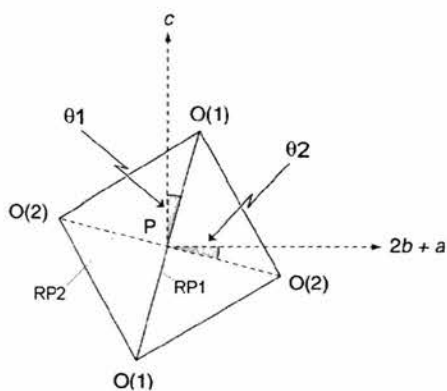


Figure 3.4 - Projection of a PO_4 tetrahedron along the 2-fold axis (a -axis).

The angles Ω and Δ are a measure of the distortion of the octahedra and tetrahedra, calculated as follows:

$$\Omega = \phi_1 - \phi_2 + 60^\circ$$

$$\Delta = \theta_2 - \theta_1 + 90^\circ$$

A related way of viewing this behaviour is to look at the thermal evolution of key Ti-O-P inter-polyhedral bond angles - such an approach has been used by Evans et al. in interpreting the behaviour of $\text{Sc}_2(\text{WO}_4)$ and related materials¹³. This interpretation of the data is also discussed.

3.1.5: Sample Preparation

There are three main methods for the preparation of NZP type materials: sol gel; solid state and hydrothermal methods.

The sol gel method¹⁴ involves aqueous solutions of alkali earth nitrates, $\text{ZrOCl}_2 \cdot 8\text{H}_2\text{O}$ and $\text{NH}_4\text{H}_2\text{PO}_4$ or H_3PO_4 as precursors. Stoichiometric amounts of nitrate and Zr solutions are mixed first under constant-stirring conditions, and then the P solution is added slowly. The order of mixing is very important to obtain a homogeneous gel and single-phase material. The gel is dried at 90°C for 24h forming a fine grained amorphous precursor, and calcined at 700°C for 16h. The calcined product is consolidated into disks which are heat-treated at 1200°C for 24h to produce highly dense ceramics of single phase NZP material. This method allows good mixing and a high degree of reactivity.

The solid state method¹⁵ involves intimately mixing stoichiometric amounts of the dry precursor oxides, which are calcined at high temperature. This is the

principal method used in these studies.

The hydrothermal method¹⁶ requires preparation of the sol gel powder followed by reaction at low temperature (200-300°C) and elevated pressure.

The preparation method can have an effect on the thermal expansivity, which will be discussed later.

3.2: A Neutron Powder Diffraction Study of $\text{NaTi}_2(\text{PO}_4)_3$ (NaTP) and $\text{Sr}_{0.5}\text{Ti}_2(\text{PO}_4)_3$ (SrTP)

The thermal expansion anisotropies of the R-3c material NaTP and R-3 material SrTP are compared and contrasted.

3.2.1: Experimental

Samples were prepared from stoichiometric quantities of TiO_2 , $(\text{NH}_4)_2\text{HPO}_4$ and Na_2CO_3 or SrCO_3 . Thoroughly ground mixtures were preheated at 200°C, followed by subsequent heat treatments at 600°C, 900°C and 1000°C with intermediate regrinding. For the Sr sample a final treatment at 1200°C was required. Neutron diffraction data were collected on the high flux diffractometer D1B at the ILL, Grenoble, using a wavelength of 2.522Å and a fixed detector bank covering 80° in 2θ. In order to determine the thermal evolution of the lattice parameters, a series of 123 short (~10 minute) scans was collected over the range 25°C < T < 835°C. These scans were refined with the cyclic version of the refinement program FULLPROF¹⁷ using the result for a run at a given temperature as input file for the following run with slightly higher temperature. Runs at selected temperatures were then chosen for detailed structural analysis. Rietveld refinement was carried out using the GSAS package¹⁸. The starting model for the refinement of the $\text{Sr}_{0.5}\text{Ti}_2(\text{PO}_4)_3$ structure was taken from Senbhagaraman et al.¹⁹. A typical refinement consisted of 17 structural parameters, with 400 data points and 80 contributing reflections over the range 18 < 2θ < 98°.

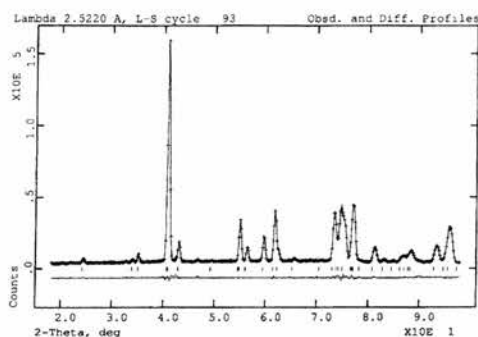


Figure 3.5: Rietveld plot for NaTP

3.2.2: Results and Discussion

Plots of the thermal evolution of the lattice parameters for both compounds are shown in figure 3.6.

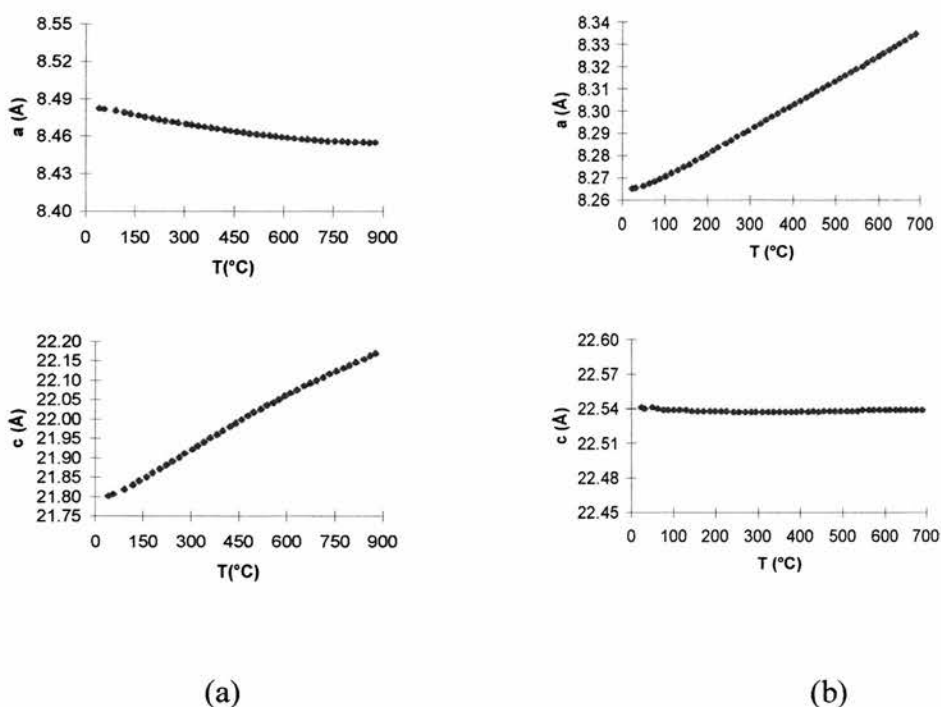


Figure 3.6. Thermal evolution of lattice parameters for (a) $\text{NaTi}_2(\text{PO}_4)_3$ and (b) $\text{Sr}_{0.5}\text{Ti}_2(\text{PO}_4)_3$.

Values of α are $-5.3(2)$ and $20.8(3) \times 10^{-6} \text{°C}$ for $\text{NaTi}_2(\text{PO}_4)_3$ in the range $25 - 500 \text{°C}$ and $13.2(2)$ and $-0.02(2) \times 10^{-6} \text{°C}$ for $\text{Sr}_{0.5}\text{Ti}_2(\text{PO}_4)_3$ in the range $25 - 800 \text{°C}$, which are in good agreement with those reported by earlier studies³. Although thermal evolution of lattice parameters by X-ray powder diffraction has

been carried out for both these samples, the present study provides, for the first time, precise structural details by neutron diffraction, which allows the mechanism of their behaviour to be pinpointed. One of the most significant trends is the near-zero expansivity of the c-axis for the Sr compound. It has previously been suggested that the largest contribution to the expansivity in NZP materials is the expansion of the Na-O bond itself. This governs the "size" of the trigonal prismatic site along the c-axis (ie. the O-O contact), which is plotted in figure 3.7.

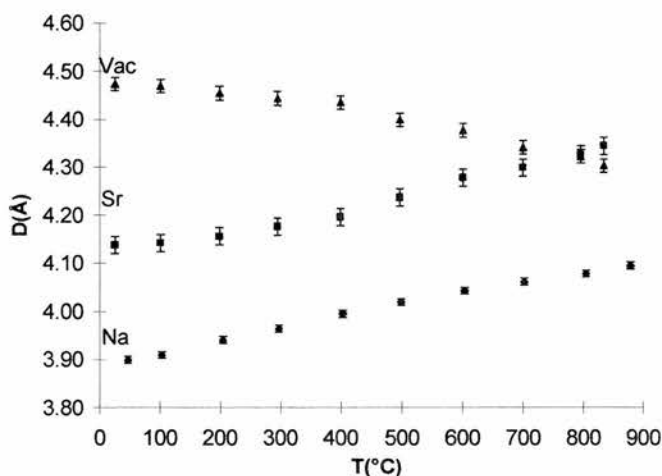


Figure 3.7. Thermal evolution of the trigonal prismatic MI sites (ie. O-O distance, D , along the c-axis). In $\text{NaTi}_2(\text{PO}_4)_3$ the c-axis expansivity is governed by $2 \times D(\text{Na})$, in $\text{Sr}_{0.5}\text{Ti}_2(\text{PO}_4)_3$ by $D(\text{Sr}) + D(\text{vac})$. Circles represent the expansion of the Na site, squares the Sr site and triangles the vacancy in SrTP.

In the case of the Sr compound in R-3 there are two such sites to consider - the Sr site and the vacancy site, which are confirmed to be completely ordered from the refinements. It can be seen that, in the Na compound this site expands, by $\sim 0.20 \text{ \AA}$ over the full temperature range, accounting completely for the overall expansivity α (two per unit cell), whereas in the Sr compound there is an expansion of the Sr site but a contraction of the vacancy site. These two almost exactly cancel out, resulting in the observed near-zero expansion coefficient, α . These parameters in turn result in the co-operative polyhedral rotations described by earlier workers, and lead to the expansivities along the a-axis. A full analysis of these effects is discussed later, but the fundamental explanation of the c-axis expansivity lies simply in the relative expansion/contraction of the occupied and vacant MI sites. The anomaly previously observed in the case of $\text{Ca}_{0.5}\text{Zr}_2(\text{PO}_4)_3$, which shows the

behaviour of an R-3c structure rather than an R-3 structure lies in the fact that in that case both the Ca site and the vacancy site expand with temperature, resulting in a net expansion of the c-axis. Apparently the smaller vacancy site in that case ($\sim 4.1 \text{ \AA}$ at 25°C) is not as compressible as the vacancy site in the present phase. A diffraction experiment cannot differentiate whether the unusual behaviour of the Sr phase is due to cation-ordering *per se* or merely the presence of equal numbers of filled and vacant MI sites. However, it is interesting to note that a larger value of $\alpha_c = 1.37 \times 10^{-6} \text{ }^\circ\text{C}^{-1}$ has been reported for $\text{Ba}_{0.5}\text{Ti}_2(\text{PO}_4)_3$, which crystallises in the disordered R-3c structure type. A comparative, detailed neutron diffraction study of the Sr and Ba materials can be found in section 3.5. However, in this experiment it is shown that this behaviour is directly related to the cation-vacancy ordering, and is due to the compressibility of the vacant site along the c-axis.

3.3 Neutron Diffraction Study of $\text{La}_{0.33}\text{Ti}_2(\text{PO}_4)_3$ (LaTP)

In this experiment the behaviour of NaTP, SrTP and LaTP are compared to look at the effect of a partial occupancy of the MI site, as LaTP has a 67% vacancy here.

3.3.1: Experimental

LaTP was prepared from stoichiometric quantities of TiO_2 , $(\text{NH}_4)_2 \text{HPO}_4$ and a 10% stoichiometric excess of dried La_2O_3 (probably required as 500°C was too low a temperature to fully dry the La_2O_3), which were thoroughly ground together, pelleted and fired at 200°C for 6 h, 600°C for 24 h followed by successive 24h firings at 100°C intervals from 900 to 1300°C . Neutron diffraction data for LaTP were collected on the SEPD instrument at the IPNS, Argonne²⁰. The sample was loaded in a thin-walled vanadium can in a 'coffee-can' furnace and data were collected at 25, 100, 200, 250 and 300°C each run lasting approximately 2 h. Rietveld refinement was carried out with the GSAS package¹⁸. Preliminary analysis of the room temperature X-ray powder diffraction data suggested that LaTP adopts the R-3 space group as found for the cation-deficient phases SrTP and CaTP. Lattice parameters for LaTP had been originally reported by Senbhagaraman et al.²¹ but no space group had been

suggested. The initial model was taken from that of SrTP which involves a complete ordering of MI cations (i.e. La in this case) over the two available sites, i.e. two-thirds occupancy of one MI site. This model was found to be verified for all the temperatures studied. A typical Rietveld refinement included 52 variables, 2100 reflections and 5200 data points over the d-spacing range 0.534 to 4.000Å.

3.3.2: Results and discussion

Atomic parameters determined for LaTP at 25° and 300°C are given in Table A1.3 in Appendix 1. A typical Rietveld plot is shown in figure 3.8 below.

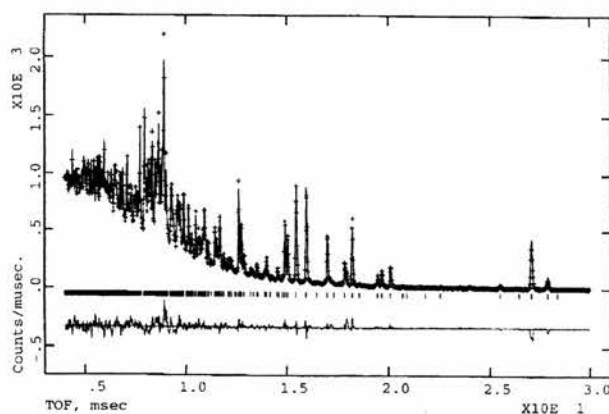


Figure 3.8 – A typical Rietveld plot for LaTP at 25°C on the SEPD instrument

Plots of the thermal evolution of lattice parameters are given in figure 3.9. Linear coefficients of thermal expansion are calculated according to the equation shown in section 1.3.

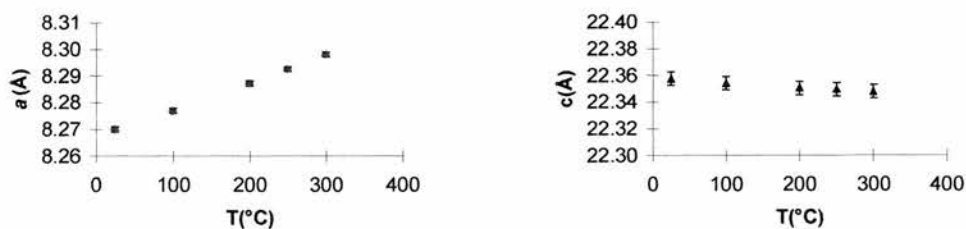


Figure 3.9 - Thermal evolution of lattice parameters for LaTP

The values found from these data for LaTP are compared to some other Nasicon-related materials in Table 3.1 below.

Table 3.1: Selected thermal expansion coefficients for NZP materials

Compound	α_a^a	α_c^a	Space group	Reference:
NaTP	-5.3	20.8	R-3c	Section 3.2
SrTP	13.5	-0.02	R-3	Section 3.2
LaTP	12.44	-1.53	R-3	This work
LaTP	-0.106	0.672	not specified	21
NaZP	-5.5	23.8	R-3c	7
SrZP	3.6	-1.2	R-3	4
NbZP ^b	-3.2	8.1	R-3c	7

^a ($\times 10^{-6} \text{ } ^\circ\text{C}^{-1}$)

^b ($\text{NbZr}(\text{PO}_4)_3$)

It can be seen that materials crystallising in the cation-ordered space group R-3 show opposite behaviour in their thermal anisotropy to those crystallising in the ordered R-3c space group, i.e. α_a is positive and α_c is negative in the former case (although, note that the previous work on LaTP suggests the opposite anisotropy in that case). It has previously been shown (section 3.2), in the case of SrTP versus NaTP that the root cause of this unusual behaviour lies in the thermal expansivities of the occupied and vacant MI sites, which in turn drive co-operative rotation of linked tetrahedra and octahedra. Now addressed is the comparative behaviour of the LaTP and SrTP materials, the differences in which might be expected to relate to the varying cation site occupancy, size and charge. The Alamo model is applied. However, a key addition to it is that within an R-3 system, two sets of ϕ values are required since, in space group R-3, there are two crystallographically distinct TiO_6 , octahedra (figure 3.1). It can be seen that these octahedral sites surround the occupied and vacant MI sites, respectively.

The expansivities of the MI site are defined in terms of the parameter D , originally defined in section 3.1, which is the distance along the c-axis between the 'top' and 'bottom' oxygen planes of the trigonal antiprismatic site. It is this

parameter which directly defines the expansivity along the c-axis. The values for SrTP and LaTP are plotted in figure 3.10.

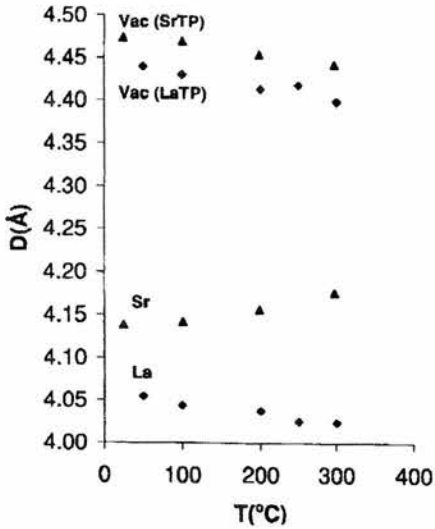


Figure 3.10: Thermal evolution of the trigonal anti-prismatic MI sites (i.e. O-O distance D , along the c-axis) in SrTP and LaTP. The c-axis expansivity is governed by $[D(M)+D(\text{vac})]$.

In SrTP more or less equal and opposite expansivities of the filled and vacant MI sites lead to a net zero α_c . In LaTP on the other hand, both occupied and vacant sites are found to contract on heating (since the occupied site is only two-thirds full) leading to a net negative α_c . Explanation of the a-axis expansivities is more complex. It is instructive to simplify this with reference to the Ti-Ti pathway shown in figure 3.11 which refers to Ti atoms at $(0, 0, 0.1469)$ and $(2/3, 1/3, 1/3-0.1469)$.

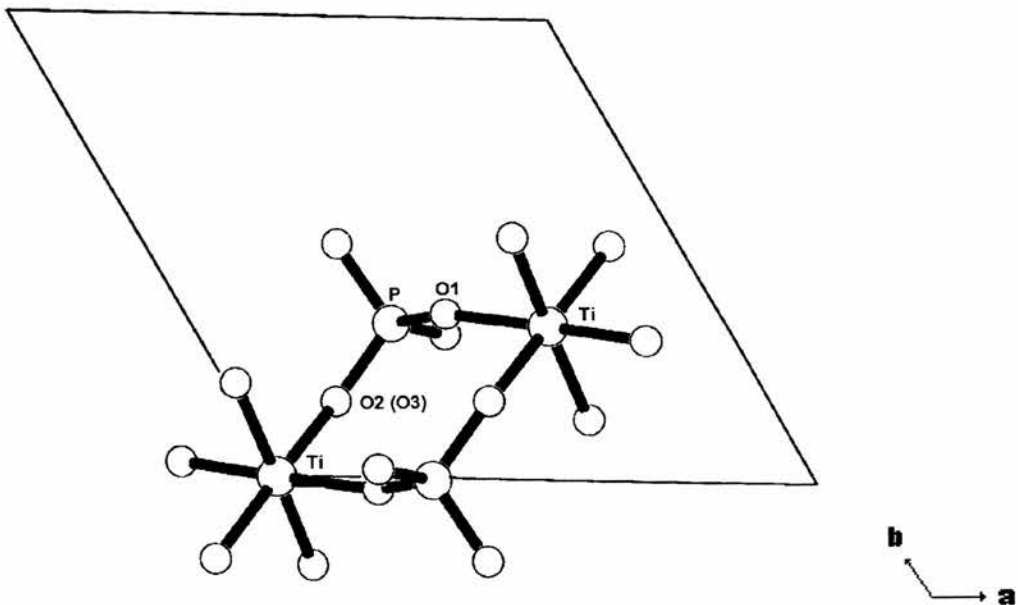


Figure 3.11: The Ti-Ti pathway

The length of the a-axis is then defined exactly by the expression:

$$a = \sqrt{3}[2RP^2 \cos \theta^2 + 2RZ^2 \cos(\pi/6 + \phi_2)]$$

as given by Alamo⁸.

From this relationship, which is fixed by symmetry, the effective separate contributions to the a-axis expansivity from both tetrahedra and octahedra can be quantified. Values of the parameters (Alamo) for LaTP are presented in Table 3.2. For comparison the corresponding parameters for NaTP and SrTP are plotted in figures 3.12-3.16.

Table 3.2: Alamo parameters for LaTP

	25°C	100°C	200°C	250°C	300°C
ϕ_{1-1}	3.78	4.05	4.27	4.47	4.74
ϕ_{2-1}	-5.26	-5.05	-4.65	-4.40	-4.10
Ω_1	69.04	69.10	68.92	68.87	68.85
ϕ_{1-2}	40.06	40.33	40.79	41.05	41.30
ϕ_{2-2}	39.79	40.04	40.45	40.57	40.64
Ω_2	60.27	60.29	60.34	60.48	60.66
θ_1	4.46	4.78	5.05	5.24	5.60
θ_2	11.14	10.88	10.54	10.51	10.07
Δ	96.68	96.10	95.49	95.28	94.47

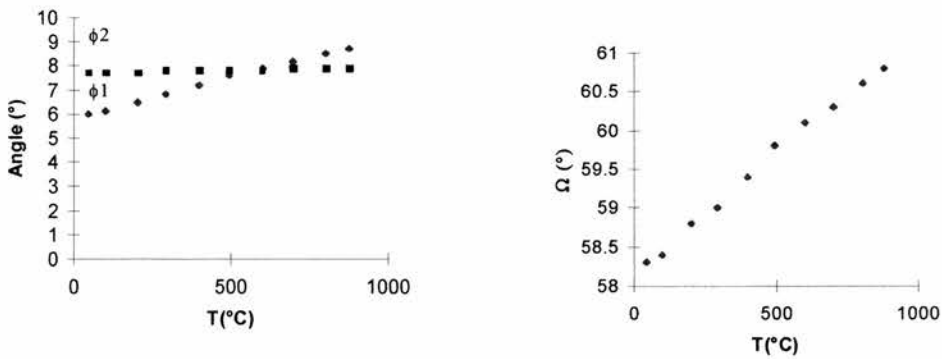


Figure 3.12: Variation of the parameters (a) ϕ_1 and ϕ_2 and (b) Ω for NaTP

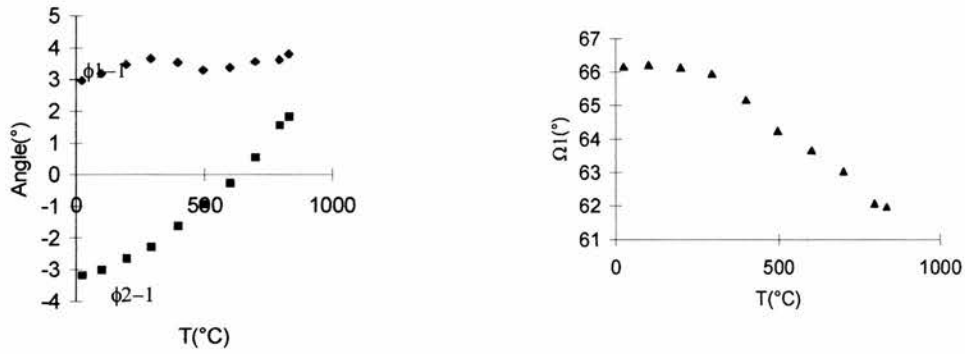


Figure 3.13: Variation of the parameters (a) ϕ_{1-1} and ϕ_{2-1} and (b) Ω_1 for SrTP

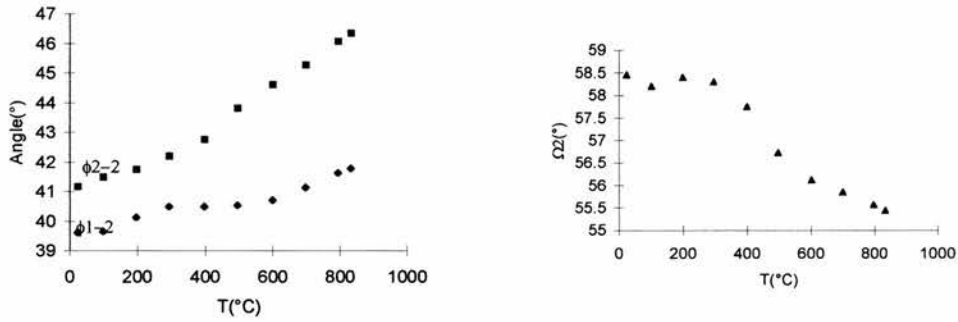


Figure 3.14: Variation of the parameters (a) ϕ_{1-2} and ϕ_{2-2} and (b) Ω_2 for SrTP

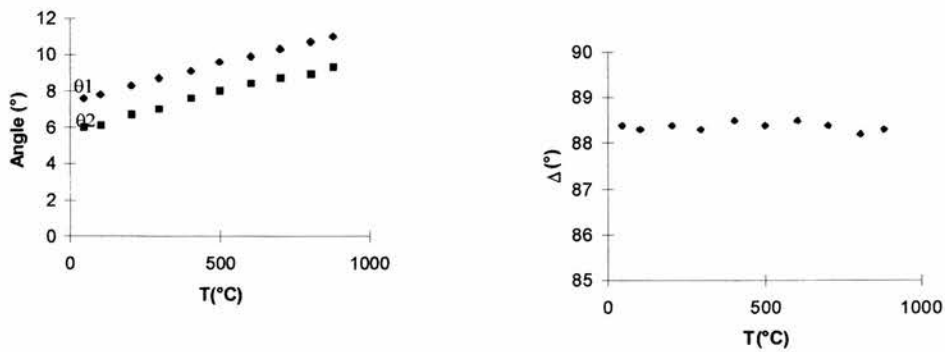


Figure 3.15: Variation of the parameters (a) θ_1 and θ_2 and (b) Δ for NaTP

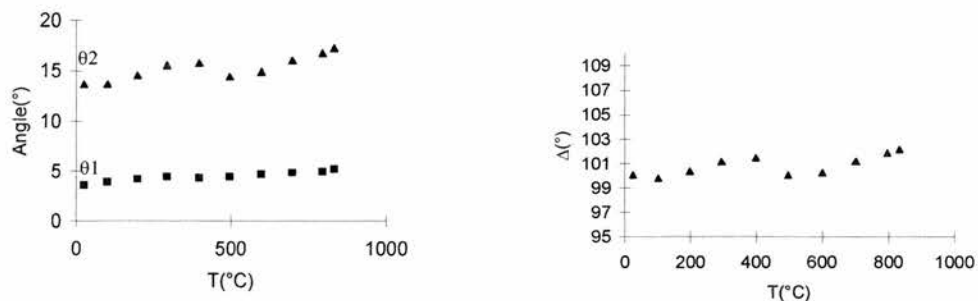


Figure 3.16: Variation of the parameters (a) θ_1 and θ_2 and (b) Δ for SrTP

The most significant trends in these variables are: within NaTP ϕ_1 increases while ϕ_2 remains virtually constant, resulting in an increasing Ω as the octahedron becomes more regular. In SrTP ϕ_1 -1 and ϕ_2 -1 both increase and Ω_1 becomes closer to 60° , i.e. the Ti(1) octahedron becomes more regular with increasing T, but this is only significant above about 300°C . In LaTP both ϕ_1 -1 and ϕ_2 -1 increase slightly, but Ω_1 stays virtually constant; essentially the same as in SrTP. For the Ti(2) octahedron, in SrTP both ϕ_1 -2 and ϕ_2 -2 increase and Ω_2 decreases, the octahedron being less regular. In LaTP, similarly, both ϕ_1 -2 and ϕ_2 -2 increase and the octahedron again becomes slightly less regular. The changes in the angles related to the tetrahedron show greater contrast. For both NaTP and SrTP, θ_1 and θ_2 increase, but result in only small changes in Δ . However, in LaTP θ_1 increases and θ_2 decreases resulting in a 2° change in Δ over this small temperature range.

The overall effect of these changes in LaTP is a resultant expansion of the a-parameter from $8.26988(9)$ to $8.29811(16)\text{\AA}$ over the temperature range 25 - 300°C . This can be broken down into an expansion of 0.0772\AA due to the tetrahedral contribution and a contraction of 0.0561\AA due to the octahedral contribution. This compares with $+0.45\text{\AA}$, -0.36\AA for SrTP and -0.126\AA , $+0.098\text{\AA}$ for NaTP, both over the expanded temperature range 25 - 800°C . A possible simplified explanation of the negative values of α_a for the R-3c structure versus the positive values of α_a for the R-3 structure, which may be seen in the values of Ω , is in the degree of freedom allowed to the Ti(2) octahedron, by virtue of the neighbouring M1 site being unoccupied. This allows the Ti(2)

octahedron to become more distorted versus T , apparently driving the observed expansion. An explanation of the opposing behaviour in terms of opposing rotations of the TiO_6 octahedra, as suggested by Alamo and Rodrigo²² is not clear-cut as, in the present case, all the octahedral rotations in the three materials occur in the same sense.

It has been suggested in earlier work on related framework systems, such as ZrW_2O_8 ²³ and $\text{Sc}_2(\text{W}_2\text{O}_4)_3$ ¹³, that the polyhedra in these systems may be regarded to a good approximation, as rigid bodies. The key parameter in determining expansivity may therefore be regarded as the bending mode of the M-O-M type linkages. In the light of this an alternative view of the a-axis expansivity in SrTP and NaTP is proposed, which is to look at changes in the key Ti-O-P bridging bond angles linking the polyhedra. These are plotted for NaTP, SrTP and LaTP in figure 3.17.

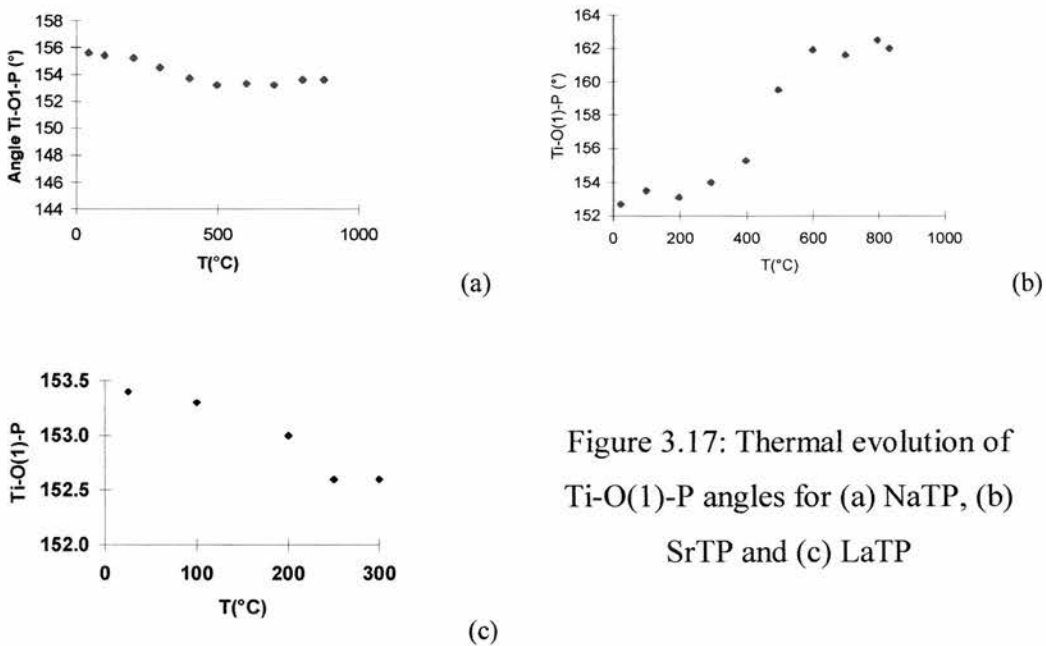


Figure 3.17: Thermal evolution of Ti-O(1)-P angles for (a) NaTP, (b) SrTP and (c) LaTP

It can be seen that a possible alternative to the Alamo model explanation of the positive α_a for SrTP and negative α_a for NaTP lay in respective expansion/contraction of this bond angle. In LaTP, however, the angle shows a very slight decrease over the limited temperature range studied here, which apparently conflicts with the model proposed for SrTP. Furthermore, the value of Δ derived from the LaTP refinements above suggest that it may not be valid to

use a rigid polyhedron model to explain the expansivity behaviour. Clearly further studies of this and related systems over an expanded temperature range is merited.

3.3.3: Conclusions

The present work on LaTP supports the earlier conclusion that the root cause of the unusual thermal expansivity behaviour in these systems is the relative expansion and contraction of filled and vacant extra-framework MI sites. In the present case both sites contract slightly due to the partial occupancy of the La site, whereas in the case of SrTP a more or less equal and opposite expansion of the filled and vacant sites was observed. This provides the simplest explanation of the *c*-axis expansivity in all these systems. The Alamo model of breaking down the *a*-axis expansivity into octahedral and tetrahedral components can be used to relate the *a*-axis expansivity to thermally induced rotations and distortions of the polyhedra. Over the limited temperature range available here, however, the relationship of the *c*-axis expansivity to the bridging Ti-O-P bond angles, which is clear in the SrTP and NaTP systems, is not necessarily valid. This may be due to studying only a limited temperature range. Another factor which needs to be considered is the refinement strategy; in the three systems studied an isotropic refinement of all atoms treated independently has been assumed. Clearly a free anisotropic refinement, or a rigid-body refinement, as discussed by Evans et al.¹³, must also be considered in future work.

3.4: A Neutron Powder Diffraction Study of NbTi(PO₄)₃ (NbTP)

As mentioned above, in NbTi(PO₄)₃ the MI sites are completely vacant. Presented here, for the first time are detailed structural refinements of NbTP from powder neutron diffraction studies and the behaviour of this material related to the model for thermal expansivity within NZP phases proposed by Alamo.

3.4.1: Experimental

The sample $\text{NbTi}(\text{PO}_4)_3$ was prepared using starting materials Nb_2O_5 (99.99%, Aldrich), TiO_2 (99.9+%, anatase, Aldrich) and $(\text{NH}_4)_2\text{HPO}_4$ (99%, Aldrich) ground in stoichiometric amounts under acetone, pelleted and heated in alumina crucibles. The heat treatment used consisted of 18h at 200°C , 6h at 600°C , 12h at 900°C and a final heating of 24h at 1300°C . Intermediate regrinding was carried out between each heating stage. The sample was characterised on a STOE STADI-P diffractometer using $\text{Cu K}\alpha_1$ radiation which revealed the sample to be phase pure.

The neutron diffraction experiment was carried out on the POLARIS instrument at the Rutherford Appleton Laboratory²⁴. Data were collected for 10g of sample for $250\mu\text{Ah}$ at the temperatures $T = 25^\circ\text{C}$ and $200\text{--}800^\circ\text{C}$ at 100° intervals. The GSAS program¹⁸ was used for data analysis.

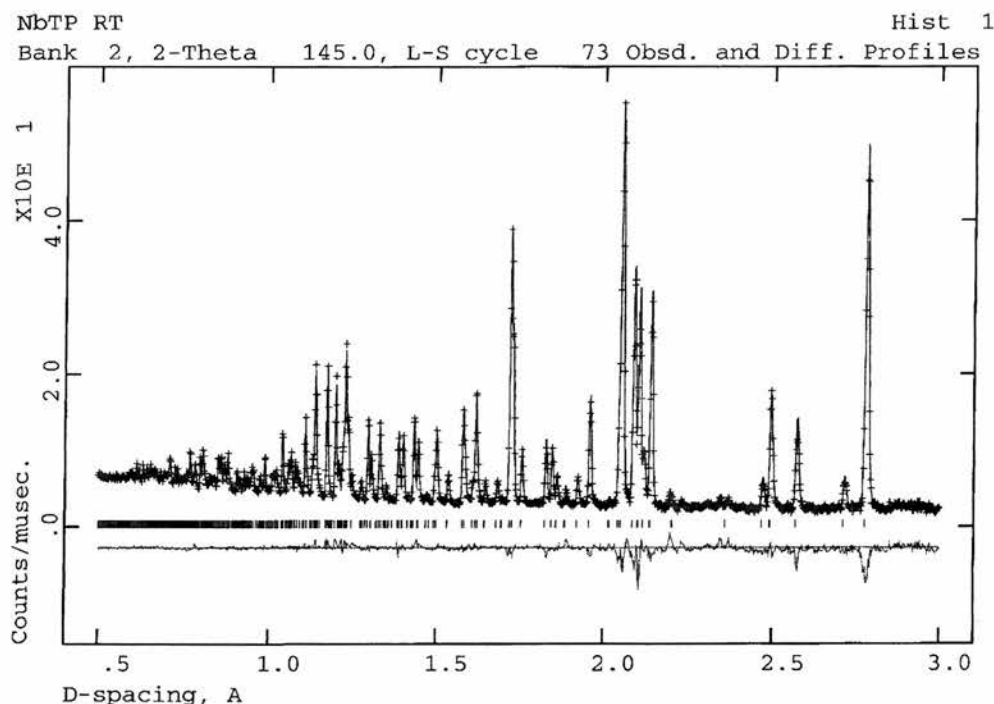


Figure 3.18: Rietveld plot for NbTP at 25°C

3.4.2 Results and Discussion

Atomic positions for NbTP as determined by Berry et al²⁵ in space group R-3c were used as starting values. The experimentally determined positions for

T=25°C and T=800°C are shown in Table A1.4 in Appendix 1.

Plots of the lattice parameters a and c and cell volume vs. temperature are shown in figure 3.19. It can be clearly seen that there is a non-linear contraction of the a axis and expansion of the c axis, leading to a slight overall volume contraction.

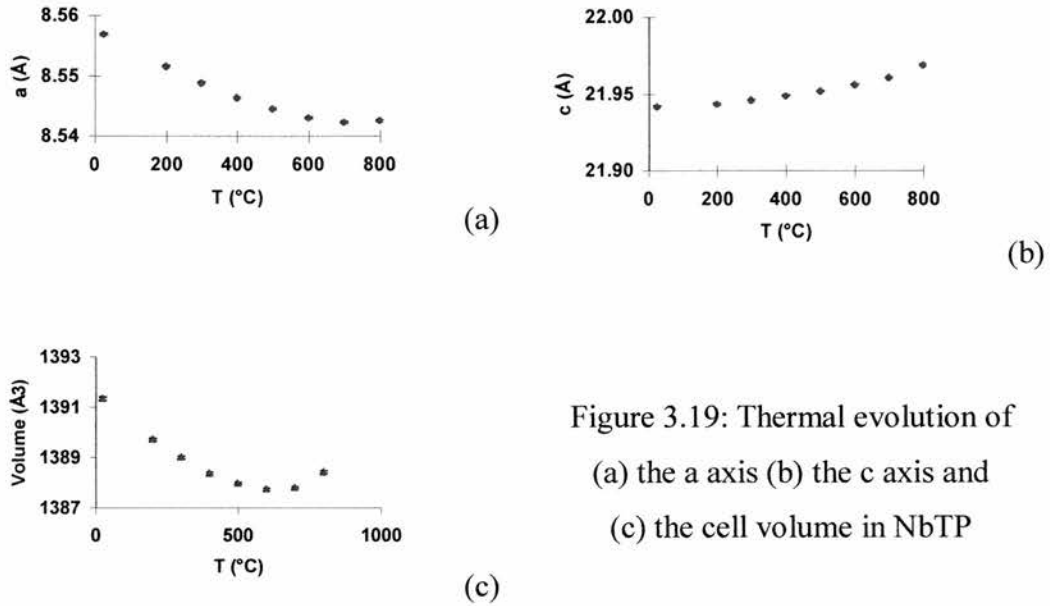


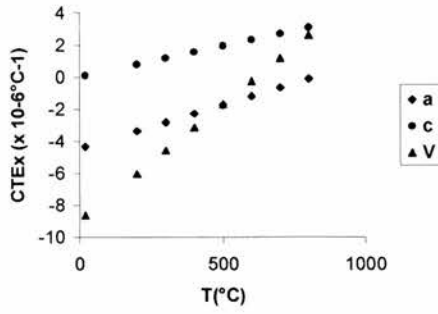
Figure 3.19: Thermal evolution of
 (a) the a axis (b) the c axis and
 (c) the cell volume in NbTP

The refined lattice parameters (p) were fitted against temperature by the polynomial expression $p = p_0 + p_1T + p_2T^2$ (1)

Table 3.3 below shows the values obtained for a, c and V.

	p_0	p_1	p_2
a	8.5579	-3.81E-5	2.32E-8
c	21.942	1.38E-7	4.21E-8
V	1391.7	-0.0124	1.00E-5

Table 3.3 - Coefficients of the equation $p = p_0 + p_1T + p_2T^2$ used to fit the lattice parameters a and c and the volume V against temperature (T in °C)



Plots of α_a , α_c and α_v are shown in figure 3.20 (left). These values are in excellent agreement with those reported by Kutty et al ⁶.

The Alamo model as described in section 3.1.4 was applied and plots of the changes of these angles are shown in figure 3.21.

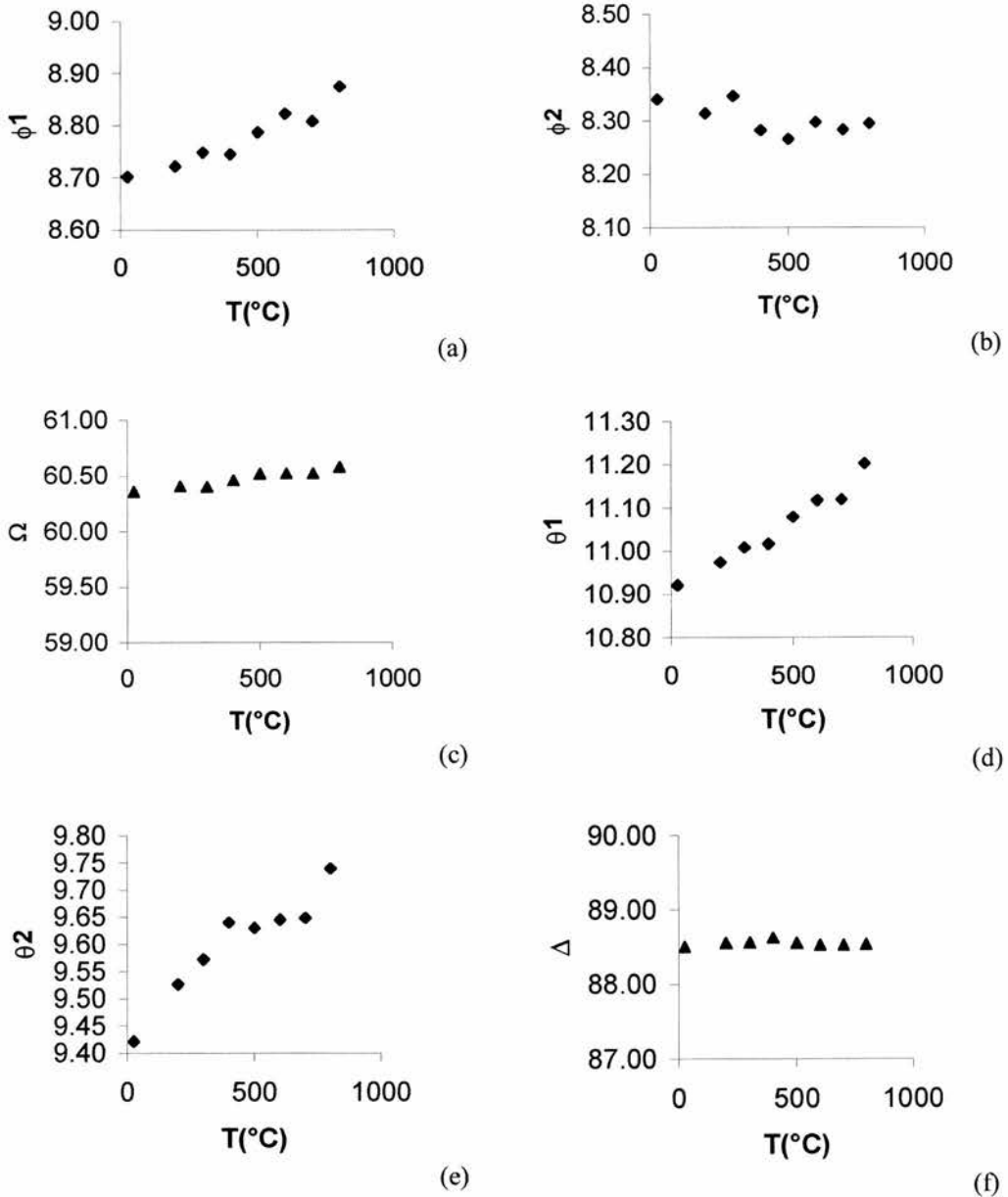


Figure 3.21: Thermal evolution of the Alamo angles
 (a) ϕ_1 (b) ϕ_2 (c) Ω (d) θ_1 (e) θ_2 (f) Δ for NbTP

ϕ_1 increases from 8.7° to 8.9° and ϕ_2 shows a slight decrease from 8.35° to 8.30° , leading to a small but significant increase in Ω from 60.35° to 60.60° . θ_1 increases from 10.9° to 11.2° and θ_2 from 9.4° to 9.7° , Δ remaining constant within error limits. These results suggest that the octahedra are distorting slightly and the tetrahedra remaining virtually rigid, as is the case for NaTP. However, the magnitude of the changes in the angles is much smaller here. This is as expected - the expansivity of NbTP is also much smaller due to the smaller expansivity of the vacant MI site, defined as the O1-O1 distance along the c axis. Within NaTP each site expands from 3.899\AA to 4.095\AA : here it is from 4.064\AA to 4.080\AA , an order of magnitude smaller. This accounts almost entirely for the c axis expansion from 21.942\AA to 21.969\AA , a total of 0.0272\AA or 0.0136\AA for each site.

3.4.3 Conclusions

The experimentally determined atom positions for NbTP compare favourably to those of Berry²⁵, but offer a significantly greater degree of precision. The values for the variation of lattice parameters vs. T agree well with those of Kutty⁶. NbTP is a negative thermal expansion material over the range $25^\circ\text{C} < T < 600^\circ\text{C}$ due to the contraction of the a and b axes being greater than the expansion of the c axis. Usually within NZP materials the magnitude of the c axis expansivity is much greater than any contraction of the a axis. However, in this case the MI sites arranged up the c axis, usually occupied by metal cations and the principal cause of overall expansion, are empty.

Analysis of the polyhedral rotations and distortions using the Alamo model reveals that the tetrahedra remain almost rigid, while there is a small distortion of the octahedra; both polyhedra rotate slightly leading to the contraction along a . This is very similar to the behaviour found in $\text{NaTi}_2(\text{PO}_4)_3$ shown in section 3.2, although the scale of the changes is an order of magnitude smaller due to the absence of MI cations.

3.5: A Neutron Powder Diffraction Study of $\text{Ba}_{0.5}\text{Ti}_2(\text{PO}_4)_3$ (BaTP), $\text{K}_{0.5}\text{Nb}_{0.5}\text{Ti}_{1.5}(\text{PO}_4)_3$ (KNTP) and $\text{Ca}_{0.25}\text{Sr}_{0.25}\text{Zr}_2(\text{PO}_4)_3$ (CaSrZP)

In previous sections, following detailed powder neutron diffraction studies on NaTP, SrTP and LaTP it was proposed that the differing behaviour of the R-3c and R-3 systems was due to opposite expansivities of filled and vacant MI sites. It has been suggested by Kutty et al²⁶ that in materials where a contraction of the *c* axis occurs, this may be due to a disordering of the MI cations, which relocate to MII sites on increasing temperature. However, the studies on LaTP showed no such disorder. One question that remained open was whether the *ordering* of filled and vacant MI sites was critical to the anisotropic thermal expansion properties or merely their partial occupancy *per se*. In this section it is aimed to investigate the effect of disordering of cations and vacancies in these sites in order to explore this latter question. It has been suggested that $\text{Ba}_{0.5}\text{Ti}_2(\text{PO}_4)_3$ (BaTP) crystallises in the R-3c structure, having half occupied but disordered MI sites³. $\text{K}_{0.5}\text{Nb}_{0.5}\text{Ti}_{1.5}(\text{PO}_4)_3$ (KNTP) which displays similar behaviour has also been prepared for the first time. Results of powder neutron diffraction studies on both these materials are presented, and compared to the previously studied SrTP and the “zero expansion” material $\text{Ca}_{0.25}\text{Sr}_{0.25}\text{Zr}_2(\text{PO}_4)_3$ (CaSrZP)⁴, both of which have R-3 structures, with ordered cation vacancies.

The results are analysed in terms of the Alamo model⁸ of polyhedral rotations and distortions, and also in terms of the thermal evolution of the key interpolyhedral Ti-O-P angles.

3.5.1: Experimental

Samples were synthesised using stoichiometric quantities of K_2CO_3 (Aldrich, 99+%), TiO_2 (Aldrich, 99.9+%), Nb_2O_5 (Aldrich, 99.99%), CaCO_3 (Aldrich, 99+%), SrCO_3 (Aldrich, 98+%), ZrO_2 (Aldrich, 99%), BaCO_3 (Aldrich, 99+) and $(\text{NH}_4)_2\text{HPO}_4$ (Aldrich, 99%). Starting materials were dried and ground under acetone before being heated to 200°C for 18h, 600°C for 6h and 900°C for 12h. They were then fired for their own individual heat treatment with intermediate regrinding. For $\text{K}_{0.5}\text{Nb}_{0.5}\text{Ti}_{1.5}(\text{PO}_4)_3$, (KNTP) this consisted of 24h at 1000°C followed by 72h at 1100°C, 24h at 1200°C and 2h at 1300°C; for $\text{Ba}_{0.5}\text{Ti}_2(\text{PO}_4)_3$

(BaTP) 24h at 1000°C, 72h at 1100°C, and 48h at 1200°C; and for $\text{Ca}_{0.25}\text{Sr}_{0.25}\text{Zr}_2(\text{PO}_4)_3$ (CaSrZP) 48h at 1200°C followed by 16h at 1340°C. Sample purity was checked on a STOE STADI-P powder diffractometer operating in transmission mode using $\text{CuK}\alpha_1$ radiation.

Time-of-flight powder neutron diffraction data were collected from BaTP and KNTP on the Polaris diffractometer²⁴ while CaSrZP was run on the HRPD diffractometer, both at the ISIS facility, CLRC Rutherford Appleton Laboratory. For each material ca. 5g of sample were loaded into a thin walled vanadium sample can and diffraction patterns collected at room temperature and from 200°C to 800°C in 100°C steps. Diffraction patterns typically consisted of 4400 data points, 38 variables, and 4457 reflections over a d-spacing range of 0.3 to 3.5Å for both samples run on Polaris and 6267 data points, 63 variables, and 1004 reflections over a d-spacing range of 0.8 to 2.5Å for CaSrZP on HRPD.

Structure refinement was carried out by the Rietveld method using the GSAS program¹⁸, with the experimentally observed peak shapes modelled by a convolution of pseudo-Voigt and exponential functions. Anisotropic temperature factors were applied for all atoms. A typical profile fit after Rietveld refinement is shown in figure 3.22.

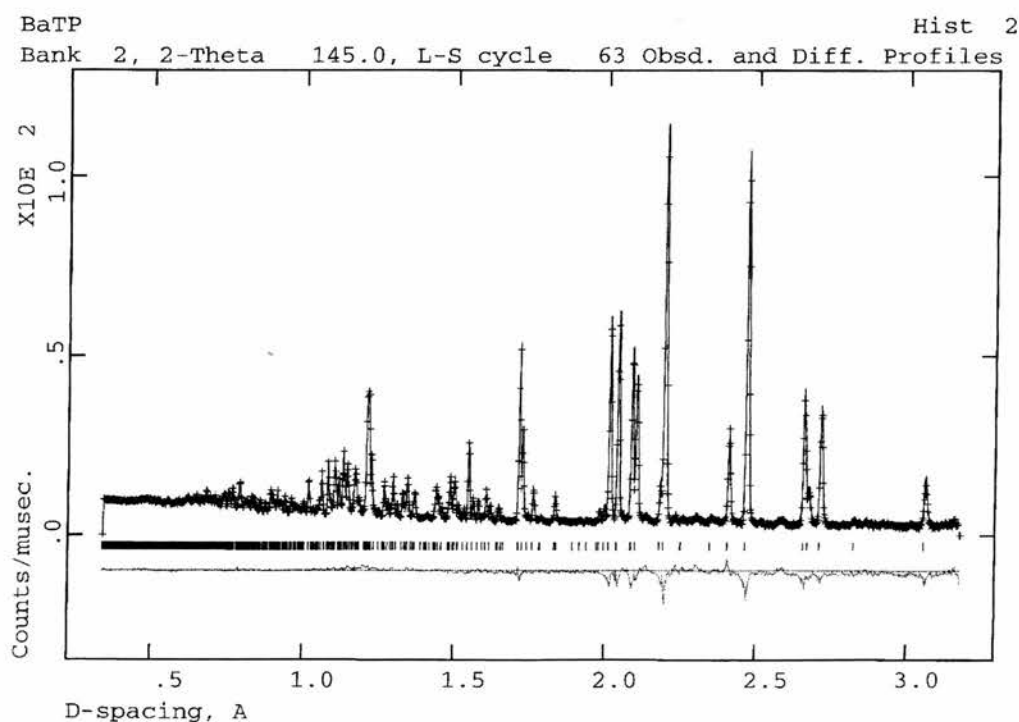


Figure 3.22 – A typical Rietveld plot for $\text{Ba}_{0.5}\text{Ti}_2(\text{PO}_4)_3$ at 20°C

3.5.2: Results and Discussion

i) Coefficients of thermal expansion

The unit cell parameters and atomic co-ordinates at the highest and lowest temperatures are shown in Tables A1.5-A1.7 in Appendix 1. Plots of the behaviour of unit cell parameters and volume are shown in figures 3.23-3.25.

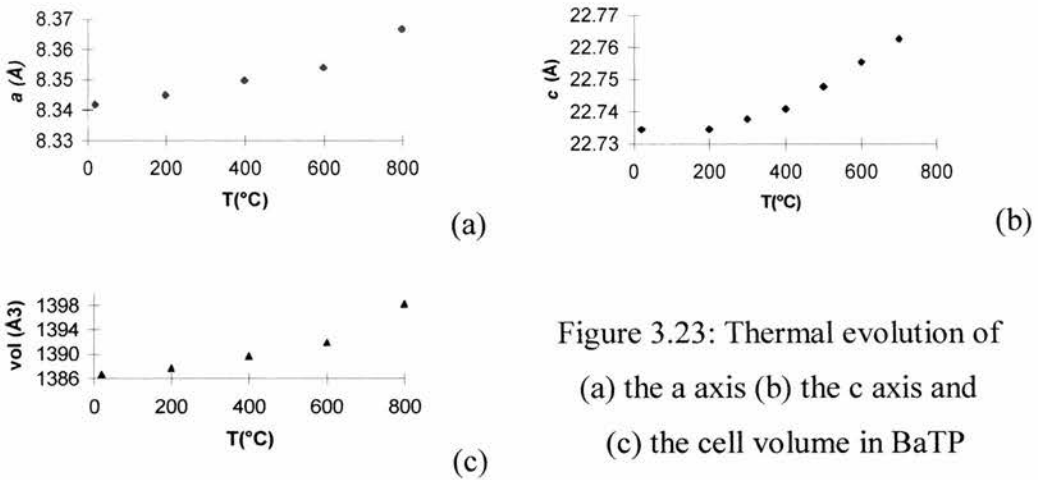


Figure 3.23: Thermal evolution of
(a) the a axis (b) the c axis and
(c) the cell volume in BaTP

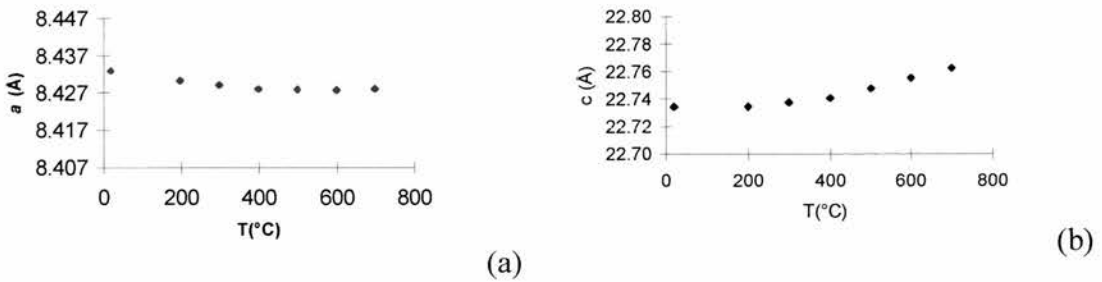
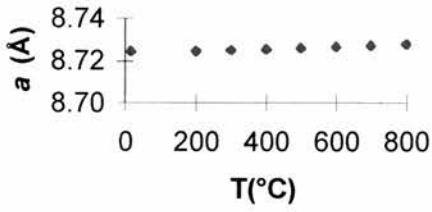
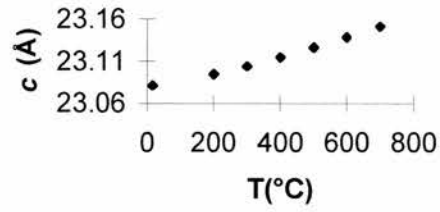


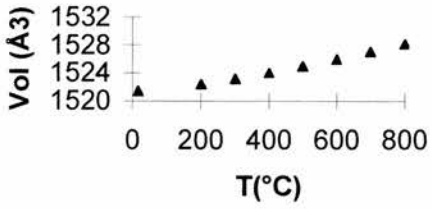
Figure 3.24: Thermal evolution of
(a) the a axis (b) the c axis and
(c) the cell volume in KNTP



(a)



(b)



(c)

Figure 3.25: Thermal evolution of

(a) the a axis (b) the c axis and

(c) the cell volume in CaSrZP

Note that for figures 3.23-3.25 the scales have been chosen to reflect a similar % change. As can be seen the behaviour of all parameters is non linear. Polynomial coefficients of thermal expansion were therefore calculated using the equations described in section 1.3 The resulting values for each material are tabulated in tableS 3.4-3.6.

Table 3.4: Experimentally determined CTE's for KNTP

T	a	c	Vol.	Average axial
20	-2.3E-06	-4.5E-07	-5.0E-06	-1.67E-06
200	-1.5E-06	7.84E-07	-2.3E-06	-0.8E-07
300	-1.1E-06	1.47E-06	-7.5E-07	-0.25E-06
400	-7.0E-07	2.16E-06	7.6E-07	0.25E-06
500	-2.9E-07	2.84E-06	2.27E-06	0.76E-06
600	1.25E-07	3.53E-06	3.77E-06	1.26E-06
700	5.36E-07	4.21E-06	5.28E-06	1.76E-06

Table 3.5: Experimentally determined CTE's for BaTP

T	a	c	Vol.	Average axial
20	4.98E-07	-1.8E-06	-8.3E-07	-0.271E-06
200	1.94E-06	3.16E-07	4.21E-06	1.4E-06
300	2.74E-06	1.51E-06	7.01E-06	2.34E-06
400	3.55E-06	2.69E-06	9.81E-06	3.27E-06
500	4.35E-06	3.88E-06	12.6E-06	4.2E-06
600	5.15E-06	5.07E-06	15.4E-06	5.1E-06
700	5.95E-06	6.26E-06	18.2E-06	6.1E-06
800	6.75E-06	7.45E-06	21.0E-06	7.0E-06

Table 3.6: Experimentally determined CTE's for CaSrZP

T	a	c	Vol.	Average axial
20	1.51E-07	3.12E-06	3.42E-06	1.13E-06
200	3.29E-07	3.82E-06	4.48E-06	1.39E-06
300	4.28E-07	4.21E-06	5.07E-06	1.66E-06
400	5.26E-07	4.6E-06	5.66E-06	1.89E-06
500	6.25E-07	4.99E-06	6.25E-06	2.08E-06
600	7.24E-07	5.38E-06	6.84E-06	2.28E-06
700	8.22E-07	5.77E-06	7.43E-06	2.38E-06
800	9.21E-07	6.16E-06	8.02E-06	2.64E-06

BaTP was the first material chosen to investigate the effect of order of cations and vacancies on the thermal expansivity. It shows an expansion of the *c* axis, contrary to that seen in SrTP, suggesting that the ordering of MI cations and vacancies, onto MIa and MIb sites respectively in SrTP is influential in allowing any behaviour other than expansion along the *c* axis, rather than the half occupied MI sites found in BaTP. This can be seen by comparing values for the parameter D, the “size” of the MI site in BaTP (ie between adjacent O2 planes along the *c* axis) vs. SrTP. Within BaTP D increases from 4.53 to 4.55 Å for each MI site over the temperature range RT to 800°C. This represents a very small expansion compared to the behaviour of the occupied site in SrTP which increases from ~4.14 to 4.35Å and the vacancy which contracts from 4.48 to 4.31Å. In other words, the partial occupancy of the MI sites in BaTP (R-3c) restricts the compression of the vacant sites. In both BaTP and KNTP there was no evidence for less than 50% occupancy of the MI sites, nor location of extra-framework cations at any other site, at any temperature studied.

KNTP exhibits unusual behaviour, its volume coefficient of thermal expansion of -5.0×10^{-6} at 20°C being quite strong before zero contraction at 300°C, returning to a strong expansion of 5.3×10^{-6} at 700°C. KNTP also shows a *c* axis expansion, increasing from 22.734Å to 22.763Å, with D increasing from 4.425 to 4.441Å. This, like the behaviour of BaTP shows a very small change compared to that of the fully occupied MI sites in NaTP (R-3c) which expand from 3.90 to 4.08 Å. Finally the investigation of CaSrZP, supposedly a zero expansion material, shows a small but significant volume expansion. This is perhaps due to the differing methods of synthesis: the original method used was a sol-gel preparation¹⁴, in contrast to the solid state reaction used in this study. D for the

occupied sites increases from 4.00 to 4.08Å, compared to 4.14 to 4.35Å for SrTP and for the vacant sites it increases more weakly from 4.39 to 4.41Å compared to the contraction in SrTP from 4.48 to 4.31Å. This particular material was originally devised to combine the opposite behaviour of CaZP ($-\alpha_a, +\alpha_c$) and SrZP ($+\alpha_a, -\alpha_c$). Each occupied MI site either contains one Sr or one Ca ion, so the site behaviour represents an average of the influence of each.

ii) The Alamo Model

Values of the parameters ϕ_1 , ϕ_2 , θ_1 , θ_2 , Δ , Ω_1 and Ω_2 for BaTP and KNTP are presented in figure 3.26 below.

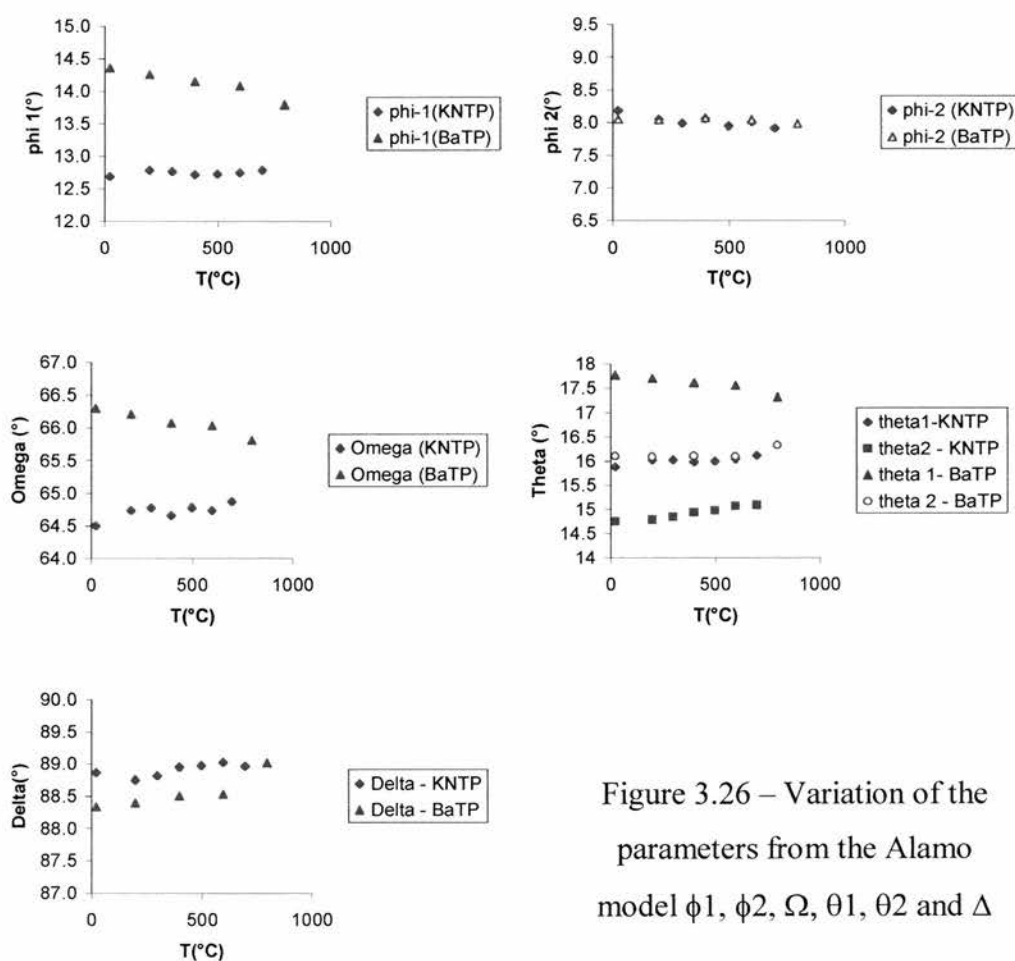


Figure 3.26 – Variation of the parameters from the Alamo model ϕ_1 , ϕ_2 , Ω , θ_1 , θ_2 and Δ

The key trends are: for KNTP; ϕ_1 shows a very slight decrease over the whole range, ϕ_2 remain constant, leading to an increasing Ω , the octahedron becoming less regular; θ_1 and θ_2 both increasing, leading to a constant Δ , the tetrahedron remaining rigid.

This behaviour shows some parallels to the previously studied NaTP and NbTP systems. θ_1 and θ_2 all increase leading to a constant Δ , and rigid tetrahedra. Ω increases in all three systems, with increases in ϕ_1 in both NaTP and NbTP being greater than in KNTP. The increase in NbTP is only marginally greater, but that of NaTP is significantly so, suggesting a correlation between the occupancy of the sites and the strength of rotation.

For BaTP ϕ_1 decreases and ϕ_2 remains constant causing Ω to decrease slightly, the octahedron becoming more regular; θ_1 decreases slightly while θ_2 remains constant, leading to an increasing Δ ; the tetrahedron becoming more regular. This behaviour is closer to that of SrTP which also shows decreasing Ω and increasing Δ . It must be stressed, however, that in all the cases of BaTP, KNTP and NbTP where there is disordering of the MI vacancies, or completely vacant sites, the magnitudes of *all* the angular changes in the Alamo model are *much* smaller than those in NaTP or SrTP which have completely filled MI or MIa sites. This re-emphasises the fundamental mechanism of the polyhedral rotations being driven by expansion of the MI sites. It is interesting to note, however that the most significant ϕ rotations occur for ϕ_1 - i.e.: the O1 face of the TiO_6 octahedron, which is *not* bonded to the MI site.

iii) Consideration of Ti-O-P Angles

The thermal evolution of the Sc-O-W angles has been suggested to be important by Evans et al in $\text{Sc}_2(\text{WO}_4)_3$ and the corresponding Ti-O-P angles have been considered in studies of NaTP and SrTP in section 3.2. NaTP had a negative α_a with the Ti-O1-P angle contracting and SrTP had a positive α_a with the Ti-O1-P angle expanding. The behaviour of the angles in KNTP, CaSrZP and BaTP correlate well with the thermal expansivity. In this study all of the Ti-O-P angles are considered: in the R-3c cases there are two; Ti-O1-P and Ti-O2-P which are plotted in fig 3.27.

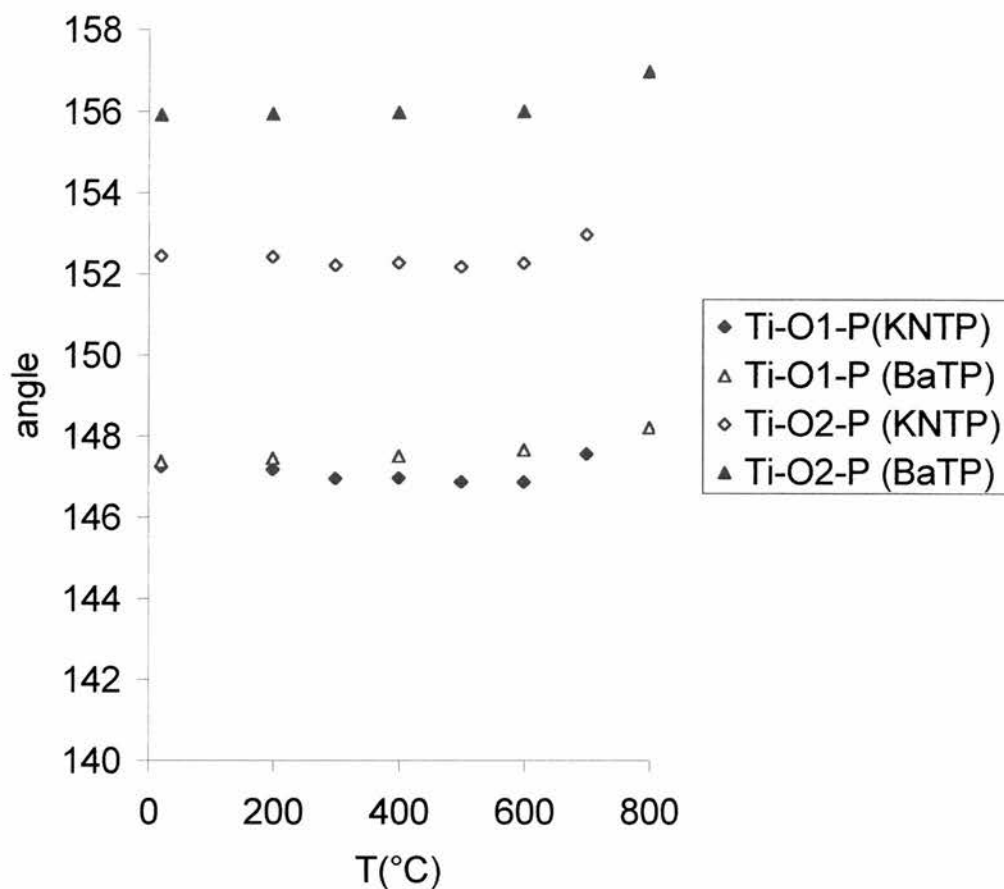


Figure 3.27 - Thermal evolution of the interpolyhedral Ti-O1-P and Ti-O2-P angles for KNTP and BaTP

An opening of both of these angles would reflect an expansion of the a axis. Within KNTP, neither Ti-O1-P or Ti-O2-P change significantly, correlating with the minimal expansion of the a axis. Within BaTP, both Ti-O1-P and Ti-O2-P increase slightly.

Within the R-3 systems there are four angles. It is the angles associated with the MI sites (Zr-O3-P and Zr-O4-P, figure 3.28) which vary most strongly in CaSrZP, both of which undergo a 2° expansion over the range 20-800°C. In SrTP the strongest change was in the angles around the Ti(1) site (ie: associated with only the occupied MI site).

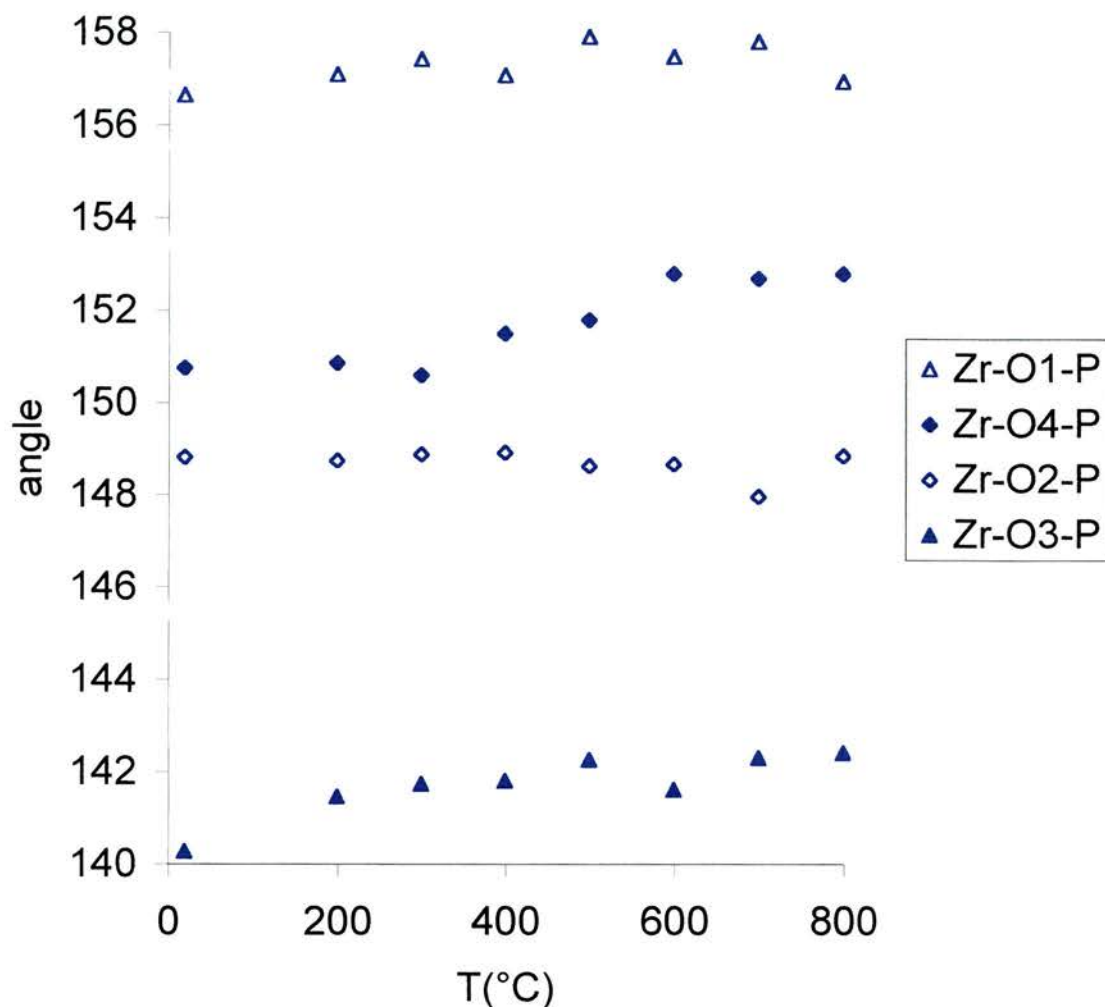


Figure 3.28 – Thermal evolution of the interpolyhedral Zr-O1-P, Zr-O4-P, Zr-O2-P and Zr-O3-P angles for CaSrZP

Ti-O1-P varies from 152.7° to 162° and Ti-O3-P from 143.4° to 155.3° . This differing, and much more pronounced effect is due to either the mixed occupancy of Ca and Sr on the MI sites or substitution of Zr for Ti (note that in the series $A_{0.5}M_2(PO_4)_3$ ($A = \text{Ca, Sr}$; $M = \text{Ti, Zr, Hf, Sn}$) the thermal expansion coefficients are strongly influenced by the nature of M).

In NaTP it was noted that the negative α_a appears to correlate with the contraction of the Ti-O1-P angle. However, in that case, the Ti-O2-P angle expands by a similar amount. Hence, whether these interpolyhedral angles can be considered as a useful parameter in describing the thermal expansion behaviour of the NZP family is still an open question. This question is explored in the series $MTi_2(PO_4)_3$ ($M = \text{Li, Na, K}$) in section 3.6.

3.5.3 Conclusions

Preparation and study of the samples KNTP and BaTP with disordering on the MI sites, has revealed that both materials, although low expansion, do exhibit a significant *c* axis expansion on heating. Ordering of cations and vacancies, as occurs in the R-3 phase SrTP which exhibits zero *c*-axis expansivity, appears to be influential in understanding the opposite anisotropy of R-3 and R-3c structured samples.

It appears that the method of preparation of CaSrZP may affect its properties. Previous studies had revealed this material to be essentially zero expansion when prepared by a sol gel method. However, this sample, prepared by a solid state method, was found to expand weakly.

3.6 A Neutron Powder Diffraction Study of $\text{KTi}_2(\text{PO}_4)_3$ (KTP) and $\text{LiTi}_2(\text{PO}_4)_3$ (LiTP)

This study compares $\text{KTi}_2(\text{PO}_4)_3$ (KTP) and $\text{LiTi}_2(\text{PO}_4)_3$ (LiTP), an important ionic conductor²⁷, with the previously studied NaTP and provides the first detailed high temperature structural study of both materials. Both Alamo's model and the high temperature cation disorder in LiTP are investigated. The behaviour of the interpolyhedral Ti-O-P angles, which were identified by Evans et al¹³ as being an important factor in explaining the behaviour of some negative thermal expansion materials is also discussed.

3.6.1 Experimental

Samples were synthesised using stoichiometric quantities of K_2CO_3 (Aldrich, 99+%), TiO_2 (Anatase, Aldrich, 99.9+%), Li_2CO_3 (Aldrich, 99+%) and $(\text{NH}_4)_2\text{HPO}_4$ (Aldrich, 99%). Starting materials were dried and ground under acetone before being heated in air to 200°C for 18h, 600°C for 6h and 900°C for 12h. Each sample was then pelleted and sintered for 24h at 1000°C followed by 24h at 1100°C and 24h at 1150°C. Sample purity was checked on a STOE STADI-P powder diffractometer operating in transmission mode using $\text{CuK}_{\alpha 1}$ radiation.

Powder neutron diffraction data for both KTP and LiTP were obtained on the HRPD instrument at the ISIS facility, CLRC Rutherford Appleton Laboratory. Data were collected for 60 μ Ah at 20°C then every 100°C from 200°C to 800°C, again for 60 μ Ah at each temperature. Data were refined using the GSAS program¹⁸ and typically consisted of 6308 data points, 38 variables, and 487 reflections over a d-spacing range of 0.705 to 2.49Å for KTP and 6310 data points, 38 variables, and 414 reflections over a d-spacing range of 0.715 to 2.49Å for LiTP. For all of these refinements a double-exponential pseudo-Voigt peak profile function was used. Anisotropic temperature factors were used for all refinements of KTP, although these led to unstable refinements in LiTP. This was due to the disordering of Li over two crystallographic sites as described later. In that case anisotropic temperature factors were therefore used for Ti, P and O atoms only. Attempts to refine both isotropic temperature factors and site occupancies for Li led to unstable refinements, therefore both Li's were constrained to have the same temperature factor as the isotropic equivalent on K in KTP at the same temperature. The occupancy of the MII site in LiTP was constrained to be equal to 1/3 [1-occ.(MI)]. A typical Rietveld plot is shown in figure 3.29.

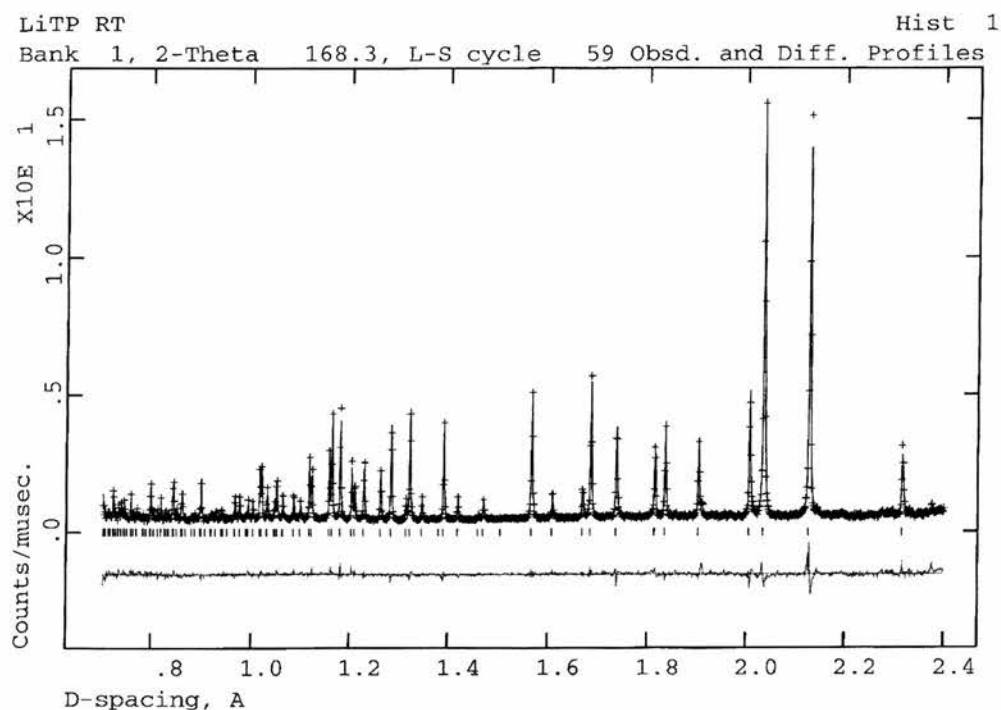


Figure 3.29 – A typical Rietveld plot for $\text{LiTi}_2(\text{PO}_4)_3$ at 20°C

3.6.2 Results and Discussion

i) Coefficients of thermal expansion

The unit cell parameters and atomic co-ordinates at the highest and lowest temperatures are shown in Table x for LiTP and Table x for KTP. Plots of the thermal behaviour of unit cell parameters and volume are shown in figure x.

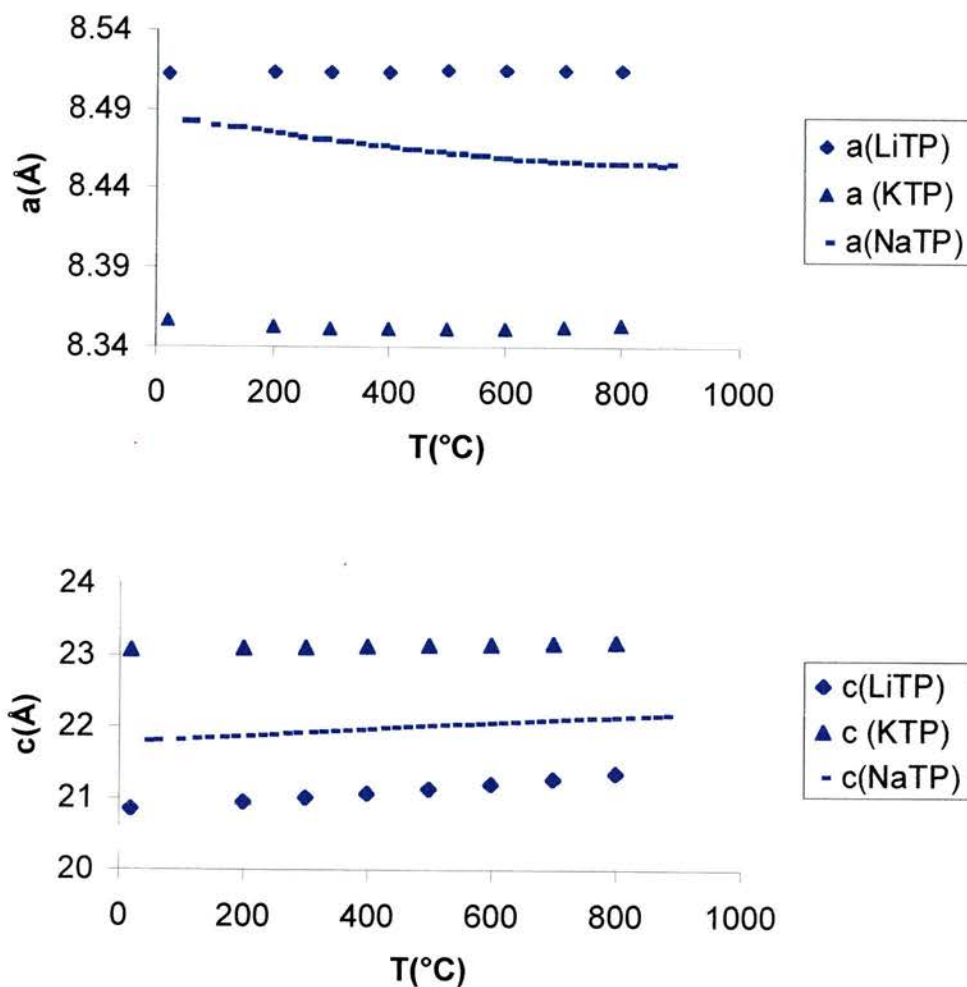


Figure 3.30 - Thermal evolution of lattice parameters for NaTP, LiTP and KTP
a axis and (b) c axis

As can be seen, the behaviour of all parameters is non linear. Polynomial coefficients of thermal expansion were therefore calculated as described previously.

The resulting values for each material are tabulated in table A1.11 in the Appendix, and their coefficients of thermal expansion (CTE's) tabulated in tables 3.7 and 3.8.

Table 3.7: Experimentally determined CTE's for KTP ($\times 10^{-6}\text{C}^{-1}$)

T	α_a	α_c	α_v	$\alpha_L^{\$}$
20	-3.20	5.89	-0.8	-0.27
200	-1.90	6.20	2.35	0.78
300	-1.10	6.38	4.10	1.37
400	-0.41	6.55	5.84	1.95
500	0.31	6.72	7.59	2.53
600	1.04	6.90	9.34	3.11
700	1.76	7.07	11.1	3.70
800	2.48	7.25	12.8	4.27

Table 3.8: Experimentally determined CTE's for LiTP ($\times 10^{-6}\text{C}^{-1}$)

T	α_a	α_c	α_v	$\alpha_L^{\$}$
20	0.748	30.8	25.7	8.57
200	0.638	30.8	28.5	9.50
300	0.577	30.8	30.0	10.0
400	0.516	30.8	31.5	10.5
500	0.455	30.8	33.1	11.0
600	0.394	30.8	34.6	11.5
700	0.333	30.8	36.1	12.0
800	0.272	30.8	37.7	12.6

$$\$ \alpha_L = 1/3 \alpha_v$$

These results are in very good agreement with those of Huang³, which are tabulated in Table 3.9.

Table 3.9: Comparison of average CTE's with Huang's results³

	$\alpha_a (\times 10^{-6}\text{C}^{-1})$	$\alpha_c (\times 10^{-6}\text{C}^{-1})$
LiTP – this study	0.49	30.8
LiTP – Huang's results [†]	-0.05	30.59
NaTP – this study	-5.3	20.8
NaTP – Huang's results [†]	-3.88	20.74
KTP – this study	-0.13	6.62
KTP – Huang's results [†]	0.21	5.73

$$^{\dagger} \text{ T range} = 25\text{-}1000^{\circ}\text{C}$$

The overall conclusion is that substitution of a larger cation decreases the thermal expansion anisotropy (i.e. the difference between α_a and α_c). However, LiTP does shows near-zero a axis expansion, although its c axis expansion is significantly greater

than that of NaTP ($30.8 \text{ cf. } 20.8 \times 10^{-6} \text{ } ^\circ\text{C}^{-1}$). This unusual behaviour appears to be due to the disordering of Li from the MI to MII sites, as discussed below.

ii) Disorder of Li

In LiTP there is a disordering of Li over the MI and MII sites which increases with temperature as shown in Table A1.9. LiTP remains the only material studied here to show disordering of the MI cations onto the MII site. Moreover, a similar powder neutron diffraction study on $\text{LiGe}_2(\text{PO}_4)_3$ by Brochu et al¹¹ did not show any evidence for occupancy of the MII site at any temperature. This disordering effect had been suggested by Kutty et al²⁶ as being a possible explanation for the c axis contraction in SrZP. LiTP however, exhibits the strongest c axis expansion of any material studied here ($30.8 \times 10^{-6} \text{ } ^\circ\text{C}^{-1}$), which does not appear to follow from this suggestion. Delmas et al²⁸ carried out a full structural study of $\text{Li}_3\text{Ti}_2(\text{PO}_4)_3$ and found that all the Li cations occupied the MII sites in preference to the MI sites. On comparing $\text{LiTi}_2(\text{PO}_4)_3$ to $\text{Li}_3\text{Ti}_2(\text{PO}_4)_3$ they observed an increase in the c axis but a decrease in the a axis. They suggested that the increased repulsion between the layers of oxygen ions around MI led to a much larger c parameter. In this case it would appear that disordering of the Li cations onto the MII sites produces the same effect, leading to a larger than expected α_c . LiTP shows by far the greatest expansion in the MI site size (defined as D, the O2-O2 distance along the c axis), expanding from 3.36(1) to 3.66(1)Å compared to 3.90(1) to 4.08(1)Å in NaTP and 4.55(1) to 4.60(1)Å in KTP. The MI-O bond expands from 2.264(2) to 2.388(2)Å in LiTP compared to 2.466(4) to 2.569(5)Å in NaTP and 2.749(2) to 2.773(2)Å in KTP. It is normal in NZP systems for a positive α_c to lead to a negative α_a , via couple rotations of linked polyhedra. In this case it would appear that this tendency is counterbalanced by the increasing occupancy of the MII sites, which acts to inhibit a axis contraction, leading to the observed near zero α_a .

iii) The Alamo Model

The expansivities of the TiO_6 and PO_4 polyhedra are insignificant over the temperature range studied. Values of the parameters ϕ_1 , ϕ_2 , θ_1 , θ_2 , Δ , Ω_1 and Ω_2

for LiTP and KTP as a function of temperature are shown in figure 3.31-3.36. The figures detailing the changes in angles for NaTP are also provided as a comparison, but unfortunately due to problems with saving MSWord documents it has not been possible to provide them on the same plots.

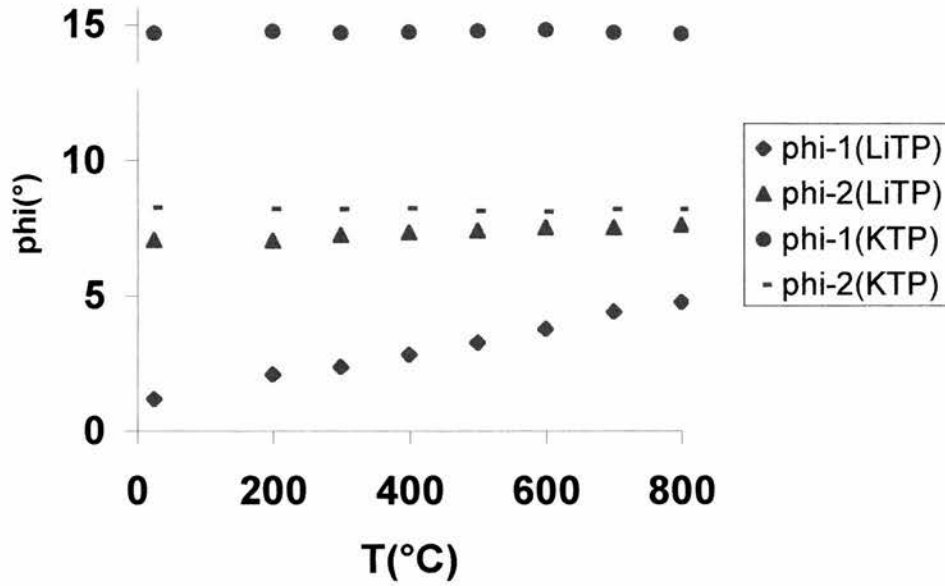


Figure 3.31: Variation of the parameters (a) ϕ_1 and ϕ_2 and for KTP and LiTP

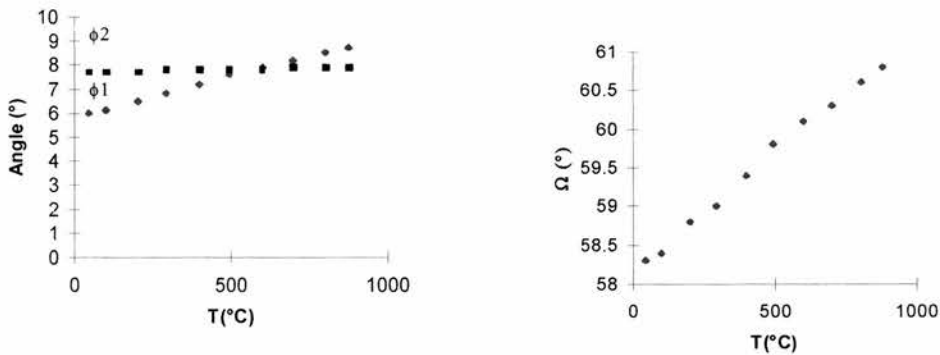


Figure 3.32: Variation of the parameters (a) ϕ_1 and ϕ_2 and (b) Ω for NaTP

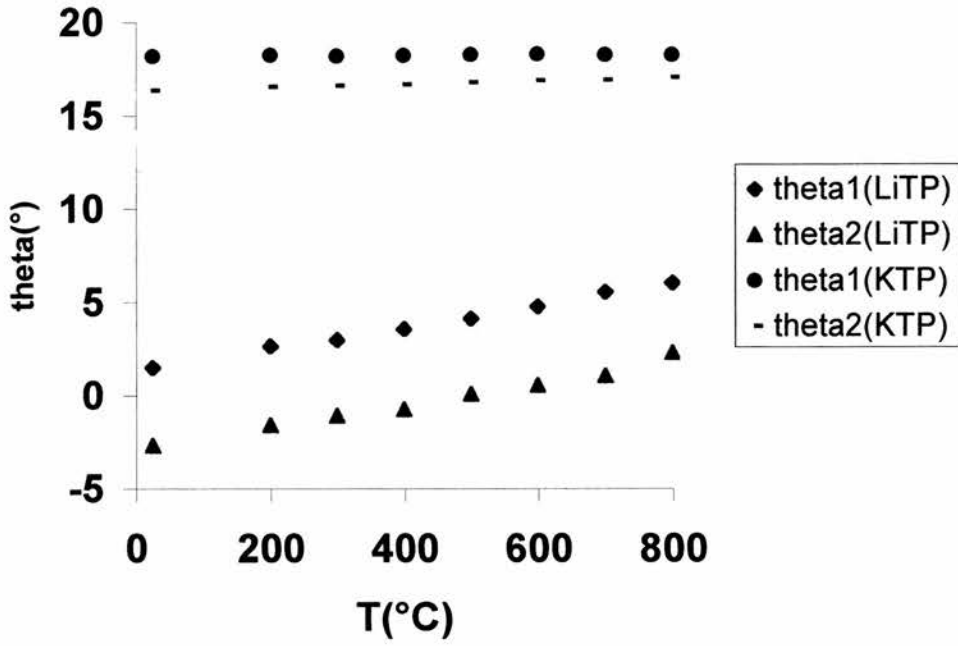


Figure 3.33: Variation of the parameters θ_1 and θ_2 for KTP and LiTP

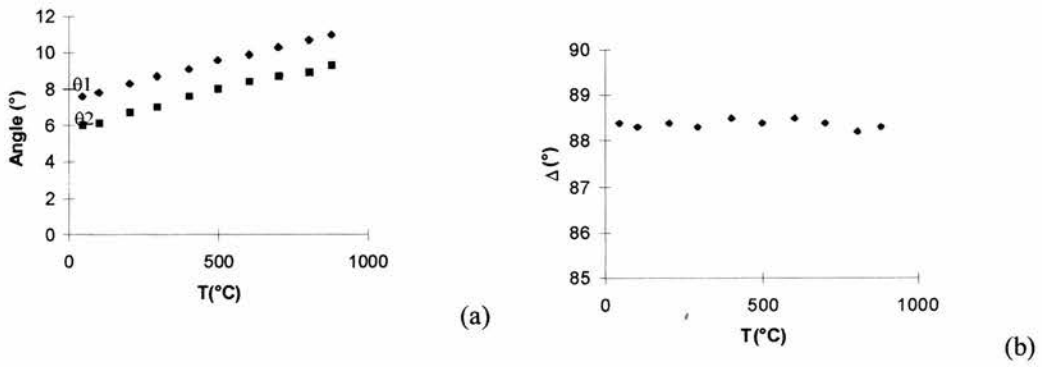
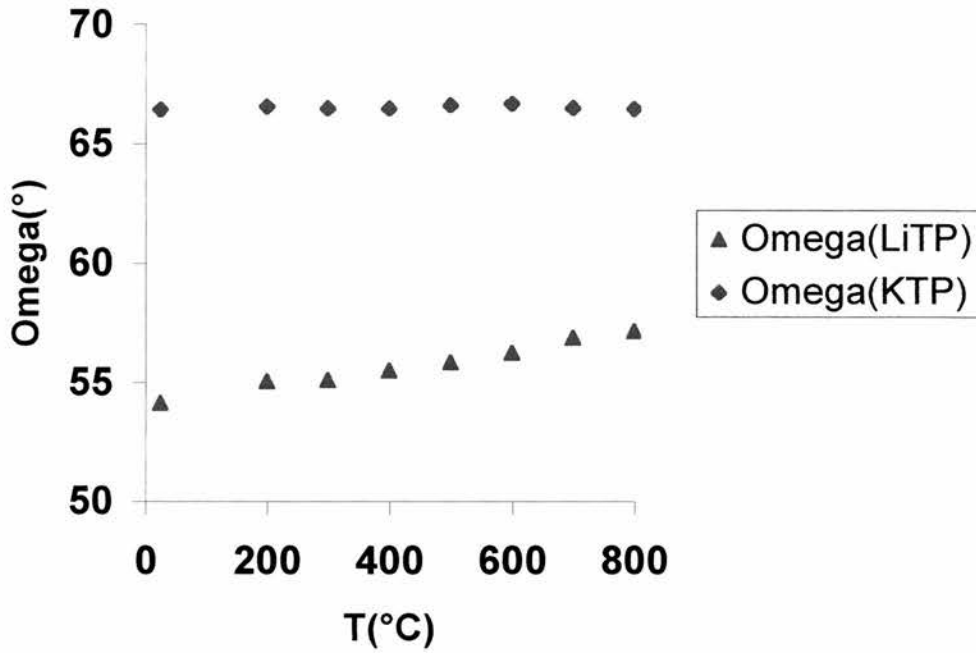
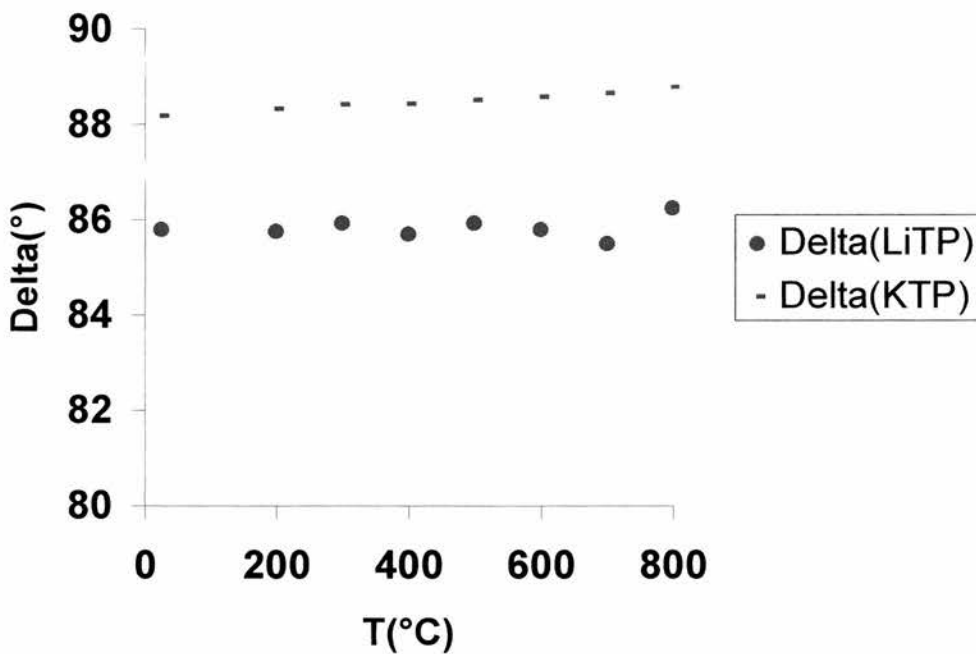


Figure 3.34: Variation of the parameters (a) θ_1 and θ_2 and (b) Δ for NaTP

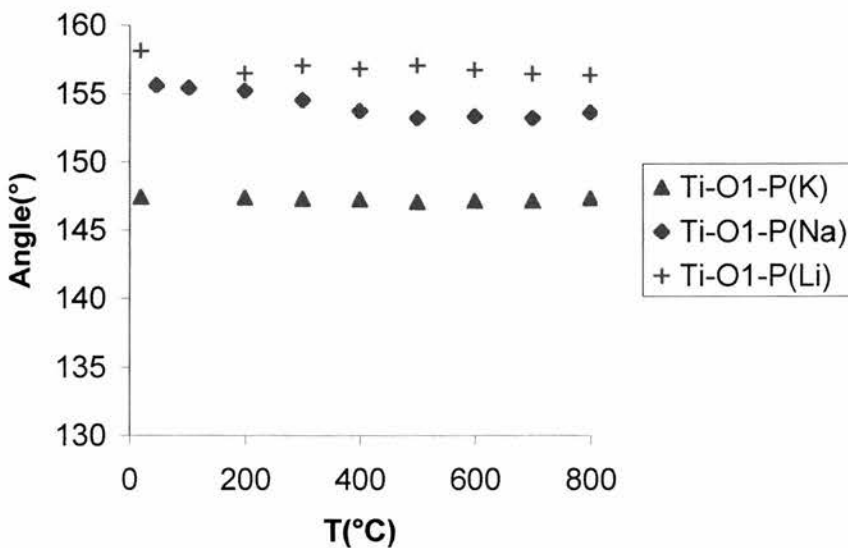
Figure 3.35 – Variation of the angle Ω for KTP and LiTPFigure 3.36 – Variation of the angle Δ for KTP and LiTP

In LiTP ϕ_1 increases strongly and ϕ_2 increases only slightly, leading to an increase in Ω , the octahedron becoming more regular. The values of these changes are almost identical to those in NaTP. However in KTP, both ϕ_1 and ϕ_2 remain virtually constant, leading to no change in Ω .

Consideration of the angles relating to the tetrahedra (θ_1 and θ_2) shows the same trend: a great similarity between NaTP and LiTP and a difference from KTP. θ_1 and θ_2 both increase strongly at much the same rate in both NaTP and LiTP, leading to a virtually rigid PO_4 tetrahedron. Within KTP, θ_1 remains constant and θ_2 increases very slightly leading to a small increase in Δ . Overall it appears that there is little distortion of the tetrahedra, but that these rotate in LiTP and NaTP, but remain in the same position in KTP. It is likely that the relatively small changes in the Alamo parameters for KTP results from the fact that these values (i.e. ϕ and θ) are quite high in the room temperature structure. In other words, the structure is already under severe strain and distortion due to the large size of the MI site, and will not distort much further – hence the relatively smaller values of α_a and α_c for KTP vs. NaTP.

iv) Consideration of Ti-O-P Angles

Evans et al have suggested that interpolyhedral angles ($\text{M-O-M}'$) change significantly in some negative thermal expansion materials¹³. The angle Ti-O1-P in both LiTP and KTP remains constant, as does Ti-O2-P in KTP (figure 3.37).



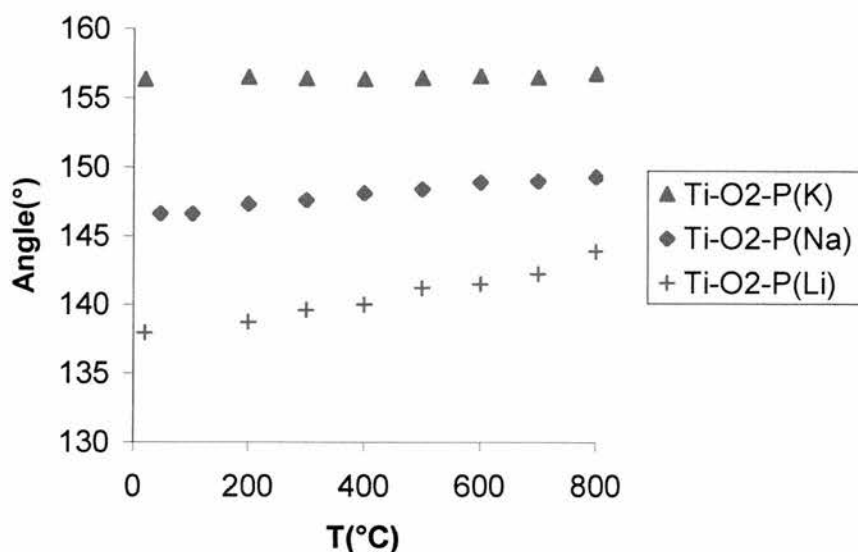


Figure 3.37 - Thermal evolution of the interpolyhedral Ti-O1-P and Ti-O2-P angles for KTP, NaTP and LiTP

However, Ti-O2-P in LiTP shows a large increase. This can be correlated to the expansion of the *c* axis as the angle is oriented almost parallel to the axis.

The previous studies on NbTP (section 3.4) showed a small contraction in *a* and expansion in *c*, but little change in either Ti-O-P angle - any change was smaller than the Rietveld esd's. These angles do not change enough to be an indicator for the thermal expansion properties in the NZP family.

3.6.3 Conclusions

In LiTP, there is a significant disordering of Li cations from the MI to MII site on heating which had not been previously reported from X-ray diffraction studies and has not been seen in any other NZP phases. This phenomenon resembles that observed in changing from $\text{LiTi}_2(\text{PO}_4)_3$ to $\text{Li}_3\text{Ti}_2(\text{PO}_4)_3$, in which the former has the MI sites fully occupied and the latter the MII sites fully occupied. Consequently, α_c for LiTP is very high due to relaxation of the MI sites from a very small size ($D=3.36\text{\AA}$) to a larger size ($D=3.66\text{\AA}$) as Li migrates from MI to MII sites. Comparing the series LiTP, NaTP, KTP in terms of increasing cation size, the results are in agreement with those of Huang, in that as the cation size increases thermal expansivity decreases. This effect appears to be due to the amount of "strain" present in the structure with respect to MI cation size; for the

larger K^+ cation the MI site is large, polyhedral tilts (ϕ and θ) are consequently large, and changes in ϕ and θ are small, leading to the smaller α_a and α_c values.

3.7: Overall Conclusion

- The main focus in this chapter is the length of the M-O bond and its effect on the MI site. The behaviour of this site is critical to the thermal expansion properties of each material.
- The thermal expansion within the NZP system is driven by expansion of the M-O bond which governs the size of the trigonal prismatic site along the c axis.
- In the R-3 system there are two MI sites, one of which is occupied and the other vacant. The differing behaviour of these sites accounts for the opposite TE behaviour to R-3c materials.
- Within LaTP both sites contract slightly due to the partial occupancy of the La site, whereas in the case of SrTP a more or less equal and opposite expansion of the filled and vacant sites was observed.
- $NbTi(PO_4)_3$, in which the MI sites are completely vacant, is a negative thermal expansion material over the range $25^\circ C < T < 600^\circ C$. This is due to the contraction of the a and b axes being greater than the expansion of the c axis.
- The c axis only contracted in cases where there was an ordering of cations and vacancies.
- α_c for LiTP is very high due to relaxation of the MI sites from a very small size ($D=3.36\text{\AA}$) to a larger size ($D=3.66\text{\AA}$) as Li migrates from MI to MII sites.
- The method of preparation may affect the TE properties. A sample of CaSrZP prepared by a solid state method, was found to expand weakly whereas previous workers suggested it was essentially zero expansion when prepared by a sol gel method.
- As the cation size increases over the series LiTP, NaTP, KTP thermal expansivity decreases.
- The interpolyhedral Ti-O-P angles do not change enough to be an indicator for the thermal expansion properties in the NZP family, possibly because the polyhedra distort significantly.

3.8: References

- 1) J. P. Boilot, J. P. Salanie, G. Desplanches and D. Le Potier, *Mater. Res. Bull.*, 1979, **14**, 1469
- 2) E. Breval and D. K. Agrawal, *Brit. Ceram. Trans.*, 1995, **94**, 27
- 3) C.-Y. Huang, D. K. Agrawal and H. A. McKinstry, *J. Mater. Sci.*, 1995, **30**, 3509
- 4) S. Y. Limaye, D. K. Agrawal and H. A. McKinstry, *J. Amer. Ceram. Soc.*, 1987, **70**, C232
- 5) D.K. Liu, L-J. Lin, C-J. Chen, *J. Appl. Cryst.*, 1995, **28**, 508
- 6) K. V. G. Kutty, R. Asuvathraman, C.K. Mathews and U.V. Varadaraju, *Mater. Res. Bull.*, 1994, **29**, 1009
- 7) T. Oota and I. Yamai, *J. Amer. Ceram. Soc.*, 1986, **69**, 1
- 8) J. Alamo, *Solid State Ionics*, 1993, **63-65**, 547
- 9) G. E. Lenain, H. A. McKinstry, J. Alamo and D. K. Agrawal, *J. Mater. Sci.*, 1987, **22**, 17
- 10) J. L. Rodrigo, P. Carrasco and J. Alamo, *Mater. Res. Bull.*, 1989, **24**, 611
- 11) M. Alami, R. Brochu, J.L. Soubeyroux, P. Gravereau, G. Le Flem, and P. Hagemuller, *J. Sol. Stat. Chem*, 1991, **90**, 185
- 12) J. Alamo and J. L. Rodrigo, *Mater. Res. Bull.*, 1992, **27**, 1091
- 13) J.S.O. Evans, T. A. Mary and A.W. Sleight, *J. Solid State Chem.*, 1998, **137**, 148
- 14) G.E. Lenain, H.A. McKinstry and D.K. Agrawal, *J. Am. Ceram. Soc.*, 1985, **68**, C224
- 15) D.K. Agrawal, C.Y. Huang, and H.A. McKinstry, *Intl. J. Thermophys.* , 1991, **12**, 697
- 16) S. Komarmeni, *Int. J. High Technol. Ceram.*, 1988, **4**, 31
- 17) J. Rodriguez-Carvajal, *Physica B*, 1993, **192**, 55
- 18) A. C. Larson and R. B. Von Dreele, Los Alamos National Laboratory Report No. LA-UR-86-748, 1987
- 19) S. Senbhagaraman, T. N. Guru Row and A. M. Umarji, *J. Mater. Chem.*, 1993, **3**, 309

- 20) J.D. Jorgensen, J. Faber Jr., J. M. Carpenter, R.K. Crawford, J.R. Haumann, R.L. Hitterman, R. Kleb, G.E. Ostrowski, F.J. Rotella and T.G. Worlton, *J. Appl. Crystallogr.*, 1989, **22**, 321
- 21) S. Senbhagaraman and A. M. Umarji, *J. Solid State Chem.*, 1990, **85**, 169
- 22) J. Alamo and J. L. Rodrigo, *Solid State Ionics*, 1993, **63-65**, 678
- 23) J. S. O. Evans, T. A. Mary, T. Vogt, M. A. Subramanian, A. W. Sleight, *Chem. Mater.*, 1996, **8**, 2809
- 24) R.I. Smith and S. Hull, "User Guide for the Polaris Powder Diffractometer at ISIS", Report RAL-TR-97-038, Rutherford Appleton Laboratory (1997)
- 25) F.J. Berry, C. Greaves and J.F. Marco, *J. Solid State Chem.*, 1992, **96**, 408
- 26) K. V. G. Kutty, R. Asuvathraman and R. Sridharan, *J. Mater. Sci.*, 1998, **33**, 4007
- 27) H. Aono, E. Sugimoto, Y. Sadaoka, N. Imanaka and G. Adachi, *J. Electrochem. Soc*, 1990, **137**, 1023
- 28) C. Delmas, A. Nadiri and J.L. Soubeyroux; *Solid State Ionics*, 1988, **28-30**, 419

3.9: Publications arising from this chapter

- 1) D. A. Woodcock, P. Lightfoot, C. Ritter, *Chem. Commun.*, 1998, 107
- 2) P. Lightfoot, D. A. Woodcock, J. D. Jorgensen and S. Short, *Int. J. Inorg. Mater.*, 1999, **1**, 53
- 3) D. A. Woodcock, P. Lightfoot, and R. I. Smith, *Mater. Res. Soc. Symp. Proc.*, 1999, **547**, 191
- 4) D. A. Woodcock, P. Lightfoot, and R. I. Smith, *J. Mater. Chem*, 1999, **10**, 2631
- 5) D. A. Woodcock and P. Lightfoot, *J. Mater. Chem*, 1999, **11**, 2907

Chapter 4: Materials with the Scandium Tungstate Structure

4.1 Introduction

$\text{Sc}_2(\text{WO}_4)_3$ has been known to exhibit negative thermal expansion for some time: its axial contraction was reported by Balashov¹ in 1975 with $\alpha_a = -5.83$, $\alpha_b = +4.03$, $\alpha_c = -1.91$ and $\alpha_v = -3.64 \times 10^{-6} \text{ } ^\circ\text{C}^{-1}$. Since then dilatometric and X-ray diffraction studies have been carried out on many members of the $\text{A}_2\text{M}_3\text{O}_{12}$ family ($\text{A} = \text{Al}, \text{Fe}, \text{Sc}, \text{Lu}, \text{In}, \text{Y}, \text{M} = \text{Mo}, \text{W}$). Materials with $\text{A} = \text{Sc}, \text{Al}, \text{Fe}, \text{Lu}, \text{In}$ and $\text{Y}_{0.5}\text{Al}_{0.5}, \text{Sc}_{0.5}\text{Al}_{0.5}$ have led to a series of molybdates and tungstates with a wide range of thermal expansion properties². However, it is only recently that the technique of neutron powder diffraction has been employed to elucidate the mechanism and factors governing the magnitude of expansivity within this system. Studies on $\text{Sc}_2(\text{WO}_4)_3$ ³, $\text{Lu}_2(\text{WO}_4)_3$ ⁴ and, since this work was carried out, $\text{Y}_2(\text{WO}_4)_3$ ⁵ have been published.

The scandium tungstate structure consists of a corner sharing network of ScO_6 octahedra and WO_4 tetrahedra crystallising in space group Pnca . The ScO_6 octahedron shares corners with 6 WO_4 tetrahedra and the WO_4 tetrahedron shares corners with 4 ScO_6 octahedra. There are 2 crystallographically distinct W sites, one (W1) on a 2-fold axis and the other on a general position (8d). A polyhedral representation of this structure is shown in figure 4.1 below.

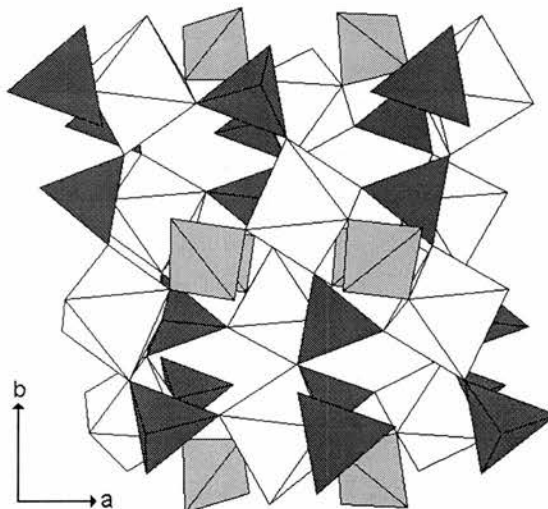


Figure 4.1 - The structure of $\text{Sc}_2(\text{WO}_4)_3$ showing ScO_6 octahedra (white), $\text{W}(1)\text{O}_4$ tetrahedra (light grey) and $\text{W}(2)\text{O}_4$ tetrahedra (dark grey).

Evans' work on $\text{Sc}_2(\text{WO}_4)_3$ itself provided many insights into the mechanism of negative thermal expansion in this material. He attempted an isotropic free refinement strategy and found that there was only a small distortion from the ideal geometry of the octahedra and tetrahedra and significant variations in the Sc-O-W angles and Sc-W non bonded distances.

As there had been little change in the geometry he was able to apply a rigid body model which led to a lower R-factor for his refinements despite having fewer variables. He also found that dilatometric measurements led to a much stronger negative thermal expansion which was attributed to microcracking of the ceramic bars caused by the anisotropic thermal expansion. Cracks which had enlarged on cooling of the annealed sample would contract on heating, enhancing the negative thermal expansion. For isotropic materials such as ZrW_2O_8 ⁶ there had been no such disagreement between the two methods. He concluded that the mechanism was due to a complex 3D twisting of rigid framework polyhedra. The tilts (two dimensional movement) and twists (three dimensional movement) are caused by the anharmonic vibrations of bridging oxygens (see fig 4.2 below) leading to a decrease in the Sc-O-W, distances leading to a shorter Sc-Sc distance and hence negative thermal expansion.

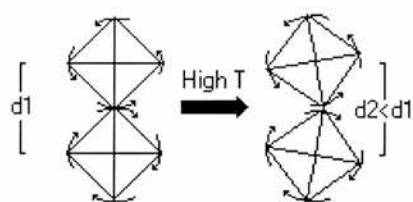


Figure 4.2 As the temperature increases, anharmonic thermal vibration occurs (curved arrows), leading to an atomic displacement, decreasing the M-O-M angle and shortening the M-M distance.

It has been suggested by Forster et al⁴ that the magnitude of thermal expansivity within the system is related to the size of the A cation. Larger A cations are suggested to lead to more negative coefficients of thermal expansion. Previous to this work $\text{Lu}_2(\text{WO}_4)_3$ ⁴ was the material with the largest cation to have been studied. The linear thermal expansion coefficient (see section 1.3) was found to be $-6.8 \times 10^{-6} \text{ } ^\circ\text{C}^{-1}$, the strongest thermal contraction to be found for this structure type. However, the upper tolerance limit for the $\text{Sc}_2(\text{WO}_4)_3$ structure is

$\text{Y}_2(\text{WO}_4)_3$, the Y^{3+} cation having an ionic radius of 1.01\AA , compared to 0.98\AA for Lu^{3+} . In this chapter, the behaviour of this material is contrasted with that of $\text{Al}_2(\text{WO}_4)_3$, the Al^{3+} radius being 0.535\AA . These materials represent the extremes of size compatibility of the A cation within this structure type, and should therefore reveal extremes of behaviour. $\text{Al}_2(\text{WO}_4)_3$ has been previously studied by Evans et al ² using both dilatometer and X-ray powder diffraction data, which revealed bulk thermal expansivities of -3 and $+2.2 \times 10^{-6}\text{C}^{-1}$, respectively. The intermediate phase $\text{YAl}(\text{WO}_4)_3$ was also reported as having an α of $5 \times 10^{-6}\text{C}^{-1}$, based on dilatometer data. In neither case were axial thermal expansion coefficients reported.

4.2: Experimental

Samples were prepared using the starting materials Al_2O_3 (99.99%, Aldrich), WO_3 (99+%, Aldrich) and Y_2O_3 (99.99%, Aldrich). $\text{Al}_2(\text{WO}_4)_3$ was synthesised using a heat treatment of 24h at 1000°C in a Pt crucible, the starting materials being intimately ground under acetone. For $\text{Y}_2(\text{WO}_4)_3$ the treatment consisted of 24h at 900°C , followed by 24h at 1000°C and 24h at 1100°C . The samples were characterised on a Philips PW3710 diffractometer using $\text{Cu K}\alpha$ radiation. This revealed the samples to be phase pure. Attempts to synthesise $\text{Nd}_2(\text{WO}_4)_3$ proved unsuccessful due to the low melting point ($\sim 900^\circ\text{C}$) of the phase mixture and the likelihood that the Nd^{3+} cation was above the upper tolerance of the $\text{Sc}_2(\text{WO}_4)_3$ structure type.

The neutron diffraction experiment was carried out on the D2B instrument at the Institut Laue Langevin, Grenoble over the temperature range $20\text{-}800^\circ\text{C}$ at a wavelength of 1.596\AA . Data were collected for approximately $3\frac{1}{2}$ h at each temperature. Data were refined using the FULLPROF ⁷ program by Dr Clemens Ritter, atom positions from Abraham and Bernstein's solution of the $\text{Sc}_2(\text{WO}_4)_3$ structure ⁸ in space group Pnca and a pseudo-Voigt profile function. Typical neutron Rietveld plots for $\text{Y}_2(\text{WO}_4)_3$ and $\text{Al}_2(\text{WO}_4)_3$ are shown in figure 4.3 and the resulting atomic co-ordinates in Appendix 2.

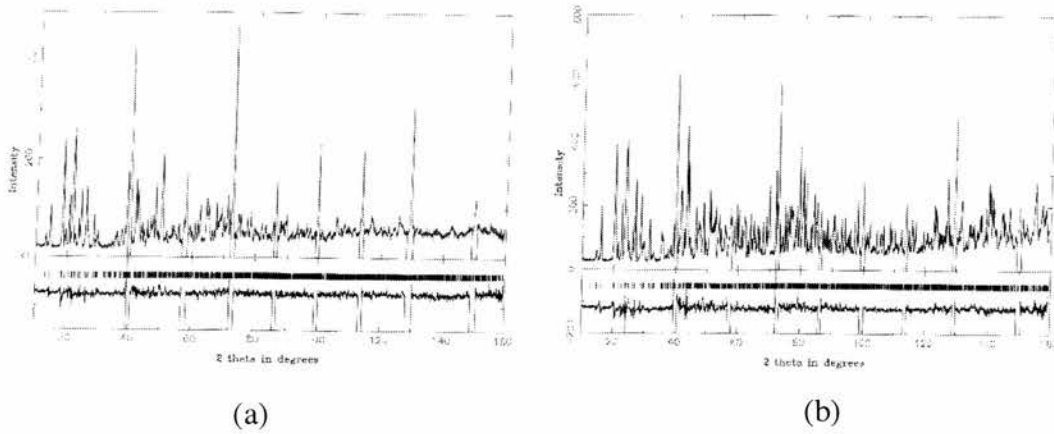


Figure 4.3: Typical neutron Rietveld plots for (a) $Y_2(WO_4)_3$ and (b) $Al_2(WO_4)_3$.

The excluded regions are due to Nb peaks from the furnace

The errors are much smaller in the $Al_2(WO_4)_3$ sample compared to $Y_2(WO_4)_3$ as the data are much better resolved at high angles. This was also the case for the X-ray data, $Al_2(WO_4)_3$ apparently being a sample of higher quality. For this reason a full anisotropic refinement of all atoms in $Al_2(WO_4)_3$ but only an isotropic refinement for $Y_2(WO_4)_3$ was carried out.

4.3 Results and Discussion

Plots of the evolution of unit cell parameters and cell volume against temperature are shown in figures 4.4 and 4.5. $Y_2(WO_4)_3$ shows negative thermal expansion along all 3 axes, the coefficients of thermal expansion are shown in table 4.1. This leads to an overall volume contraction of $-20.9 \times 10^{-6} \text{ } ^\circ\text{C}^{-1}$.

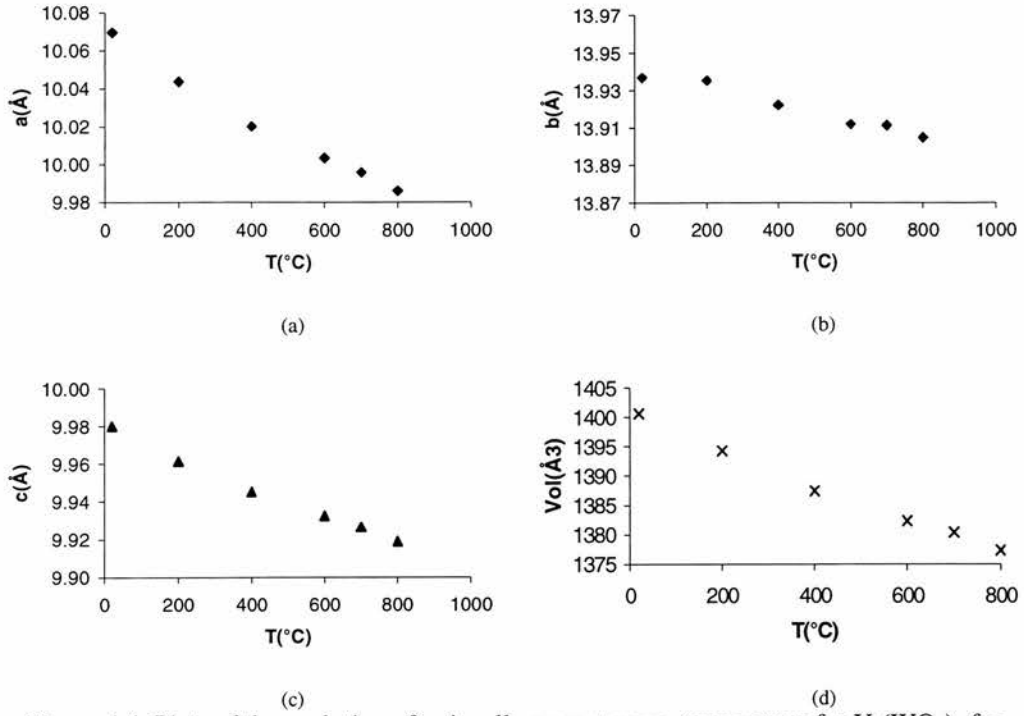


Figure 4.4: Plots of the evolution of unit cell parameters vs. temperature for $Y_2(WO_4)_3$ for (a) the a axis (b) the b axis (c) the c axis and (d) cell volume

$Al_2(WO_4)_3$ shows a slight contraction along both the a and c axes, but the strong expansion of the b axis leads to an overall volume expansion of $4.51 \times 10^{-6} \text{ °C}^{-1}$.

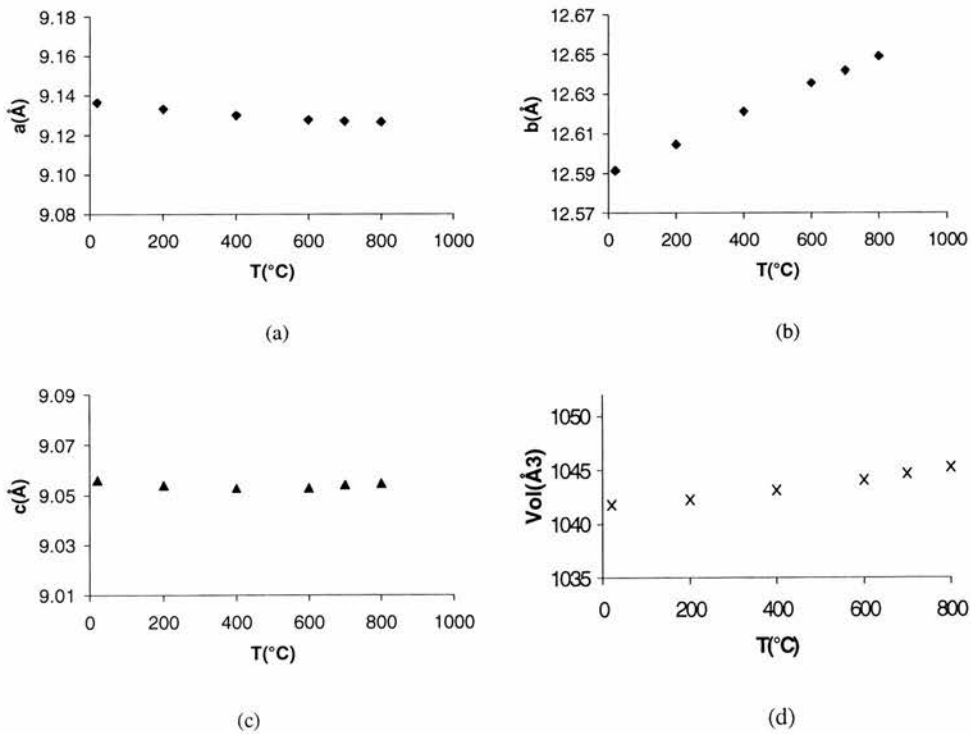


Figure 4.5: Plots of the evolution of unit cell parameters vs. temperature for $Al_2(WO_4)_3$ for (a) the a axis (b) the b axis (c) the c axis and (d) cell volume

As expected $Y_2(WO_4)_3$ shows similar, but slightly enhanced negative thermal expansion to $Lu_2(WO_4)_3$ which both show dramatically different behaviour to $Al_2(WO_4)_3$ and $Sc_2(WO_4)_3$. There is a correlation of the behaviour with ionic size. The larger cation increases the size of the surrounding polyhedra. Oxygen-oxygen repulsive interactions become less significant, allowing a greater distortion of the polyhedra which is necessary for negative thermal expansion in this system⁵. The b axis expansion for $Sc_2(WO_4)_3$ appears to be larger than expected – following these trends it should be lower than the value for $Al_2(WO_4)_3$. This is possibly due to experimental error as the values are relatively close to each other.

Table 4.1 - Coefficients of thermal expansion for $M_2(WO_4)_3$ materials

Sample	Ionic radius for M^{3+} (Å)	α_a ($\times 10^{-6} \text{ } ^\circ\text{C}^{-1}$)	α_b ($\times 10^{-6} \text{ } ^\circ\text{C}^{-1}$)	α_c ($\times 10^{-6} \text{ } ^\circ\text{C}^{-1}$)	V ($\times 10^{-6} \text{ } ^\circ\text{C}^{-1}$)	Ref
$Al_2(WO_4)_3$	0.535	-1.31	5.94	-0.0994	4.51	This work
$Sc_2(WO_4)_3$	0.745	-6.3	7.5	-5.5	-6.5	3
$Lu_2(WO_4)_3$	0.98	-9.9	-2.2	-8.3	-20.4	4
$Y_2(WO_4)_3$	1.01	-10.35	-3.06	-7.62	-20.9	This work

Evans et al³ have carried out an elegant and detailed analysis of the thermal expansion behaviour of $Sc_2(WO_4)_3$. Their modelling of the structure using an isotropic free atom scheme suggested that the WO_4 and ScO_6 polyhedra could be regarded as rigid. They therefore imposed such a constraint on their model, reducing the complexity of the refinement and producing better fits to the diffraction data. They concluded that the root cause of the unusual behaviour was in transverse thermal vibrations of bridging O atoms, manifesting itself in changes in certain Sc-O-W bond angles. A free anisotropic/isotropic model has been used in this case, though this is not suggested as the optimum model. The resulting M-O-W bond angles are presented in tables 4.2 and 4.3 overleaf.

Table 4.2: Y-O-W bridging angles

T (°C)	Y-O1-W2	Y-O2-W1	Y-O3-W2	Y-O4-W1	Y-O5-W2	Y-O6-W2
20	153.8	166.9	156.5	151.3	172.2	149.4
200	156.3	165.1	156.7	152.9	171.2	151.3
400	153.6	165.8	157.6	152.7	170.4	150.8
600	155.9	164.5	159.4	153.3	168.7	150.3
700	151.9	162.5	159.2	155.2	169.8	152.1
800	153.7	161.4	158.2	154.4	170.9	149.4

Errors in these angles are approximately 0.7°

Table 4.3: Al-O-W bridging angles

T (°C)	Al-O1-W2	Al-O2-W1	Al-O3-W2	Al-O4-W1	Al-O5-W2	Al-O6-W2
20	149.8	171.0	154.2	147.1	174.4	141.8
200	150.7	169.3	154.4	148.0	174.4	142.3
400	151.0	167.6	153.6	148.8	174.8	144.3
600	150.4	167.2	153.6	149.4	173.7	145.3
700	150.3	167.3	153.5	150.8	175.2	146.0
800	150.9	165.2	153.1	150.3	175.3	146.3

Errors in these angles are approximately 0.3°

A general trend in Evans' work was that "large" (>170°) angles decrease with temperature, "small" angles (<150°) increase with temperature and "intermediate" angles remain constant.

The angles involving the W1 ion on the special position exhibit the same trends in all the cases of all of $\text{Sc}_2(\text{WO}_4)_3$, $\text{Al}_2(\text{WO}_4)_3$ and $\text{Y}_2(\text{WO}_4)_3$ i.e. M-O2-W1 decreases significantly and M-O4-W1 increases strongly. $\text{Sc}_2(\text{WO}_4)_3$ and $\text{Al}_2(\text{WO}_4)_3$ exhibit the same general thermal expansion properties i.e. that both contract along a and c while b expands although the effects for Sc are more pronounced.

T(K)	Sc-O6-W2
10	142.59
300	144.33
450	145.64

Table 4.4 : Behaviour of the Sc-O6-W2 angle in $\text{Sc}_2(\text{WO}_4)_3$ ³

M-O6-W2 appears to be a key angle, as it remains relatively constant in $\text{Y}_2(\text{WO}_4)_3$ but increases strongly in both $\text{Sc}_2(\text{WO}_4)_3$ (Table 4.4) and $\text{Al}_2(\text{WO}_4)_3$. This may be related to the fact that the 20°C value of this parameter is significantly larger for $\text{Y}_2(\text{WO}_4)_3$ vs. $\text{Sc}_2(\text{WO}_4)_3$ and $\text{Al}_2(\text{WO}_4)_3$. The angles M-O1-W2, M-O3-W2 and M-O5-W2 show little correlation with the different trends in lattice parameters.

4.4: Conclusions

Evans et al.³ suggested that the negative thermal expansivity in the $\text{Sc}_2(\text{WO}_4)_3$ structure was due to transverse vibrations of the 2 co-ordinate bridging oxygen groups, leaving M-O bond lengths unchanged but decreasing the average M-O-W bridging angle, bringing the two cations closer together. They quantified the tilts of individual bonds and related them to the variations in bridging bond angles. Higher resolution data would be required to make these calculations and only general trends involving the M-O-W bridging angles can be looked at. Recently Forster and Sleight⁵ have suggested that $\text{Y}_2(\text{WO}_4)_3$ shows a substantial drop in the W-O distance, leading to a shortening of the Y-W non bonded distance and little change in the Y-O-W angles. The resolution was not sufficient to see clear trends in these distances, although in contrast to Forster's results, this work found both Y-O4-W1 and Y-O2-W1 to vary significantly. These results also suggest that the M-O6-W2 angle shows the greatest difference in thermal behaviour between $\text{Al}_2(\text{WO}_4)_3$, $\text{Sc}_2(\text{WO}_4)_3$ and $\text{Y}_2(\text{WO}_4)_3$. The angle is very small for small M cations (Al – 142°, Sc –143°, Y 150° at 20°C) and expands significantly on heating. This may be one of the most important parameters influencing the differing behaviour of the series.

4.5: References

- 1) V.A. Balashov, G.I. Vorona, A.A. Maier and O.P. Proshina, *Inorg. Mater.*, 1975, **11**, 1469
- 2) J.S.O. Evans, T.A. Mary, and A.W. Sleight, *J. Solid State Chem.*, 1997, **133**, 580
- 3) J. S. O. Evans, T. A. Mary and A. W. Sleight, *J. Solid State Chem.*, 1998, **137**, 148
- 4) P. M. Forster, A. Yokochi and A. W. Sleight, *J. Solid State Chem.*, 1998, **140**, 157
- 5) P. M. Forster and A. W. Sleight, *Int. J. Inorg. Mater.*, 1999, **1**, 123
- 6) T.A. Mary, J.S.O. Evans, T. Vogt, A.W. Sleight, *Science*, 1996, **277**, 90
- 7) J. Rodriguez-Carvajal, *Physica B*, 1993, **55**, 192
- 8) S.C. Abrahams and J. L. Bernstein, *J. Chem. Phys*, 1966, **45**, 8, 2745

4.6: Publications Arising from this Chapter

- 1) D.A. Woodcock, P. Lightfoot, C. Ritter, *J. Solid State Chem.*, in press

Chapter 5: Microporous Materials

5.1: Introduction

Zeolites and AIPO's are widely used in the chemical and petroleum industry as shape selective catalysts and molecular sieves¹. Their properties are associated with their crystal structure, in which vertex linked SiO_4 , AlO_4 and PO_4 tetrahedra form cages and encompass large channels and cavities through which small molecules may diffuse. Commercial catalytic applications thus depend critically on the structure and behaviour of these materials at high temperature.

Computer simulations by Tschaufeser et al² and also by Gale³ have predicted, in advance of experiments, that many zeolites and AIPOs such as those with structure types (as defined by the International Zeolite Association) FAU (zeolite X and Y), MAZ (ZSM-4), RHO (zeolite rho), OFF (offretite), MER (zeolite omega), LTL (zeolite L), VFI (VPI-5), AFT (AIPO-52), ERI (AIPO-17), MWW (MCM-22) and IFR (SSZ-42) will show a negative coefficient of thermal expansion (CTE). Tschaufeser's calculations predict that the expansion will be very much affected by the Si and Al content: the more siliceous zeolites had much greater contraction or expansion. However, the relationship between expansivities and Si/Al ratios is not linear, an effect that is presumably due to the behaviour of extra-framework cations rather than simply the framework composition. Also suggested in Tschaufeser's work is the theory that there is an empirical correlation between 2D and 3D channels and negative thermal expansion (NTE) and that there is a further correlation between low stability, low density and NTE.

Until recently there had been little detailed practical work on the thermal expansion behaviour of framework silicates, apart from the silica minerals and feldspars. α -quartz is known to have a negative thermal expansion below 50K⁴, as is β -quartz above its transition temperature⁵. This behaviour is interpreted as being due to an increase in the amplitude of the anisotropic motion of the oxygen atoms on increasing the temperature, resulting in a further shortening of the Si-O bond distances. Recent lattice dynamic studies on quartz by Smirnov⁶ have identified the presence of Rigid Unit Modes (RUMs, Section 1.9) as being responsible.

Recently Park et al⁷ recorded the coefficient of thermal expansion for MFI (ZSM-5), DOH (dodecasil 1H), DDR (decadodecasil 3R), MTN (dodecasil 3C) and AFI (AIPO-5). They found a volume expansion between 298K and 345-534K, followed by a contraction for each over a limited temperature range. Na-zeolite X has been found to contract by Couves et al⁸, as has Zeolite A by Colantuano⁹, but this is believed to be due to a partial structure collapse.

Siliceous faujasite¹⁰ and AIPO-17¹¹ have both been identified by Sleight and Attfield as contracting, AIPO-17 exceptionally so with a linear CTE of $-11.7 \times 10^{-6} \text{K}^{-1}$ (corresponding to $\alpha_v = -35.1 \times 10^{-6} \text{K}^{-1}$ over a temperature range of 18-300K. This value is significantly more negative than previously reported for any material and also significantly greater than the value predicted in computer simulations. In neither of these studies were any noticeable changes found in the internal geometry of the structure, including O-T-O and T-O-T angles.

The overall mechanism of negative thermal expansion in zeolites remains unclear. Studies by Dove¹² have outlined a Rigid Unit Mode theory of negative thermal expansion which states that the existence of low energy distortions can be predicted depending on the connectivities of the tetrahedra. Contraction of the material is dependent on the flexibility of the T-O-T bridging angle which is in turn dependent on these low energy distortions. It has also been suggested by Sleight¹¹ that an empirical way of predicting which zeolites and aluminophosphates contract is to compare the cell volumes of the as prepared and calcined dehydrated materials. If the as prepared volume is lower than the calcined volume, then the framework has contracted around the Structure Directing Agent, and therefore has the ability to contract and may exhibit negative thermal expansion.

5.2: Experimental

Several materials were selected for study. Pure zeolitic SiO₂ polymorphs were preferred so that the results were not influenced by either extraframework cations or water content, although some dehydrated aluminophosphates were also studied. For most of these materials, measurements were carried out over a

temperature range which was both wider than Sleight's and encompassing catalytically useful temperatures.

The following materials were studied: ITQ-1* (Instituto de Tecnología Química, Valencia), ITQ-3*, ITQ-4, ITQ-7, ITQ-9, SSZ-23*, CIT-5, AIPO-31*, MAPO-17 and chabazite. All samples were pure SiO₂ polymorphs except for AIPO-31 and MAPO-17. Those samples marked * were studied by X-ray diffraction only. This was because for neutron powder diffraction studies larger quantities of samples were required and due to a combination of this, high structural complexity, presence of structural intergrowths and limited neutron time it was not feasible to study all samples using both techniques.

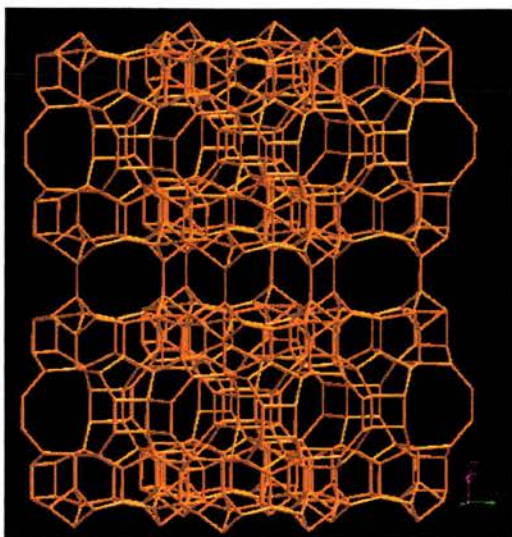
5.3: X-ray Diffraction Study

All samples were synthesised as described previously for ITQ-1¹³, ITQ-3¹⁴ SSZ-23¹⁵ and AIPO-31¹⁶. ITQ-1, ITQ-3 and SSZ-23 were synthesised by Dr Luis Villaescusa and Dr Maria-Jose Diaz-Cabanias at the Instituto de Tecnología Química, Valencia. Samples were calcined in a dry, flowing O₂ atmosphere at 550°C for 8h and placed into a 0.5mm quartz capillary within a few minutes. Thermogravimetric analysis was performed on each of the samples in order to ascertain whether water loss was responsible for any of the thermal contraction. This showed that a maximum of 0.2% water was adsorbed on these hydrophobic materials. Furthermore, the materials chosen for the study possess essentially no connectivity defects, so any observed thermal contraction could not be caused by annealing of the defects. The absence of Si-OH groups is demonstrated by ²⁹Si MAS NMR of the calcined materials as shown by Cambor et al for each siliceous material.

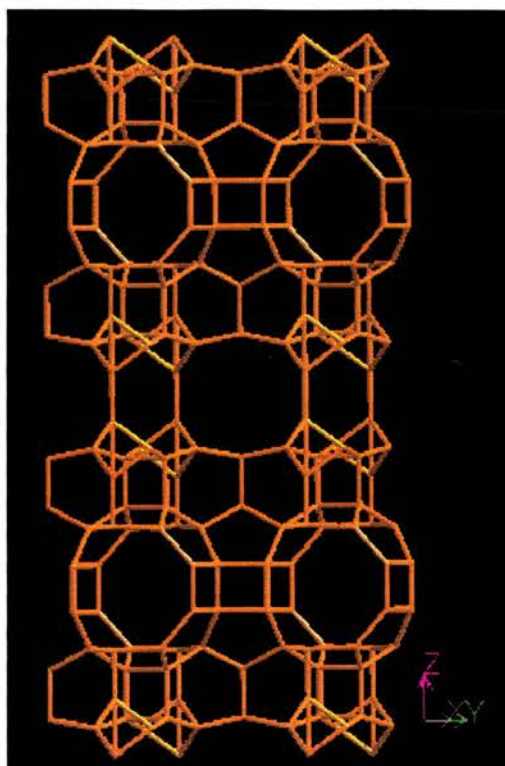
X-ray patterns were recorded at 50°C intervals up to 500°C for SSZ-23, ITQ-1 and AIPO-31 and to 550°C for ITQ-3 on a STOE Stadi-P transmission diffractometer using Cu K_{α1} radiation at 1.54056Å, over a 2θ range of 7.7 - 45.2°. The resultant histograms were processed using the GSAS program¹⁷, using literature values for atomic co-ordinates, and refining scale factor, lattice parameters, zero point, background and peak shapes only.

5.3.1: Structure Descriptions

ITQ-1 (MWW) is a pure silica zeolite crystallising in the hexagonal space group $P6/mmm$ with two ten membered ring (MR) channels. Large cages are formed from side pockets in the channel system. ITQ-1 is the pure silica analogue of MCM-22 and consists of two double layers joined by single Si-O-Si bridges. The framework is depicted in figure 5.1, with a clearer view of the layers in a projection along the (100) plane shown in figure 5.2.



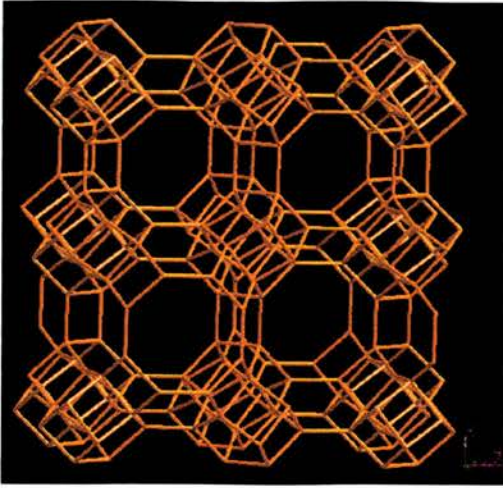
Above: Figure 5.1* : Framework projection of ITQ-1



Right: Figure 5.2*: Projection of ITQ-1 along (100) plane.

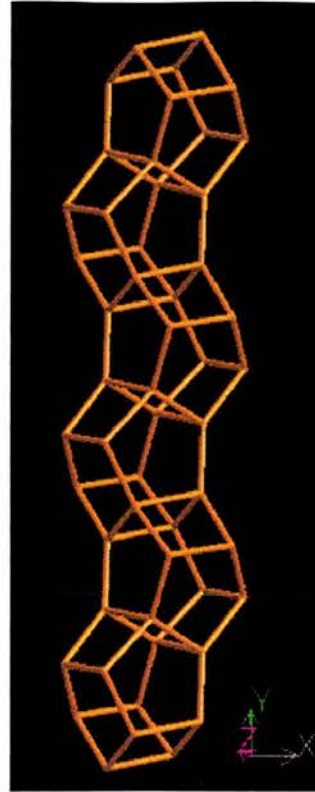
ITQ-3 is a pure silica zeolite crystallising in orthorhombic space group $Cmcm$. It consists of a 2D system of 8MR channels and is closely related to zeolite RUB-13. Intergrowths between the two structure types occur readily, rendering a detailed structural study problematic.

*Figures 5.1-5.6, 5.19, 5.20 and 5.23-5.28 reproduced from the International Zeolite Association Structure Commission website.



Above : Figure 5.3: Projection of the framework structure of ITQ-3

Right: Figure 5.4: The chains of cages arranged along b in ITQ-3



SSZ-23 is monoclinic, crystallising in space group $P 2_1/n$ and was the first pure silica zeolite to be identified with a 9 MR system. The structure is very complex, with 16T atoms.

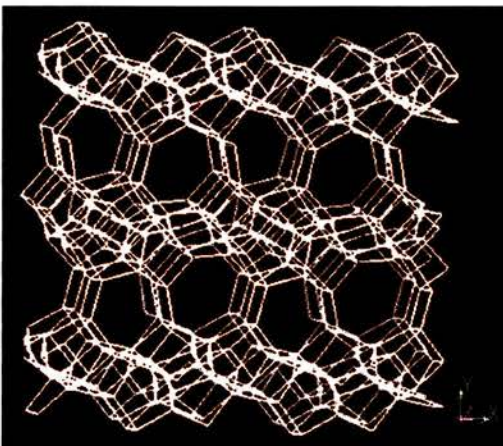


Figure 5.5: Framework of SSZ-23

AIPO-31 is rhombohedral in space group $R-3$. Structural features include non-planar layers of $4^2.6^2.12$ -rings linked with staggered four-rings. The pore structure consists of 12-membered rings forming unidimensional channels.

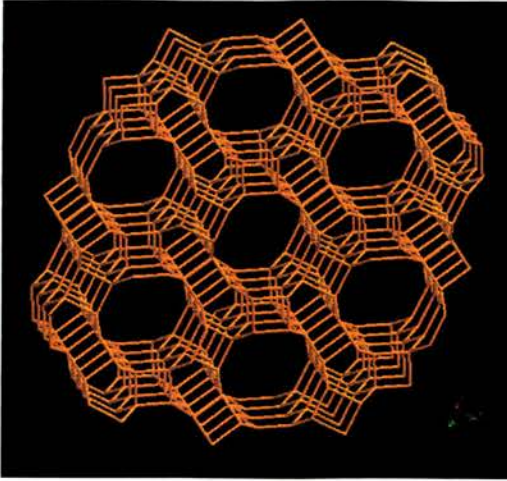


Figure 5.6: Framework view of AIPO-31 showing unidimensional channels formed from 12 membered rings.

5.3.2: Results and Discussion

The values of α found are detailed in Table 1 and shown in figures 5.7-5.10.

Table 5.1: Comparison of CTE's Determined by Powder XRD

All α values are $\times 10^{-6} \text{ K}^{-1}$

Sample	α_a	α_b	α_c	α_{vol}	Range (K)	Ref
ITQ-1	-4.23	-4.23	-3.21	-12.1	323-773	This work
ITQ-3	-0.29	-2.06	-10.1	-11.4	323-823	This work
SSZ-23	-6.09	-3.21	-0.73	-10.3	323-773	This work
AIPO-31	+9.72	+9.72	+17.3	+32.8	373-773	This work
MFT	-5.5	-6.9	-2.8	-15.1	393-975	7
AFI	-5.1	-5.1	-3.7	-14.5	424-774	7
DOH	-0.6	-0.6	-3.1	-3.1	573-996	7
MTN	-1.7	-1.7	-1.7	-5.0	463-1002	7
DDR	-2.8	-2.8	-3.1	-8.7	492-1185	7
Faujasite	-4.2*	-4.2*	-4.2*	-12.6*	25-573	10
AIPO-17	-11.7*	-11.7*	-11.7*	-35.1*	18-300	11

* These values are calculated from the values quoted for linear α 's which are equal to $\alpha_v/3$.

All three of the pure SiO_2 materials show a large negative α comparable to that of faujasite over this range though none as large as that found by Sleight for AIPO-17. AIPO-31 expands very strongly, which is consistent with

Tschaufeser's predictions for materials with only 1D channels. Note that the negative thermal expansion found for MFT, AFI, DOH, MTN and DDR only occurs over a limited temperature range, and that faujasite and AIPO-17 have been studied under cryostatic conditions. In order to compare the materials directly it would be necessary to study them over the same temperature range. Our experiments undertaken on AIPO-17 over the range 50-500°C showed a small contraction of a and a large expansion of c leading to an overall volume expansion.

Also worthy of note is the behaviour of ITQ-1 which features linear Si-O-Si bonds, a common characteristic of negative thermal expansion materials. It is the pure silica analogue of MCM-22, which was predicted to contract by Gale³.

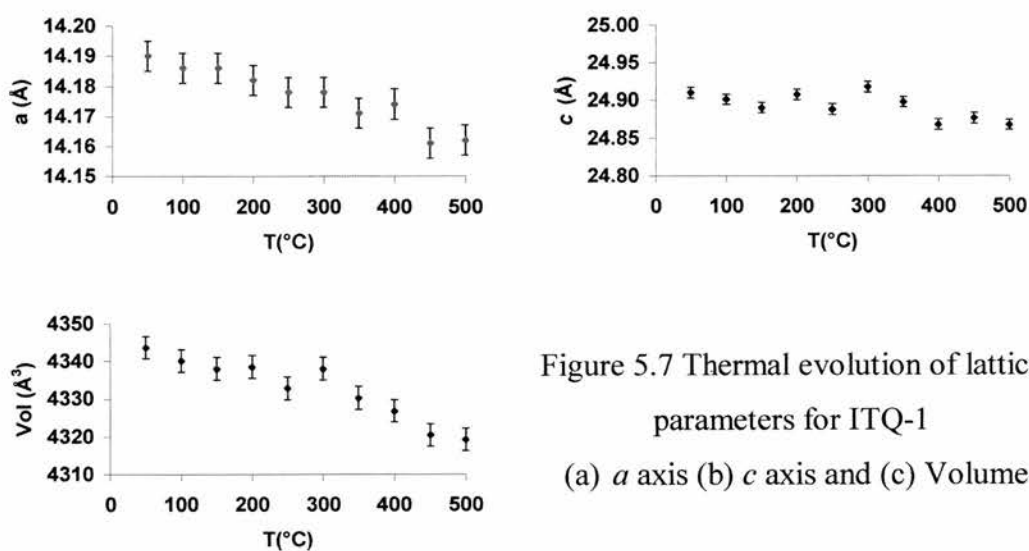


Figure 5.7 Thermal evolution of lattice parameters for ITQ-1
(a) a axis (b) c axis and (c) Volume

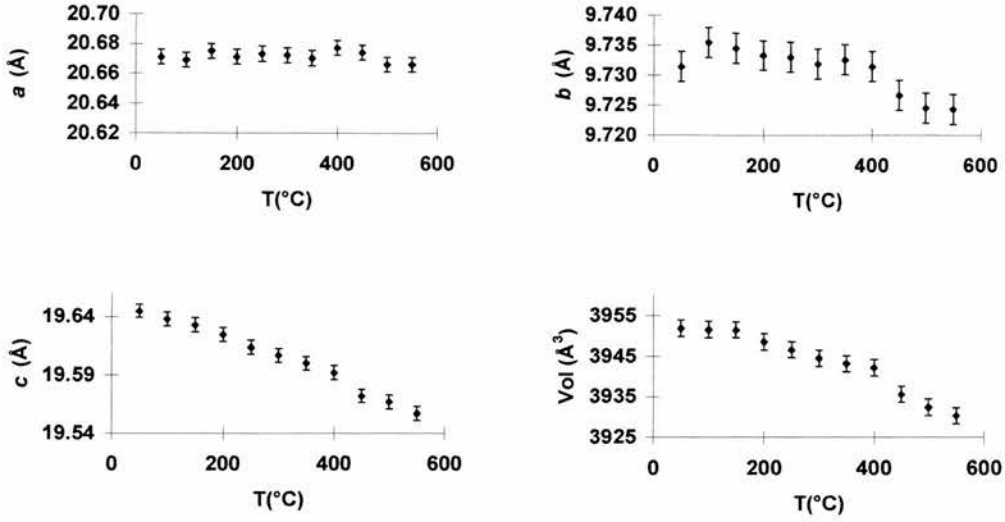


Figure 5.8 Thermal evolution of lattice parameters for ITQ-3 (a) *a* axis (b) *b* axis (c) *c* axis and (d) Volume

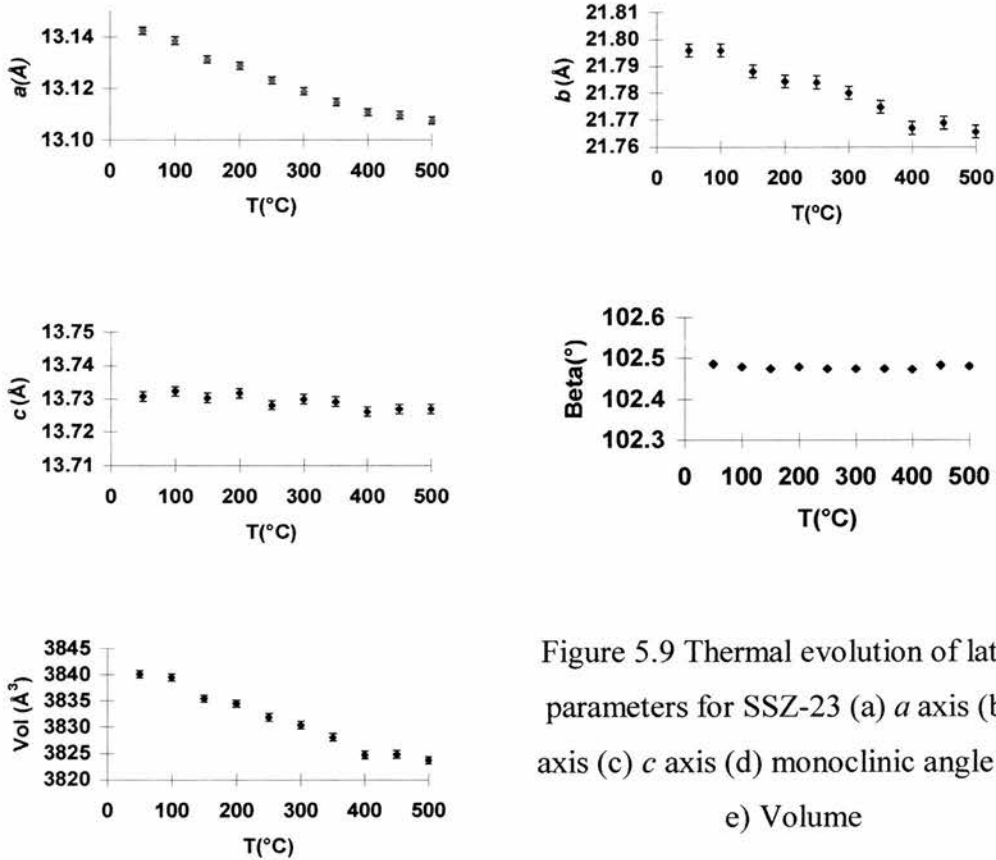


Figure 5.9 Thermal evolution of lattice parameters for SSZ-23 (a) *a* axis (b) *b* axis (c) *c* axis (d) monoclinic angle and (e) Volume

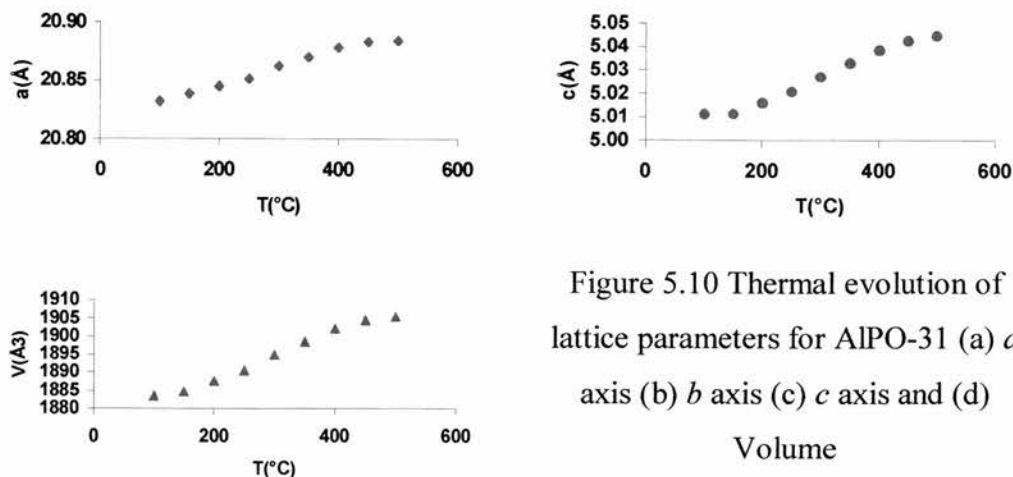


Figure 5.10 Thermal evolution of lattice parameters for AlPO-31 (a) a axis (b) b axis (c) c axis and (d)

Volume

5.3.3: Conclusions (from X-ray Diffraction)

The aim of this work was to measure the variation of lattice parameters by powder X-ray diffraction. This technique is precise enough to show trends in the evolution of lattice parameters. However, structure determination from powder neutron or single crystal X-ray diffraction data would be required to study the mechanism more closely. For example, the current data show highly anisotropic contraction, especially for ITQ-3 and SSZ-23, which at first sight does not correlate significantly with structural features such as the chains of cages arranged along b in ITQ-3, the layers in the ab plane in ITQ-1 or with the puckered layers parallel to (101) in SSZ-23. Interestingly MCM-22, analogous to ITQ-1 has been predicted to contract by Gale³. However, the predicted CTEs of $\alpha_a = -2 \times 10^{-6}\text{K}^{-1}$ and $\alpha_c = -9 \times 10^{-6}\text{K}^{-1}$ do not correlate with these results.

It is important also that studies incorporate high temperatures as well as low, since the behaviour does not appear to be continuous. It is possible that the trends found at low temperature are much more dramatic.

Further detailed structure analysis would be required in order to pinpoint specific structural and compositional features which may influence this unusual behaviour. However, these particular samples were not chosen for PND due to the issues mentioned in section 5.2. Experiments on the other samples are detailed in the next section.

5.4: Neutron Diffraction

The technique of neutron diffraction has the potential to allow a much more detailed examination of both structure and mechanism. One of the most significant points to arise from both the experimental and computational work is the suggestion that in all the framework structures where NTE has been reported, the thermal behaviour may be described in terms of dynamic rocking of essentially rigid polyhedra. This approximation has been borne out in powder diffraction studies of the system $\text{Sc}_2(\text{WO}_4)_3$ ¹⁸ and the only two zeolitic systems so far analysed quantitatively – SiO_2 (faujasite)¹⁰ and AIPO-17¹¹. Within both faujasite and AIPO-17 the mechanism of contraction is believed to be due to the transverse vibrations to the two co-ordinate bridging oxygens.

Previous studies on members of the $\text{NaZr}_2(\text{PO}_4)_3$ (NZP) family (Chapter 3) suggest that it may be relevant in some cases to consider a certain degree of flexibility of the polyhedra. In this study, the mechanism of negative thermal expansion in pure SiO_2 zeolites is investigated, and results presented of powder neutron diffraction data analysis on two polymorphs, chabazite (CHA) and ITQ-4 (IFR). In the case of chabazite, three different Rietveld refinement strategies are described and compared, viz. free isotropic refinement, geometrically restrained refinement and isotropic rigid body refinement. This type of analysis should in principle help discriminate between dynamic and static effects. Neither of the two previously studied systems, faujasite and AIPO-17 showed a systematic change in atomic co-ordinates with temperature, implying that harmonic transverse vibrations of the bridging oxygen atoms were responsible for the thermal contraction, rather than genuine static change in Si-O-Si or O-Si-O bond angles. One of the main characteristics of the thermal contraction in $\text{Sc}_2(\text{WO}_4)_3$ ¹⁸ and ZrW_2O_8 ¹⁹, however, is a change in bridging angles (M-O-M'). The structure of chabazite is similar to that of AIPO-17 in that both are composed of systematic stacking of double six rings as shown in figure 5.11.

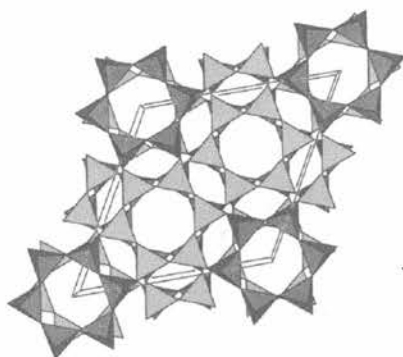


Figure 5.11 – Polyhedral representation of the structure of chabazite viewed down the c axis.

Within chabazite the rings are stacked in the sequence AABBC, whereas in AIPO-17 they are stacked AABAAC (ERI structure type). This results in similar hexagonal lattice parameters for the two structures, similar framework densities and both having 6 and 8 membered ring channels.

IFR materials (termed as ITQ-4 or SSZ-42²⁰) have been modelled by Gale³. His results predict negative thermal expansion along all cell axes and an increase in the monoclinic angle, leading to an overall volume contraction.

5.4.1 Experimental

Pure silica samples of chabazite and ITQ-4 were prepared by Cambor et al by the methods outlined in the literature^{21,22}. Each sample was initially studied by variable temperature X-ray powder diffraction on a STOE STADI-P diffractometer. Data quality was sufficient to quantify the behaviour of unit cell parameters vs. temperature. Both had a reduction in cell volume over the temperature range 323K to 773K.

The sample of chabazite was placed in a vanadium can and run in furnace RALF3 on the OSIRIS instrument²³ at the ISIS facility at the CCLRC Rutherford Appleton Laboratory. The choppers were run at 25Hz giving, with the current opening angles, a bandwidth of 4Å for each setting. To have overlap between the different measurements 6 different settings were used to cover the range 2Å to 16Å. This gives in the near backscattering geometry of OSIRIS a d-spacing range of about 1.0 to 7.0Å. Measurements were recorded at 293K, 473K, 673K, 773K, 873K and 1073K. A measurement of an empty can was recorded and subtracted from the initial data before starting refinements. The first of the

chabazite refinements to be carried out using the GSAS program¹⁷ was completely unrestrained, refining unit cell parameters, scale factor, background, peak shape (Gaussian double exponential), atomic co-ordinates and isotropic temperature factors, which were constrained by atom type. Each refinement consisted of refinements of 28 variables, 274 reflections over the range 1.0 to 7.0 Å. The experiment was repeated firstly using soft constraints for Si-O (1.61 +/- 0.005) and O-O (2.58 +/- 0.005) distances and secondly by treating the SiO₄ tetrahedra as rigid bodies, with Si-O fixed at 1.61Å, and isotropic thermal parameters for Si and O.

The sample of ITQ-4 was run in the cryofurnace at temperatures 95K, 142K, 225K, 342K, 442K and 510K. Choppers were set as for chabazite giving the same d-spacing range of 1.0 to 7.0 Å. As above, the background was subtracted and a free isotropic refinement performed. Due to the increased complexity of this structure it is felt that a full quantitative discussion is not appropriate.

5.4.2: Results and Discussion

Chabazite R_{wp} , R_p and χ^2 values for unrestrained, restrained and rigid body refinements are shown in appendix 3, table A3.1. The Rietveld fit at 293K is shown in figure 5.12.

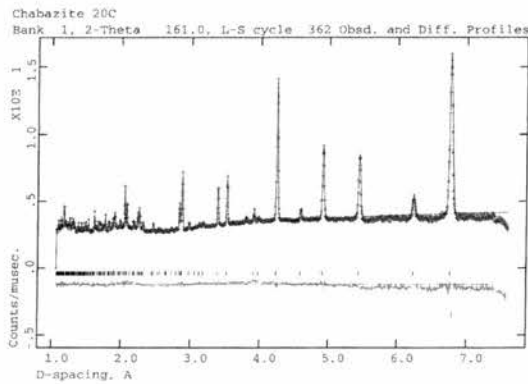


Figure 5.12 – Typical neutron Rietveld plot for Chabazite at 293K

From these results, the free refinement strategy appears to give the best results. Due to limited data, a full TLS rigid body refinement cannot be carried out so the suggestions of Evans and Sleight¹⁸ cannot be tested.

The unit cell parameters and atomic co-ordinates at the highest and lowest temperatures are shown in table A3.2. Plots of the behaviour of unit cell parameters and volume are shown in figures 5.13.

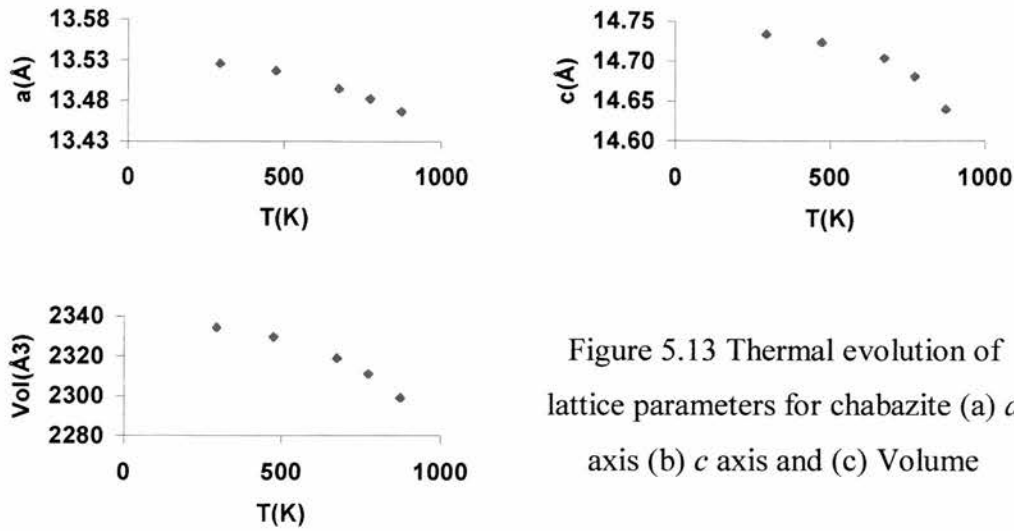


Figure 5.13 Thermal evolution of lattice parameters for chabazite (a) a axis (b) c axis and (c) Volume

As can be seen the behaviour of all parameters is non linear. Polynomial coefficients of thermal expansion were therefore calculated using equation 1.2 as described in section 1. The resulting values are tabulated in table A3.3 and α 's shown in table 5.2 below.

Table 5.2: Experimentally determined CTE's for chabazite

T	a	c	Vol.	Average axial
293K	-2.4E-06	-3.7E-06	-1.6E-05	-0.5E-06
473K	-5.6E-06	-5.0E-06	-1.7E-04	-5.3E-06
673K	-9.2E-06	-1.5E-05	-3.3E-04	-11.0E-06
773K	-1.1E-05	-1.9E-05	-4.1E-04	-13.7E-06
873K	-1.3E-05	-2.4E-05	-5.0E-04	-16.7E-06

The chabazite results from $T=1073\text{K}$ have not been considered in this calculation as the fit was starting to deteriorate due to a splitting of some reflections suggesting a decomposition or a transformation to lower symmetry.

Considering the structural parameters, the Si-O-Si and O-Si-O angles are the parameters which show the greatest change. The most significant of these are plotted in figure 5.14.

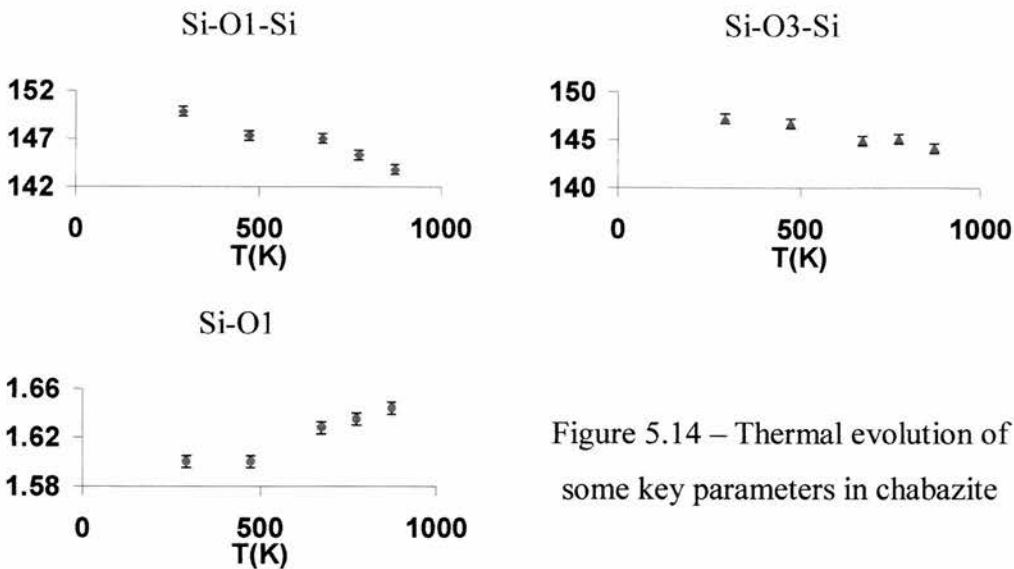


Figure 5.14 – Thermal evolution of some key parameters in chabazite

There is a strong contraction in the Si-O1-Si angle and in the Si-O3-Si angle. This, coupled with the expansion in the Si-O1 bond length which forms part of the same single 6 ring configuration suggests a narrowing of the channels as the Si's move closer together. A representation of this single 6 ring viewed down the c axis is shown in figure 5.15.

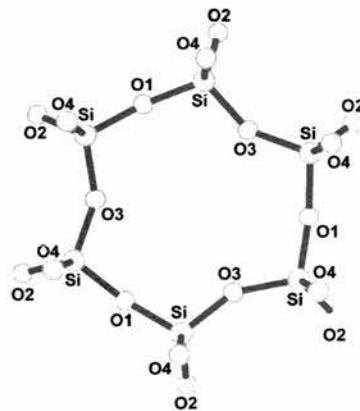


Figure 5.15 – Representation of the single 6 ring in chabazite viewed down the c axis

The contraction of the ring is clearly responsible for the contraction of the a and b axes.

There is an expansion of the O3-Si-O4 angle and a contraction of the O1-Si-O2 angle which form opposite sides of the same tetrahedron. It is perhaps this distortion in particular which is responsible for the failure of the rigid body model in this case as the tetrahedra can no longer be treated as rigid.

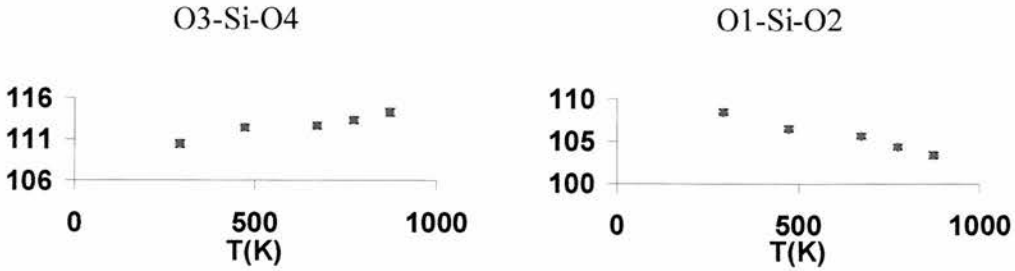


Figure 5.16 – Thermal evolution of the key O-Si-O bridging angles in chabazite

The double 6 ring structure viewed perpendicular to the c axis is shown in figure 5.17 below.

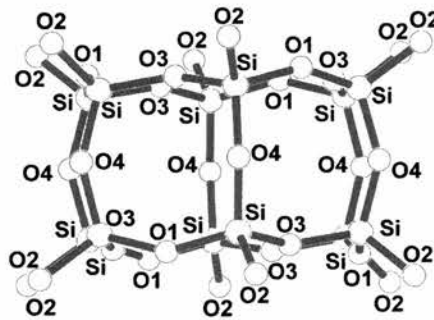
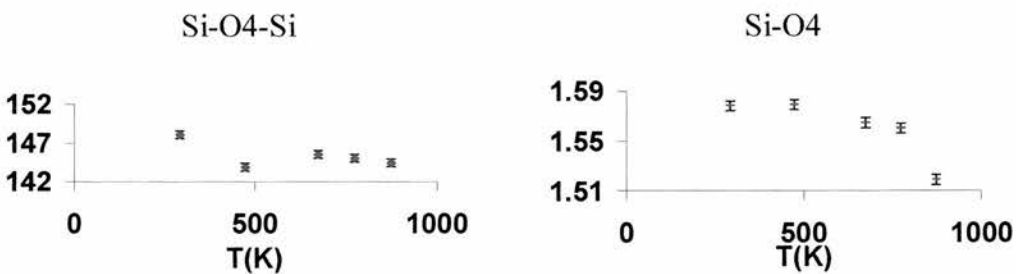


Fig 5.17 - Representation of the double 6 ring in chabazite viewed perpendicular to the c axis

The bridging Si-O4-Si angle can be clearly seen. There is a small decrease in this angle, and an apparent shortening of the Si-O4 distance.



This may be an artefact of the isotropic refinement strategy and may really reflect increased transverse motion of O4. However the combined effect is to pull the

layers closer together, as revealed in the corresponding Si-Si distance (figure 5.18) and shorten the *c* axis.

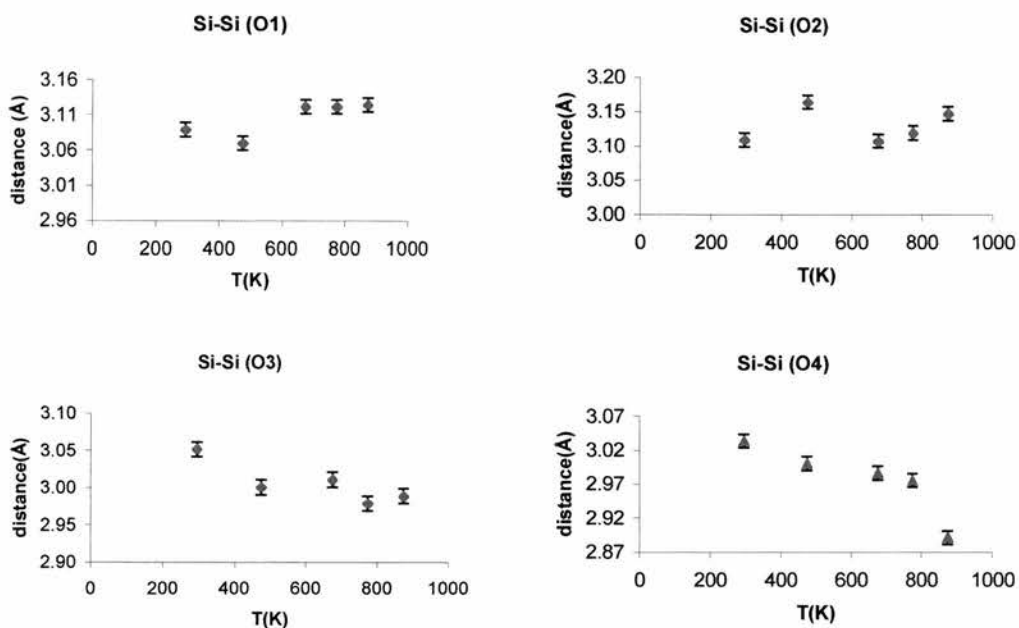
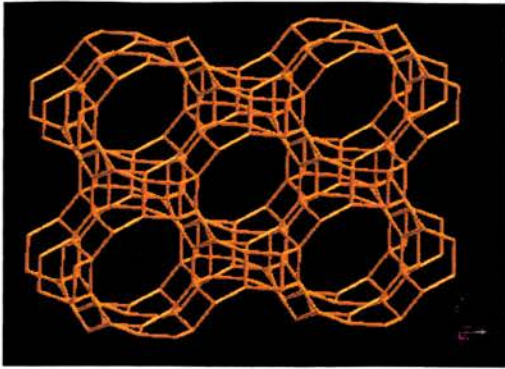


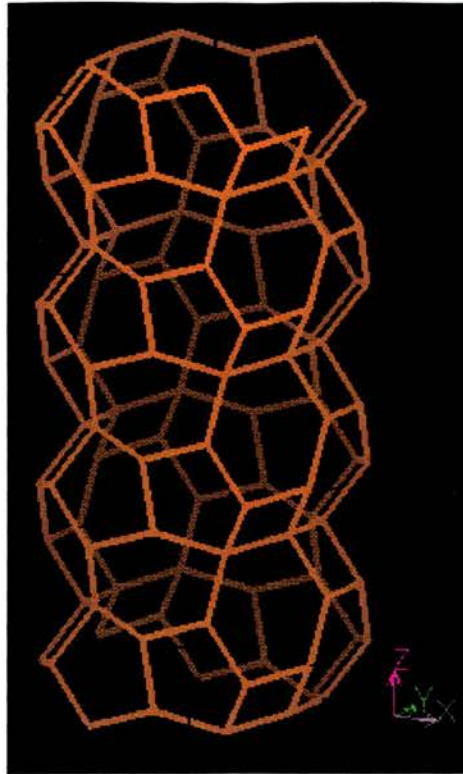
Fig 5.18: Si-Si distances. It is the Si-Si (O4) distance which contracts most strongly and is the one which relates to the contraction between the layers.

ITQ-4 has a large one dimensional large-pore sinusoidal channel running along the *c* axis. The channel is formed from a large pore 12 MR which is highly puckered. Each channel is separated from each other by a single chain of alternating 4MR and 6MR, leading to a very high density of channels and hence a large void space. The framework is shown overleaf in figure 5.19 and a view of the channel in figure 5.20.



Above: Figure 5.19 : framework view of ITQ-4

Right: Figure 5.20: View of the 12MR channel in ITQ-4



The Rietveld fit for ITQ-4 at 95K is shown in figure 5.21 and corresponding structural parameters are given in table A3.4 in Appendix 3.

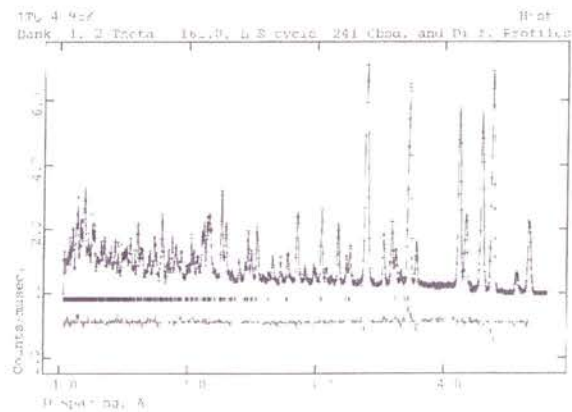


Figure 5.21 - Typical neutron Rietveld plot for ITQ-4 at 95K.

The behaviour of the unit cell parameters is shown in figure 5.22 and their polynomial fits are given in table 5.3.

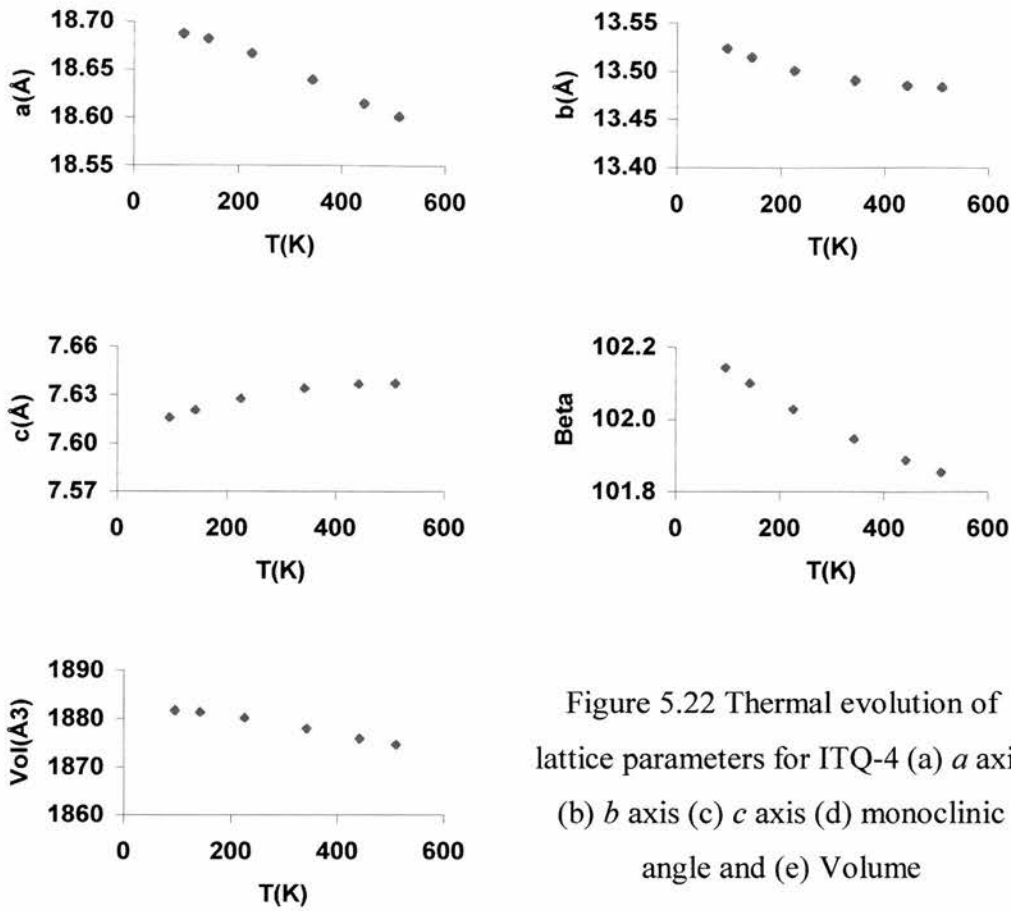


Figure 5.22 Thermal evolution of lattice parameters for ITQ-4 (a) a axis (b) b axis (c) c axis (d) monoclinic angle and (e) Volume

In the case of ITQ-4, the data is not of high enough quality to identify the key trends influencing the behaviour.

Table 5.3: Experimentally determined CTE's for ITQ-4

T	a	b	c	Volume	Average axial
95	-11.5E-06	-1.5E-05	1.40E-05	-6.5E-06	-2.2E-06
142	-11.5E-06	-1.3E-05	1.24E-05	-7.1E-06	-2.4E-06
225	-11.5E-06	-1.0E-05	9.52E-06	-8.2E-06	-2.7E-06
342	-11.5E-06	-5.6E-06	5.49E-06	-9.8E-06	-3.3E-06
442	-11.5E-06	-1.9E-06	2.05E-06	-1.1E-05	-3.7E-06
510	-11.5E-06	6.6E-07	-3.00E-07	-1.2E-05	-4.0E-06

However, in contrast to previous simulations of ITQ-4 (SSZ-42)³, an expansion of the c axis and a contraction of the monoclinic angle have been found. This is an expansion along the channels within ITQ-4.

Table 5.4: Comparison of CTE's for SSZ-42 and ITQ-4

	This work ($\times 10^{-6}\text{K}^{-1}$)	Gale ($\times 10^{-6}\text{K}^{-1}$)
α_a (95K)	-11.5	-8.5
α_a (510K)	-11.5	-9
α_b (95K)	-15	-2.5
α_b (510K)	+0.66*	-4.5
α_c (95K)	+14	-5
α_c (510K)	-0.3*	-5
α_β (95K)	-9.3	+3.5
α_β (510K)	-4.3	+8

*change sign at approx. 480K

The hypothesis relating an expansion of the unit cell volume on calcination to negative thermal expansion is inconclusive in the case of ITQ-4, which expands by only 0.06% upon calcination, and is not borne out at all in the case of chabazite which contracts by 0.18% on calcination. A given zeolite may be prepared with different structure directing agents in such a way that removal of the template may cause expansion or contraction of the cell depending on the template. The thermal behaviour of the calcined material would be expected to be essentially independent of the template used.

5.4.3: Conclusions (Neutron Diffraction Experiments Part One)

Of the three models tested, the free isotropic refinement strategy was found to be most suitable in the case of chabazite although the data were not of sufficient quality to give an unambiguous thermal motion model. Both ITQ-4 and chabazite contract, chabazite exceptionally so with its contraction exceeding that of even AlPO-17, the most strongly contracting material known as the temperature approaches 873K ($\alpha_{\sqrt{3}} = -16.7$ c.f. $-11.7 \times 10^{-6}\text{K}^{-1}$). Within this system the key feature appears to be the behaviour of the Si-O1-Si and Si-O3-Si angles, which contract, pulling the single 6 rings together and contracting the a and b axes. The c axis contracts due to a shortening of the Si-O4-Si bond pathway which bridges the double 6 rings. Whether these effects are static or merely due to transverse vibration of bridging O atoms is still an ambiguity. Higher resolution powder

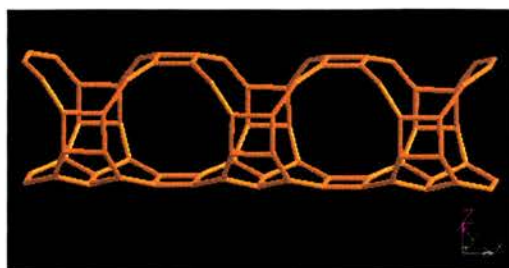
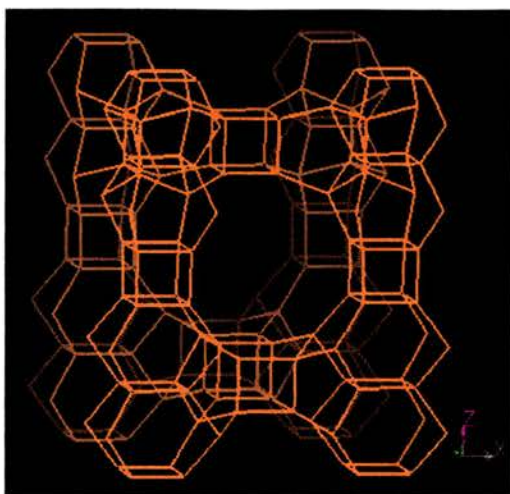
data, or preferably single crystal, will be required in order that a more satisfactory model of thermal motion effects can be obtained.

The relative strength of the contraction of the c axis in chabazite compared to that of its a and b axes is the inverse of that in AIPO-17 which showed a stronger contraction in its a and b rather than c axes, despite the fact that the two structures are closely related.

The results from ITQ-4 do not show adequate precision to draw definite conclusions of the key parameters influencing its thermal contraction. A further study extended to lower d spacings is required. However the cell parameters, which are well defined from these data, are in contrast to Gale's calculations³. He predicted a contraction of all three axes and an expansion of the monoclinic angle compared to our results which show a contraction of the a and b axes and the monoclinic angle and an expansion of the c axis, along the direction of the 12MR channels. Clearly further work, both experimental and computational, is merited on these, and other related microporous systems, before a fuller explanation of their behaviour can be established.

5.5: Further Neutron Diffraction Experiments

Further neutron experiments on three more silica polymorphs ITQ-7, ITQ-9 and CIT-5 and a magnesiumaluminophosphate MAPO-17. ITQ-7²⁴ is related to zeolite Beta, crystallising in the tetragonal space group $P4_2/mmc$. It is a three dimensional system with large pore 12MR channels (MR= membered ring) and double 4MR channels. It has a very large micropore volume and low framework density, ranking alongside chabazite as the lowest with 15.4 Si per 1000Å³.



Left: Figure 5.23 : View of ITQ-7 normal to (001)

Above: Figure 5.24: The channel system in ITQ-7

ITQ-9²⁵ is triclinic in space group I-1 and consists of 1D cages joined through 10MR windows. It has an extremely large pore volume (0.21cm³/g) compared to other 1D/10MR zeolites.

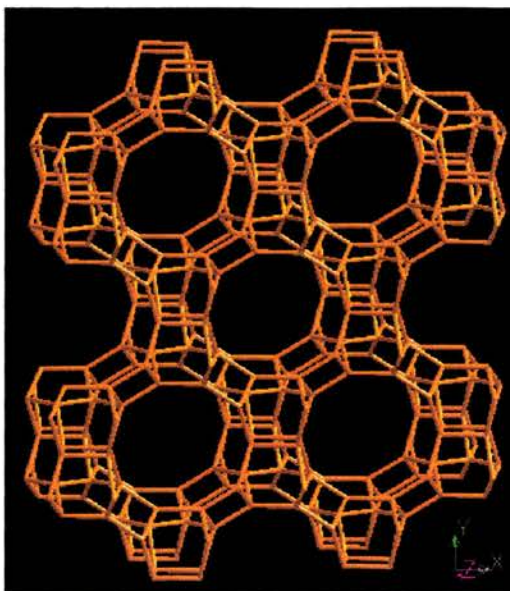
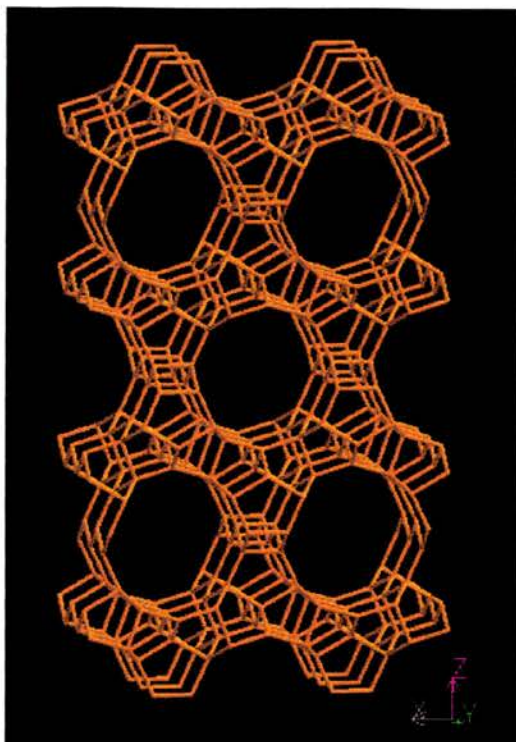


Figure 5.25: Framework structure of ITQ-9

CIT-5²⁶ is one of the first extra-large pore zeolites with 14MR channels. These channels run parallel to the b axis and are surrounded by a number of small cage units. Figure 5.26 shows the framework structure and figure 5.27 the channel system. It is orthorhombic in space group Im2a.



Above: Figure 5.26: The framework structure of CIT-5

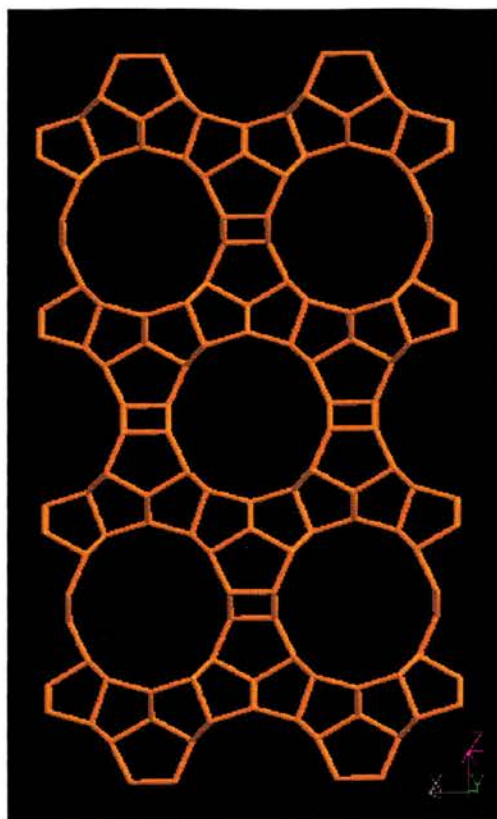


Figure 5.27: The channel system in CIT-5

MAPO-17 is similar to ALPO-17 (ERI, erionite structure) but with a 10% doping of Mg into the framework for ease of synthesis. The charge is balanced by the presence of H^+ groups attached to the bridging oxygens. It crystallises in the hexagonal space group $P 6_3/m$ and a view of the structure is shown in figure 5.28 below.

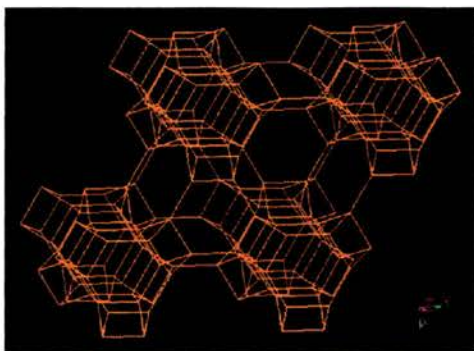


Figure 5.28: View of the structure of MAPO-17

5.5.1: Experimental

The pure silica zeolites ITQ-7²⁴, ITQ-9²⁵ and CIT-5²⁶ were prepared by members of the Cambior group according to the literature. MAPO-17 was prepared by Martin Maple from a diquinuclidinium template of formula $[(C_7H_{13}N)(CH_2)_3(C_7H_{13}N)](OH)_2$ as described previously²⁷.

Data were collected for ITQ-7, ITQ-9 and MAPO-17 on the OSIRIS instrument²³ at the ISIS facility at the CCLRC Rutherford Appleton Laboratory. Samples were placed in a vanadium can and run in furnace RALF3 at the same settings as described in section 5.4.1. Measurements were recorded at 30°C and in 100° steps from 100°C to 700°C for CIT-5, at 50°C and from 100°C to 500°C in 100°C steps for MAPO-17 and at 60°C, 120°C, and from 200°C to 600°C in 100°C steps for ITQ-7. Problems with the monitor at 300°C for ITQ-7 led to this measurement being discarded. A measurement of an empty can was recorded and subtracted from the initial data before starting refinements.

Refinements were carried out using the GSAS program¹⁷. For both CIT-5 and ITQ-7 unit cell parameters, scale factor, background, peak shape (Gaussian double exponential), atomic co-ordinates and isotropic temperature factors, which were constrained by atom type, were refined. Refinements of CIT-5 data consisted of refinements of 57 variables, 4757 reflections over the range 1.0 to 7.0 Å and for ITQ-7 data, 59 variables and 1860 reflections over the same d-spacing range. Soft constraints for Si-O (1.61 +/- 0.005) and O-O (2.58 +/- 0.005) distances were used.

MAPO-17 refinements were of scale factor, background and unit cell parameters only, using 7 variables, 4373 reflections over the range 1.0 to 7.0 Å.

Data were collected for ITQ-9 in a vanadium can on the POLARIS instrument at 20°C, and from 200°C to 600°C in 100°C steps. A background measurement was subtracted. The same refinement strategy was used as in the CIT-5 and ITQ-7 experiments, although data from the low angle, 90° and backscattering banks were combined for greater precision. This resulted in an overall d-spacing range of 0.7 to 8.3 Å and refinements using 104 variables and 6135 reflections.

5.5.2: Results and Discussion

Unit cell parameters vs T are plotted in figures 5.29-5.33 on a scale relative to the change in chabazite. CTE's were calculated according to equation 1.2 and are shown in Table 5.5. Atomic co-ordinates at highest and lowest temperatures along with R-factors can be found in Appendix 3. All of the plots shown below are on a scale relative to that of both chabazite and CIT-5.

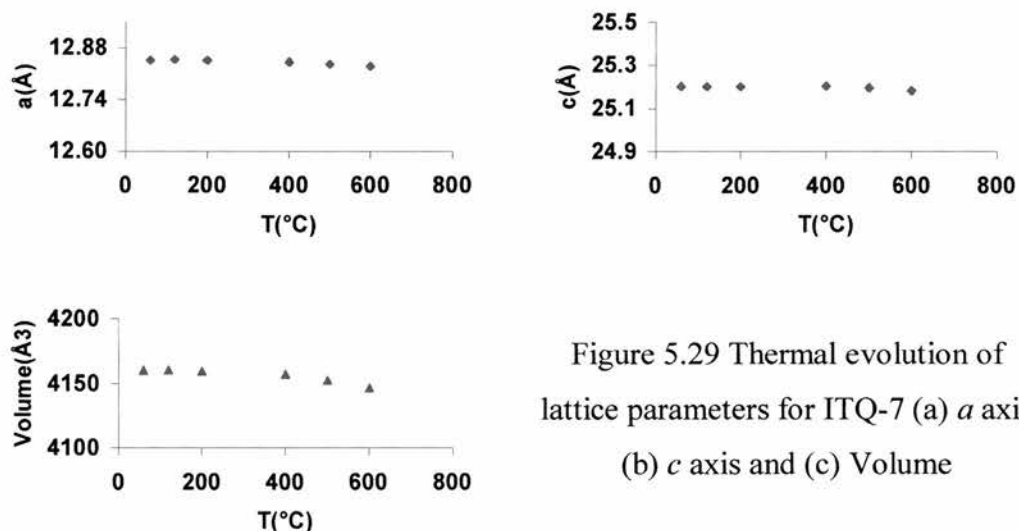


Figure 5.29 Thermal evolution of lattice parameters for ITQ-7 (a) a axis (b) c axis and (c) Volume

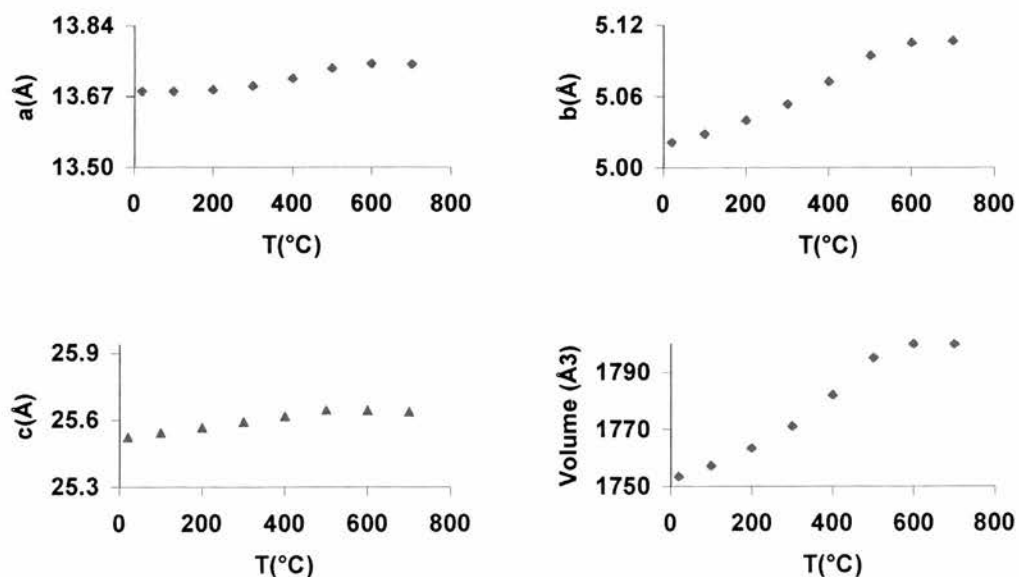


Figure 5.30 Thermal evolution of lattice parameters for CIT-5 (a) a axis (b) b axis (c) c axis and (d) Volume

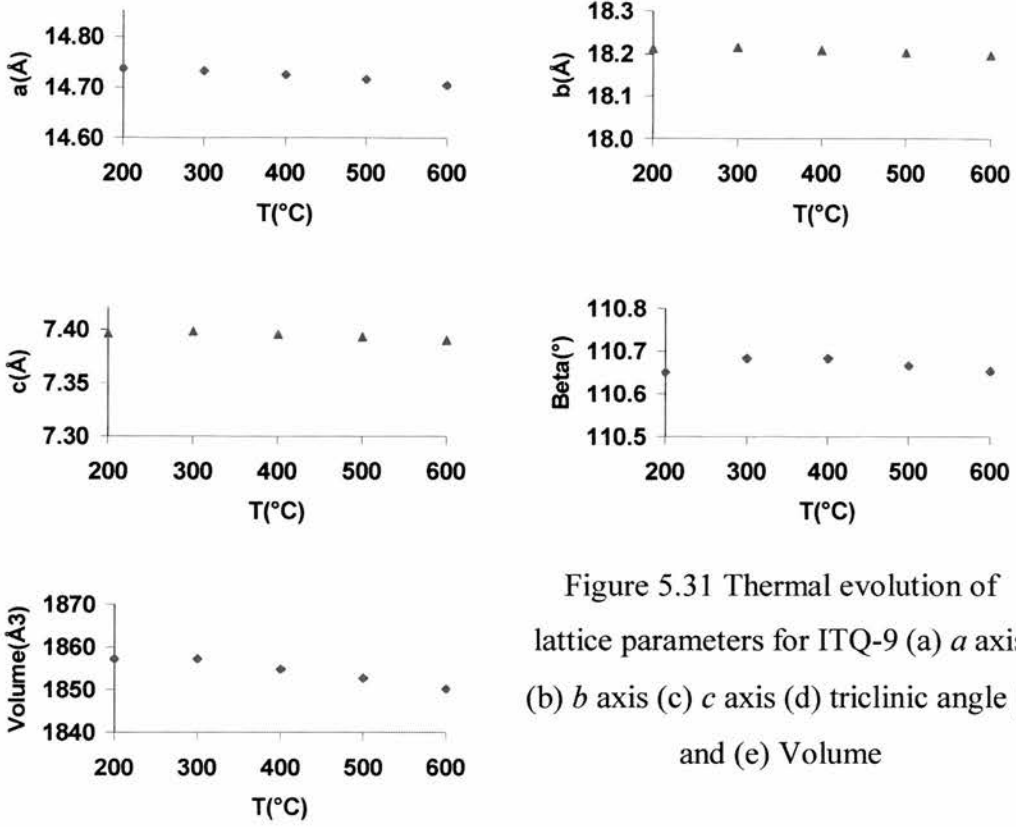


Figure 5.31 Thermal evolution of lattice parameters for ITQ-9 (a) *a* axis (b) *b* axis (c) *c* axis (d) triclinc angle β and (e) Volume

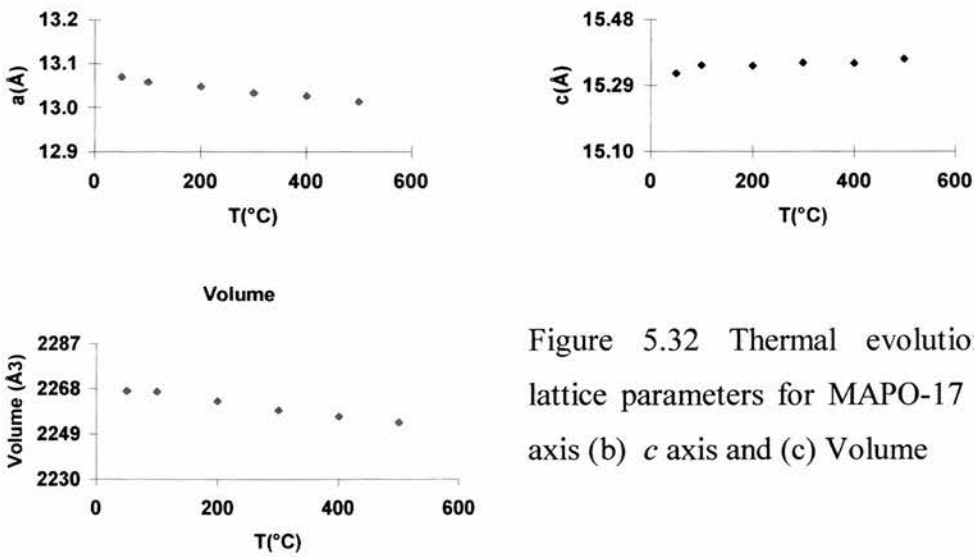


Figure 5.32 Thermal evolution of lattice parameters for MAPO-17 (a) *a* axis (b) *c* axis and (c) Volume

Table 5.6: Coefficients of thermal expansion for all materials studied

Sample	α_a	α_b	α_c	α_v	$1/3 \alpha_v$
ITQ-1*	-4.23	-4.23	-3.21	-12.1	-4.33
ITQ-3*	-0.29	-2.06	-10.1	-11.4	-3.80
SSZ-23*	-6.09	-3.21	-0.73	-10.3	-3.43
AIPO-31*	+9.72	+9.72	+17.3	+32.8	+10.9
ITQ-4 [§]	-11.5	-7.47	+7.19	-9.1	-3.03
ITQ-7	-2.28	-2.28	-1.05	-5.61	-1.87
ITQ-9	-5.58	-2.37	-2.19	-10.02	-3.34
CIT-5	+8.57	+28.2	+8.41	+14.9	+5.0
MAPO-17	-9.16	-9.16	+4.66	-4.57	-1.52
Chabazite [§]	-8.24	-8.24	-13.3	-28.5	-9.50

*determined over T range 323-773K using powder X-ray diffraction.

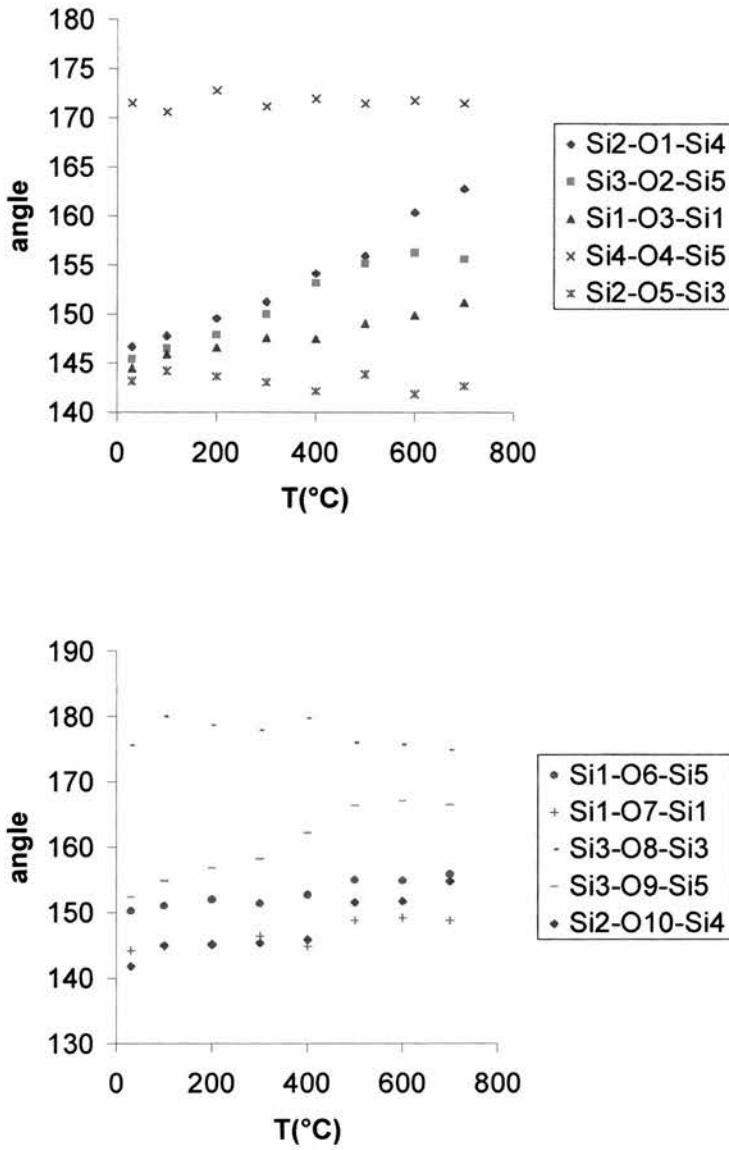
§ average CTE as expansivity was non linear

There are several interesting observations to be made from these experiments on ITQ-7, ITQ-9, CIT-5 and MAPO-17. ITQ-7, ITQ-9, and MAPO-17 all exhibit NTE. However, the contraction of MAPO-17 is not nearly as great as that of AIPO-17 which is one of the most contracting materials known over the temperature range 10-300K. This is either due to the higher temperature or the doping of Mg into the framework, which results in the presence of H⁺ groups attached to the bridging oxygens restricting bending of the bonds and hence contraction.

Secondly, Tschaufeser² predicted that it was necessary to have a network of either 2D or 3D channels for NTE to be possible. ITQ-9, like ITQ-4 has only 1D channels but exhibits weak NTE. However, both ITQ-4 and ITQ-9 have a very large micropore volume which was also suggested to be important. Both CIT-5 and AIPO-31 have 1D channels, but they showed a very strong volume expansion, driven by a strong axial expansion along their “short” (ca 5Å) axes. The short axes on ITQ-4 and ITQ-9 are approximately 7.4Å. Within ITQ-4 this axis expands and within ITQ-9 it contracts. A molecular modelling study would be required in order to ascertain the driving force causing these contrasting effects.

From these four samples only CIT-5 showed any clear trends in bonds and angles, despite the lower d spacings of Polaris available for studies of the complex (8T atoms) sample of ITQ-9.

The Si-O-Si angles are plotted in figures 5.33 and 5.34.



Figures 5.33 and 5.34: Thermal behaviour of the Si-O-Si angles in CIT-5

It can be clearly seen that the angles Si2-O1-Si4 and Si2-O10-Si4 vary the most. Figure 5.35 overleaf shows clearly that these angles are situated along the b axis and drive its expansivity.

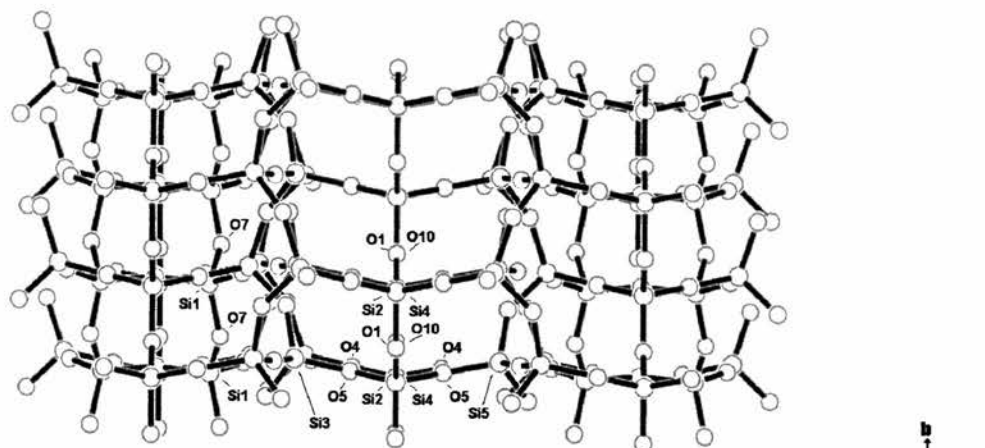


Figure 5.35: View down c axis showing layers

Also significant is the behaviour of Si3-O2-Si5, Si1-O3-Si1, Si1-O7-Si1 and Si3-O9-Si5. These angles can be seen in figure 5.36.

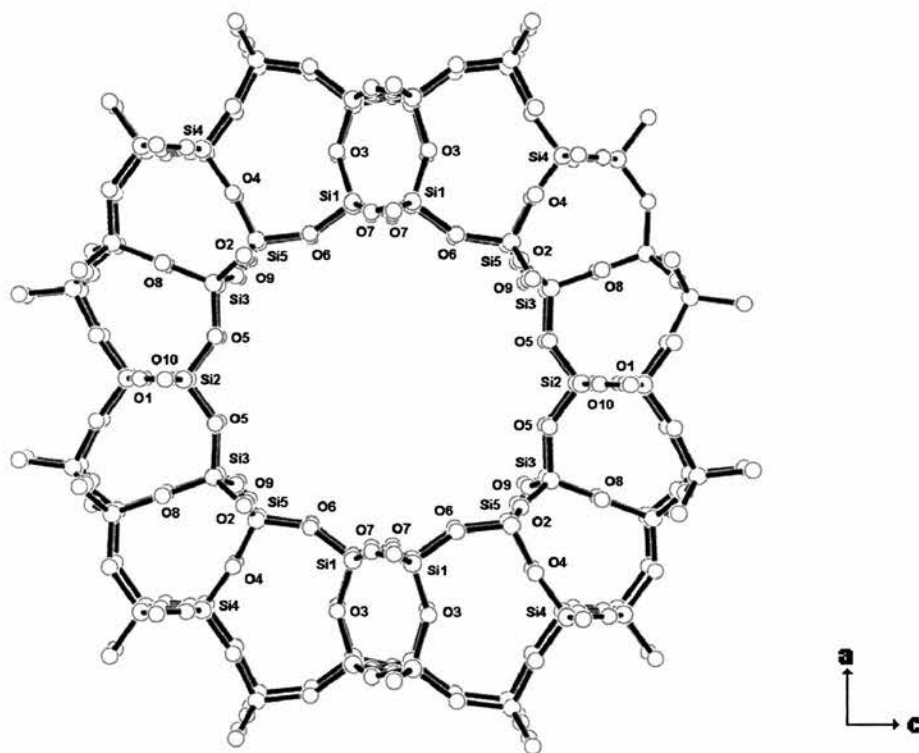


Figure 5.36: 14MR CIT-5 viewed down b axis

At first glance these angles appear to have little correlation with the b axis. However, the angle between each of the Si-Si vectors and the b axis has been calculated and the results shown in table 5.7.

Table 5.7: Angle away from b axis and overall change in angle

Angle	Description of location	Tilt from b axis of Si-Si vector	Overall change
Si2-O1-Si4	b axis	34.8°	+16.1°
Si3-O2-Si5	ring	35.2°	+10.2°
Si1-O3-Si1	bridging	34.6°	+6.7°
Si4-O4-Si5	bridging	78.8°	0°
Si2-O5-Si3	ring	78.8°	-0.5°
Si1-O6-Si5	ring	80.1°	+5.7°
Si1-O7-Si1	ring	34.6°	+4.6°
Si3-O8-Si3	bridging	88.7°	-0.7°
Si3-O9-Si5	ring	35.2°	+14.2°
Si2-O10-Si4	b axis	35.8°	+13°

The b axis expansion is driven by the behaviour of the angles Si2-O1-Si4, Si3-O2-Si5, Si1-O3-Si1, Si1-O7-Si1, Si3-O9-Si5 and Si2-O10-Si4 whereas the angles Si4-O4-Si5, Si2-O5-Si3, Si1-O6-Si5, and Si3-O8-Si3 lie almost perpendicular to the b axis on the ac plane. The a and c axis expansion is driven by the Si-O6-Si angle.

5.6: Chabazite: A Further Experiment

One issue which remained to be resolved was whether or not the thermal contraction was reversible - do the samples expand on cooling? A sample of chabazite was heated on the STOE furnace and then cooled. The resulting plots of unit cell parameters and volume vs. temperature are shown in figure 5.37 overleaf.

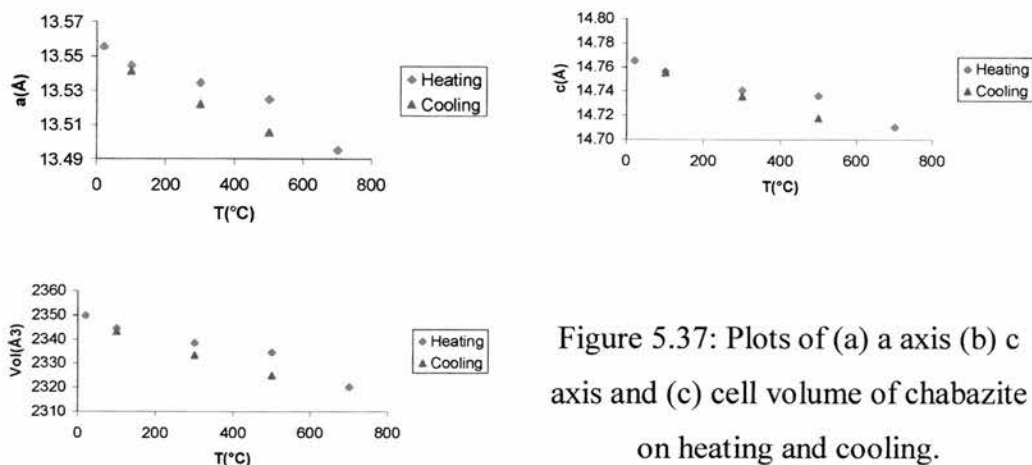


Figure 5.37: Plots of (a) a axis (b) c axis and (c) cell volume of chabazite on heating and cooling.

As can be seen, chabazite expands on cooling, so the contraction is not due to any irreversible structural change or annealing of defects occurring even though there is some slight hysteresis.

5.7: Overall Conclusion

The overall conclusion is that negative thermal expansion in microporous structures appears to be much more widespread than previously thought. Eight of the ten samples studied have shown negative axial thermal expansion and most of these have also shown a volume contraction.

Tschaufeser's prediction² that it was necessary to have a network of either 2D or 3D channels for NTE to be possible appears not to be true for both ITQ-9 and ITQ-4 which have only 1D channels but exhibit weak NTE. However, both ITQ-4 and ITQ-9 have a very large micropore volume which was also suggested to be important.

Neutron powder diffraction is a powerful enough technique to extract information about the behaviour of some structural parameters, although the Osiris instrument has only adequate resolution for simple structures. Polaris was able to determine the expansivity of ITQ-9 where X-ray diffraction had failed. For precise information on temperature factors, studies of single crystals would be required. Molecular modelling studies are necessary to explain the factor which is driving the large b axis expansion in ITQ-4, CIT-5 and AIPO-31. In

particular it would be interesting to find out why it is these “short” axes which expand the most.

5.8: References

- 1) J.M. Thomas, *Angew. Chem. Intl. Ed. Engl.*, 1988, **27**, 1673
- 2) P. Tschaufeser and S. C. Parker, *J. Phys. Chem.*, 1995, **99**, 10609
- 3) J. D. Gale, *J. Phys. Chem. B*, 1998, **102**, 5423
- 4) D. Taylor, *Br. Ceram. Trans. J.*, 1984, **83**, 5
- 5) P.R.L. Welche, V. Heine and M.T. Dove, *Phys. Chem. Minerals*, 1998, **26**, 63
- 6) M.B. Smirnov, *Phys. Rev. B*, 1999, **59**, 4036
- 7) S. H. Park, R. W. G. Kuntsleve, H. Graetsch and H. Gies, *Studies in Surface Science and Catalysis*, 1997, **105**, 1989
- 8) J. W. Couves, R. H. Jones, S. C. Parker, P. Tschaufeser and C. R. A. Catlow., *J. Phys.: Condens. Matter*, 1993, **5**, L329
- 9) A. Colantuano, S. Dal Vecchio, G. Mascolo and M. Pansini, *Thermochimica Acta*, 1997, **29**, 659
- 10) M. P. Attfield and A. W. Sleight, *Chem. Commun.*, 1998, 601
- 11) M. P. Attfield and A. W. Sleight, *Chem. Mater.*, 1998, **10**, 2013
- 12) M.T. Dove, *Phase Transitions*, 1997, **61**, 1
- 13) M. A. Cambor, A. Corma, M.-J. Díaz Cabañas and C. Baerlocher, *J. Phys. Chem. B.*, 1998, **102**, 44
- 14) M. A. Cambor, A. Corma, P. Lightfoot, L. A. Villaescusa and P. A. Wright, *Angew. Chem. Intl. Ed. Engl.*, 1997, **36**, 2659
- 15) M. A. Cambor, M.-J. Díaz Cabañas, J. Perez-Pariente, S. J. Teat, W. Clegg, I. J. Shannon, P. Lightfoot, P. A. Wright and R. E. Morris, *Angew. Chem. Intl. Ed. Engl.*, 1998, **37**, 2659
- 16) H.L. Zubowa, M. Richter, U. Roost, B. Parlitz and R. Fricke, *Catalysis Letters*, 1993, **19**, 67
- 17) A. C. Larson and R. B. Von Dreele, Los Alamos National Laboratory Report No. LA-UR-86-748, 1987

- 18) J. S. O. Evans, T. A. Mary and A. W. Sleight, *J. Solid State Chem.*, 1998, **137**, 148
- 19) J. S. O. Evans, T. A. Mary, T. Vogt, M. A. Subramanian and A. W. Sleight, *Chem. Mater.*, 1996, **8**, 2809
- 20) C. Y. Chen, L. W. Finger, R. C. Medrud, P. A. Crozier, I. Y. Chan, T. V. Harris and S.I. Jones, *Chem. Commun*, 1997, 1775
- 21) M.J. Diaz-Cabanas, P. A. Barrett and M. A. Camblor, *Chem. Commun*, 1998, **17**, 1881
- 22) P.A. Barrett, M.A. Camblor, A.Corma, R.H. Jones and L.A. Villaescusa, *J. Chem. Mater.*, 1998, **9**, 8, 1713
- 23) D. Martin and D. Engberg, *Physica B*, *in press*
- 24) L.A. Villaescusa, P. A. Barrett and M. A. Camblor, *Angew. Chem. Intl. Ed. Engl.*, 1999, **38**, 1997
- 25) L.A. Villaescusa, P. A. Barrett, M. A. Camblor and R.H. Jones, *J. Chem. Soc., Faraday Trans.*, 1998, **94**, 2475
- 26) P. A. Barrett, M.J. Diaz-Cabanas, M. A. Camblor and R.H. Jones *Chem. Commun*, 1998, **17**, 188
- 27) G.W. Noble, P. A. Wright, P. Lightfoot, R. E. Morris, K. J. Hudson, A. Kvik and H. Graafsma, *Angew. Chem. Intl. Ed. Engl.*, 1997, **36**, 81

5.9: Publications arising from this chapter

- 1) D. A. Woodcock, P. Lightfoot, P. A. Wright, L. A. Villaescusa, M.-J. Díaz Cabañas and M. A. Camblor, *J. Mater. Chem.*, 1999, **9**, 349
- 2) D. A. Woodcock, P. Lightfoot, L. A. Villaescusa, M.-J. Díaz Cabañas and M. A. Camblor, *Chem. Mater.*, 1999, **11**, 2508
- 3) D. A. Woodcock, M.J. Maple, P. Lightfoot, P. A. Wright, L. A. Villaescusa, M.-J. Díaz Cabañas, M. A. Camblor, D. Engberg and R.I. Smith, *J. Mater. Chem.*, in preparation

Chapter 6: Studies of $\text{NaTi}_2(\text{PO}_4)_3$ under elevated pressure

This chapter relates to an experiment carried out on the Polaris instrument at ISIS on a sample of $\text{NaTi}_2(\text{PO}_4)_3$ under elevated pressure in order to investigate the link between negative thermal expansion and pressure induced amorphisation.

6.1: Introduction

Some materials such as ice and silicon, which show negative thermal expansion over a limited temperature range transform to an amorphous phase under pressure. Recent computer simulations have suggested the possibility of a common origin between negative thermal expansion and pressure induced amorphisation¹ i.e. Rigid Unit Modes. ZrW_2O_8 has been modelled² and can accommodate a change in pressure by a coupled rotation of polyhedra requiring only changes in the highly flexible Zr-O-W bridging angles. At relatively low pressure (2kbar) it becomes unstable and goes through a transition to a structurally related orthorhombic phase³. The new phase is stable and transforms back to the cubic form by heating at 393K and ambient pressure. Shifts in atom positions up to 1Å occur. This orthorhombic phase has been modelled by Pryde et al who have confirmed the presence of both Rigid Unit Modes and quasi Rigid Unit Modes within the phase, and have predicted that it also shows NTE. A neutron powder diffraction study on ZrW_2O_8 has been carried out up to 80 kbar by Perottoni and da Jornada⁴. ZrW_2O_8 was found to begin to become amorphous at 15 kbar, providing a further example of the link between these properties.

Experiments on NaTP (Chapter 3) have shown a contraction of the a and b and expansion of the c axis on heating. The structure of NaTP is simple, which lends itself easily to studies using only a small sample volume such as in a pressure cell.

6.2: Experimental

The sample of NaTP was prepared as described previously in section 3.2. It was then loaded into a pressure cell on Polaris and the pressure increased to the desired pressure using helium gas. Data was collected through a window in the

pressure cell at 90° to the beam and measurements taken at 500 bar (77μAh), 1080 bar (966.9μAh), 2500 bar (265.3μAh) and 5420 bar (1074.2μAh). Due to erratic performance of the beam, the number of different temperatures was low and a consistent acquisition time was not possible. Refinements were carried out using the GSAS program and a typical refinement consisted of 23 variables, 3688 profile points and 876 reflections.

6.3: Results and Discussion

A Rietveld difference plot at 5420 bar is shown in figure 6.1 below.

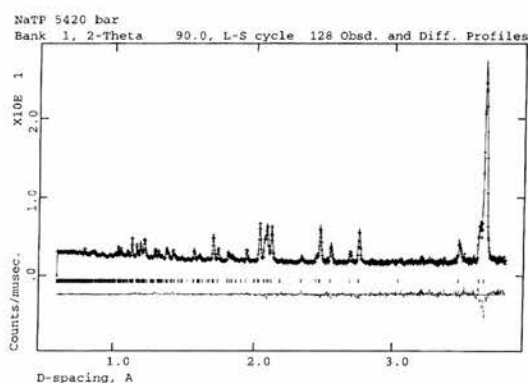


Figure 6.1: Rietveld plot for NaTP at 5420 bar

The resulting atomic co-ordinates at highest and lowest pressures are tabulated below and variation in lattice parameters shown in figure 6.2.

Table 6.1: Atomic co-ordinates for NaTP at 500bar and 5420 bar

Pressure = 500 bar

Space group = R-3c Lattice parameters $a = b = 8.481(1)\text{\AA}$ $c = 21.795(3)\text{\AA}$

Cell volume = $1357.7(3)\text{\AA}^3$

	Wyckoff site	x	y	z	Occupancy	$U_{\text{equiv}} \times 100$
Na	6b	0	0	0	1.0	1.6(5)
Ti	12c	0	0	.1449(7)	1.0	-0.28(23)
P	18e	.2880(9)	0	.25	1.0	-0.18(15)
O1	36f	.1747(9)	-.0241(7)	.1920(4)	1.0	0.83(13)
O2	36f	.1899(8)	.1633(9)	.0886(2)	1.0	0.72(12)

$$\chi^2 = 0.9080 \quad R_p = 0.1718 \quad R_{wp} = 0.0832$$

Pressure = 5420 bar

Space group = R-3c Lattice parameters a = b = 8.4730(4) Å c = 21.7390(13) Å

Cell volume = 1351.6(1) Å³

	Wyckoff site	x	y	z	Occupancy	U _{equiv} x 100
Na	6b	0	0	0	1.0	1.3(2)
Ti	12c	0	0	.1446(3)	1.0	-0.07(9)
P	18e	.2879(4)	0	.25	1.0	0.08(6)
O1	36f	.1758(3)	-.0223(3)	.1921(1)	1.0	0.71(5)
O2	36f	.1907(3)	.1627(3)	.0886(1)	1.0	0.58(4)

$$\chi^2 = 1.854 \quad R_p = 0.0564 \quad R_{wp} = 0.0293 \quad \text{Å}$$

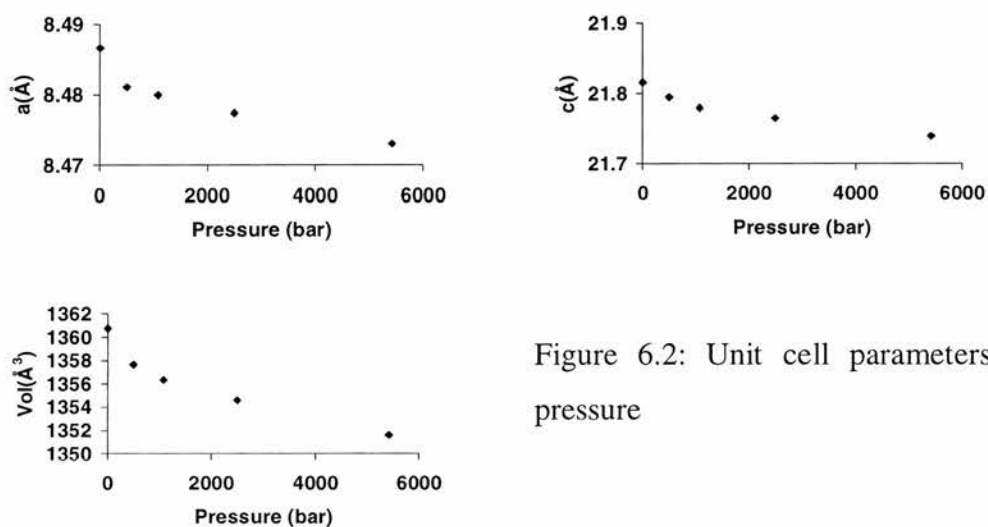


Figure 6.2: Unit cell parameters vs. pressure

The a and c axes do not contract by an equivalent amount. In order to quantify their contraction, a “pressure expansion coefficient” (the compressibility), p , has been calculated in the same manner as a thermal expansion coefficient, according to equation 6.1 below.

$$p = [(l_1 - l_0) / (p_1 - p_0)] / l_0 \quad (6.1)$$

where l_0 is the starting cell length, the l_1 finishing start length, p_0 the starting pressure and p_1 the finishing pressure.

The results are tabulated in Table 6.2 below. They do not include the first point at ambient pressure which was taken from Chapter 3 and does not correlate well with these results.

Table 6.2 – Axial and Volume Compressibilities of NaTi₂(PO₄)₃

p_a	$-2.36(5) \times 10^{-7} \text{bar}^{-1}$
p_c	$-4.58(5) \times 10^{-7} \text{bar}^{-1}$
p_v	$-11.02(7) \times 10^{-7} \text{bar}^{-1}$

It can clearly be seen that the contraction of the c axis is significantly greater than that of the a axis. If these contractions are equated to the equivalent temperature change required to effect them, the contraction of the a axis of 0.1% is equivalent to a 200°C temperature change (according to previous experiments) and the 0.25% change in the c axis equivalent to a 120°C temperature change. However, the main change on heating or cooling NaTP is the size of the MI site (filled with Na⁺ cations) aligned up the c axis. It increases or decreases by about 0.3 Å per 100° increase in temperature. However, the change in pressure does not effect as great a change at all. Table 6.3 below shows the size of the MI site for each pressure measured.

Table 6.3 – Variation of the Size of the MI Site with Pressure

Pressure (bar)	D (Å)
1*	3.899(5)
500	3.861(5)
1080	3.863(5)
2500	3.854(5)
5420	3.851(5)

* from previous experiments, Chapter 3

There is only a slight decrease in the size of this site – which is not of the same order as a thermal contraction induced by 100°C temperature decrease.

The Ti-O-P angles are also tabulated below as a measure of internal distortion. As can be seen, they contract slightly which is commensurate with a volume contraction, but only slightly.

Table 6.4: Variation of Ti-O-P Angles with Pressure

Pressure (bar)	Ti-O1-P($^\circ$)	Ti-O2-P($^\circ$)
1*	155.6(2)	146.6(2)
500	154.3(3)	145.1(3)
1080	155.2(3)	145.6(3)
2500	155.0(4)	145.4(4)
5420	154.8(3)	145.3(3)

* from previous experiments

The Alamo model has also been applied as a further measure of internal distortion. The results are plotted in figure 6.3. The changes in the parameters are similar to e.s.d.'s and generally indicate a slight shortening of bond lengths and contraction of angles. It is difficult to extract any clear evidence of polyhedral distortion due to the limited data available but comparison of the datasets at 1080 and 5420 bar, which are more complete due to a longer acquisition time reveal little change.

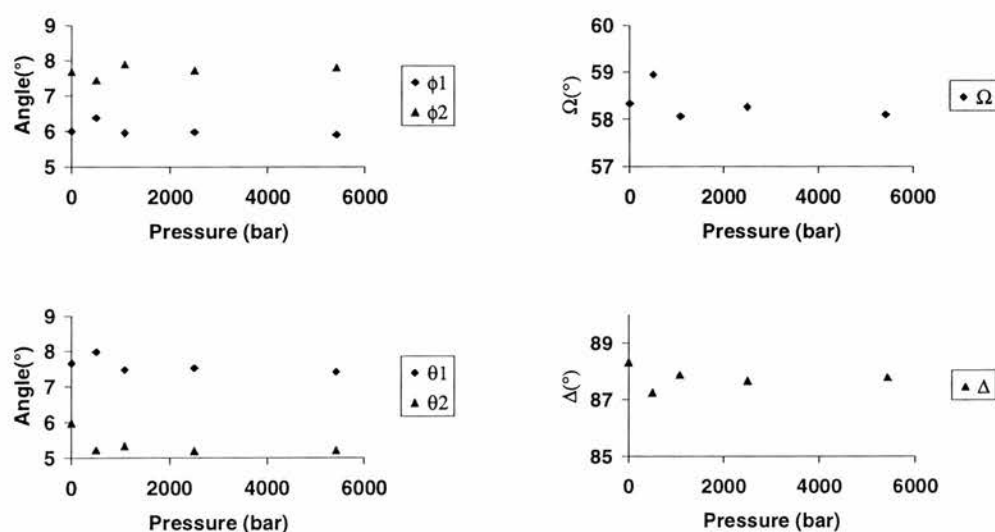


Figure 6.3: Variation in parameters for the Alamo model

6.4: Conclusion

NaTP itself does not show any sign of a change in structure when pressure is increased. There is only limited distortion of the structure, if any. This is possibly because it does not exhibit negative thermal expansion with regard to its volume, only a thermal contraction of its a axis expansion. A more promising candidate may be $\text{NbTi}(\text{PO}_4)_3$, discussed in Chapter 3 which does show a volume contraction. It is also possible that 5.4 kbar is too low a pressure to expect to see a change in structure. It was observed that the amorphisation of ZrW_2O_8 occurs at 15 kbar, which in itself is a low pressure to expect to see a full amorphisation of the structure. However, the phase change from cubic to orthorhombic in ZrW_2O_8 occurred at 2kbar which was well within the range of this study.

The c axis is found to be more compressible than the a axis. The contraction of the c axis is not entirely due to a contraction of the MI sites, unlike in the case of the thermal expansion of the c axis in NaTP , the bulk of which is caused by an expansion of these sites.

6.5: References

- 1) R. J. Speedy, *J. Phys. Condens. Matter*, 1996, **8**, 10907
- 2) A.K.A. Pryde, M. T. Dove and V. Heine, *J. Phys. Condens. Matter*, 1998, **10**, 8417
- 3) J.S.O. Evans, Z. Hu, J. D. Jorgensen, D.N. Argyriou, S. Short and A.W. Sleight, *Science*, 1997, **275**, 61
- 4) C. A. Perottoni and J. A. H. Jornada, *Science*, 1998, **280**, 886

Chapter 7: Conclusions and Further Work

7.1: Conclusions

The main aims of this work were to use X-ray and neutron powder diffraction to both identify new low and negative thermal expansion materials and to pinpoint the structural influences on the mechanism of their behaviour. Both of these objectives have been achieved. The following conclusions have been reached:

- The thermal expansion within the NZP system is driven by expansion of the M-O bond governing the size of the trigonal prismatic site along the c axis.
- Cation size is the dominant effect with both cation ordering and method of preparation appearing to be influential.
- $\text{NbTi}(\text{PO}_4)_3$ is a negative thermal expansion material.
- $\text{NaTi}_2(\text{PO}_4)_3$ did not reveal any phase change under increased pressure.
- $\text{Y}_2(\text{WO}_4)_3$ and $\text{Al}_2(\text{WO}_4)_3$ are both negative thermal expansion materials, with a larger cation resulting in an increased contraction.
- The pure silica zeolites ITQ-1, ITQ-3, SSZ-23, ITQ-4, ITQ-7, ITQ-9 and chabazite and the aluminophosphate MAPO-17 contract on heating and the pure silica zeolite CIT-5 and the aluminophosphate AIPO-31 expand.
- The NTE in chabazite is due to a contraction of the Si-O-Si bond angles both between and within the rings.
- CIT-5 expands strongly, especially along its short b axis. This is due to the behaviour of the angles along the b axis which drive its expansivity.
- Studies on chabazite showed that the material expanded on cooling, so the thermal contraction was not due to annealing of defects or water loss.
- A free isotropic refinement strategy was found to be most suitable than a rigid body refinement.
- Negative thermal expansion in microporous structures appears to be much more widespread than previously thought. Eight of the ten samples studied have shown negative axial thermal expansion and most of these have also shown a volume contraction.
- The experimental work presented in this study suggests the need for improved computer simulation techniques for modelling NTE behaviour.

7.2: Further Work

At the time this work began the field was limited to a small number of materials. The work by Sleight and others on ZrW_2O_8 has shown the way forward for more in depth studies on more recently discovered materials. In this work, the identification of the pure silica zeolites ITQ-1, ITQ-3, ITQ-4, chabazite and SSZ-23 and the NZP framework structure $\text{NbTi}(\text{PO}_4)_3$ as contracting have opened up a number of possibilities for further study. These are mainly connected with analysis of the Rigid Unit Modes, which have been identified as being at the core of thermal contraction and lattice dynamics studies.

For precise information on temperature factors, studies of single crystals would be required. Work by Evans on ZrW_2MoO_8 have used the temperature factors to great effect in analysis of its thermal contraction mechanism.

Some limited predictions were attempted on NaTP and SrTP using the program GULP. The main aim from this was to model the lattice parameters of the materials and to be able to draw conclusions about the electronic and potential effects involved. Unfortunately, these experiments proved unsuccessful with several different potential models failing. Both materials were predicted to show an isotropic expansion which is clearly at odds with the experimental data. There is great room for improvement in the correlation between modelling and experimental results: Tschaufeser's predictions on the TE of some microporous materials greatly underestimated the magnitude of the thermal contraction involved and Gale's study of SSZ-42 showed different behaviour to the experimental results on the isostructural material ITQ-4 reported here.

Negative thermal expansion has been suggested to be due to the materials having a negative Gruneisen parameter (β -eucryptite, ice) or Rigid Unit Modes (ZrW_2O_8 , β -quartz and zeolite rho). Inelastic neutron scattering could be used to detect the phonon modes and calculate the Gruneisen parameter for each of the materials. This would hopefully identify the vibrations influencing the TE. It would be advantageous to calculate the RUM spectrum for each of the materials and find out if RUMs are present in all of the contracting materials. Such measurements would hopefully reveal the direction that the RUMs are directing the contraction/expansion. This was successful in studies of orthorhombic

polyethylene and would be especially interesting in a comparison of AIPO-31 and CIT-5 to determine why the expansion of their short axes is so strong.

Two new aluminophosphates, STA-6 and STA-7, have recently been prepared. They have similar structures, although there is a key difference. STA-6 has a one dimensional channel structure, whereas STA-7 has three dimensional channels. A comparison of the TE of both of these materials would shed further light on Tschaufeser's prediction that NTE is more likely to be found if there are three dimensional channels. Thus STA-7 would be expected to contract more strongly. Preparation of an aluminophosphate version of chabazite would provide an interesting comparison to the strongly contracting pure silica material studied here. It would allow a more detailed understanding of the thermal expansion inherent to this structure type and perhaps allow a tailoring of the expansivity to other values. The effect of Si/Al ratios has already been studied by Cambor on sodalites and this work would provide it with a useful complement.

Appendices

The following appendices contain the experimentally determined atomic co-ordinates for all the materials where they were refined. In the case of ITQ-1, ITQ-3, SSZ-23, AlPO-31 and MAPO-17 these co-ordinates were not refined and the values used can be found in the literature as referred to previously.

Experimentally determined polynomial parameters are also provided where appropriate.

Appendix 1: Materials with the NZP (Nasicon Structure)

Table A1.1: Atomic co-ordinates and bond lengths for $\text{NaTi}_2(\text{PO}_4)_3$	124
Table A1.2: Atomic co-ordinates and bond lengths for $\text{Sr}_{0.5}\text{Ti}_2(\text{PO}_4)_3$	125
Table A1.3: Atomic co-ordinates and bond lengths for $\text{La}_{0.33}\text{Ti}_2(\text{PO}_4)_3$	126
Table A1.4: Atomic co-ordinates and bond lengths for $\text{NbTi}(\text{PO}_4)_3$	127
Table A1.5: Atomic co-ordinates and bond lengths for $\text{K}_{0.5}\text{Nb}_{0.5}\text{Ti}_{1.5}(\text{PO}_4)_3$	128
Table A1.6: Atomic co-ordinates and bond lengths for $\text{Ba}_{0.5}\text{Ti}_2(\text{PO}_4)_3$	129
Table A1.7: Atomic co-ordinates and bond lengths for $\text{Ca}_{0.25}\text{Sr}_{0.25}\text{Zr}_2(\text{PO}_4)_3$	130
Table A1.8: Experimentally determined polynomial parameters for $\text{Ba}_{0.5}\text{Ti}_2(\text{PO}_4)_3$, $\text{K}_{0.5}\text{Nb}_{0.5}\text{Ti}_{1.5}(\text{PO}_4)_3$ and $\text{Ca}_{0.25}\text{Sr}_{0.25}\text{Zr}_2(\text{PO}_4)_3$	132
Table A1.9: Atomic co-ordinates and bond lengths for $\text{LiTi}_2(\text{PO}_4)_3$	132
Table A1.10: Atomic co-ordinates and bond lengths for $\text{KTi}_2(\text{PO}_4)_3$	133
Table A1.11: Experimentally determined polynomial parameters for $\text{KTi}_2(\text{PO}_4)_3$ and $\text{LiTi}_2(\text{PO}_4)_3$	134

Appendix 2: Materials with the Scandium Tungstate Structure

Table A2.1 - Atomic co-ordinates and bond lengths for $\text{Al}_2(\text{WO}_4)_3$	135
Table A2.2 - Atomic co-ordinates and bond lengths for $\text{Y}_2(\text{WO}_4)_3$	136

Appendix 3: Microporous Materials

Table A3.1 Results from profile fit for Chabazite	138
Table A3.2: Experimentally determined atomic co-ordinates for chabazite	138
Table A3.3: Experimentally determined polynomial parameters for chabazite	139
Table A3.4: Experimentally determined atomic co-ordinates for ITQ-4	139
Table A3.5: Experimentally determined polynomial parameters for ITQ-4	140
Table A3.6 Experimentally determined atomic co-ordinates for CIT-5	140
Table A3.7 Experimentally determined atomic co-ordinates for ITQ-7	141
Table A3.8: Experimentally determined atomic co-ordinates for ITQ-9	143

Appendix 1: Materials with the Nasicon (NZP) Structure

Table A1.1: NaTi₂(PO₄)₃

T = 47°C

Space group R-3c

a = 8.4866(6)Å c = 21.8159(21)Å, Cell volume = 1360.74(19)Å³

	Wyckoff site	x	y	z	U _{equiv} x 100
Na	6b	0	0	0	5.2(10)
Ti	12c	0	0	0.1439(6)	-0.6(6)
P	18e	0.2892(10)	0	0.25	2.2(4)
O1	36f	0.1766(7)	-0.0228(6)	0.1929 (3)	1.14(25)
O2	36f	0.1900(8)	0.1626(8)	0.0894(2)	1.03(4)

R_{wp} = 0.0424 R_p = 0.0404 χ^2 = 2.485

Na-O2 x 6: 2.466(4)Å P-O1 x 2: 1.523(6)Å Ti-O1-P: 155.6(6)°

Ti-O1 x 3: 1.928(12)Å P-O2 x 2: 1.530(6)Å Ti-O2-P: 146.6(4)°

Ti-O2 x 3: 1.922(11)Å

T = 879°C

Space group R-3c

a = 8.4596(7)Å c = 22.1844(22)Å, Cell volume = 1374.91(21)Å³

	Wyckoff site	x	y	z	U _{equiv} x 100
Na	6b	0	0	0	18.0(18)
Ti	12c	0	0	0.1464(6)	2.0(6)
P	18e	0.2868(12)	0	0.25	2.5(5)
O1	36f	0.1691(8)	-0.0327(7)	0.1946 (3)	3.52(29)
O2	36f	0.1961(9)	0.0670(9)	0.0923(2)	2.86(29)

R_{wp} = 0.0454 R_p = 0.0434 χ^2 = 2.621

Na-O2 x 6: 2.569(5)Å P-O1 x 2: 1.517(7)Å Ti-O1-P: 153.6(6)°

Ti-O1 x 3: 1.914(12)Å P-O2 x 2: 1.500(7)Å Ti-O2-P: 149.8(5)°

Ti-O2 x 3: 1.960(12)Å

Table A1.2: Sr_{0.5}Ti₂(PO₄)₃

T = 25°C, Space group R-3

a = 8.2730(5)Å c = 22.5621(15)Å Cell volume = 1337.31(14)Å³

	Wyckoff site	x	y	z	U _{equiv} x 100
Sr	3a	0	0	0	5.1(11)
Ti1	6c	0	0	0.1509(9)	1.4(17)
Ti2	6c	0	0	0.6435(9)	1.4(17)
P	18f	0.2868(12)	0.0032(16)	0.2525(6)	0.3(4)
O1	18f	0.1846(19)	-0.0115(12)	0.1949(4)	-0.1(6)
O2	18f	0.0778(13)	-0.1409(21)	0.6978(4)	0.3(4)
O3	18f	0.1787(14)	0.1909(14)	0.0918(4)	0.1(6)
O4	18f	0.2138(16)	0.0707(13)	0.5990(3)	0.8(5)

R_{wp} = 0.0385 R_p = 0.0395 χ^2 = 3.812

Sr-O1 x 6: 3.291(10)Å Ti2-O4 x 3: 1.849(23)Å Ti1-O1-P: 152.7(11)°

Sr-O2 x 6: 2.574(10)Å P-O1: 1.528(16)Å Ti2-O2-P: 141.4(8)°

Ti1-O1 x 3: 1.853(27)Å P-O2: 1.510(18)Å Ti1-O3-P: 143.4(10)°

Ti2-O2 x 3: 2.018(25)Å P-O3: 1.494(12)Å Ti2-O4-P: 148.4(8)°

Ti1-O3 x 3: 2.038(28)Å P-O4: 1.540(16)Å

T=834°C

a = 8.3627(6)Å b = A c = 22.5590(17)Å Cell volume = 1366.29(18)Å³

	Wyckoff site	x	y	z	U _{equiv} x 100
Sr	3a	0	0	0	8.3(13)
Ti1	6c	0	0	0.1539(9)	5.2(23)
Ti2	6c	0	0	0.6421(9)	-9.0(13)
P	18f	0.3054(19)	0.0295(25)	0.2538(8)	1.8(7)
O1	18f	0.1787(21)	-0.0139(18)	0.2012(6)	1.0(7)
O2	18f	0.0683(18)	-0.1497(24)	0.6932(7)	2.4(6)
O3	18f	0.1727(19)	0.1682(17)	0.0922(5)	2.3(6)
O4	18f	0.2234(22)	0.0555(19)	0.5991(4)	4.6(7)

$R_{wp} = 0.0415$ $R_p = 0.0482$ $\chi^2 = 4.506$
 Sr-O1 x 6: 3.327(10)Å Ti2-O4 x 3: 1.909(28)Å Ti1-O1-P: 162.0(13)°
 Sr-O2 x 6: 2.631(9)Å P-O1: 1.459(18)Å Ti2-O2-P: 143.8(10)°
 Ti1-O1 x 3: 2.015(28)Å P-O2: 1.575(16)Å Ti1-O3-P: 155.3(13)°
 Ti2-O2 x 3: 2.007(28)Å P-O3: 1.538(16)Å Ti2-O4-P: 150.3(16)°
 Ti1-O3 x 3: 1.867(29)Å P-O4: 1.422(19)Å

Table A1.3: La_{0.33}Ti₂(PO₄)₃

T = 25°C, space group R-3,

a = 8.26988(9)Å. c = 22.3573(4)Å

	Wyckoff site	x	y	z	U _{equiv} x 100
La*	3a	0	0	0	0.033(3)
Ti1	6c	0	0	0.1469(5)	0.000(1)
Ti2	6c	0	0	0.6424(4)	0.000(1)
P	18f	0.2854(4)	0.0047(5)	0.2517(2)	0.002(6)
O1	18f	0.1801(5)	- 0.0143(4)	0.1930(2)	0.0079(7)
O2	18f	0.0762(4)	- 0.1438(5)	0.6966(2)	0.0101(7)
O3	18f	0.1710(5)	0.1902(5)	0.0907(1)	0.0025(6)
O4	18f	0.2188(5)	0.0767(4)	0.5993(1)	0.0014(6)

* 2/3 occupancy

$R_{wp} = 0.0399$ $R_p = 0.0402$ $\chi^2 = 3.899$
 La-O1 x 6: 3.3181(3)Å Ti2-O4 x 3: 1.85972(2)Å Ti1-O1-P: 153.436(0)°
 La-O2 x 6: 2.5219(3)Å P-O1: 1.53972(2)Å Ti2-O2-P: 141.460(0)°
 Ti1-O1 x 3: 1.86183(2)Å P-O2: 1.51517(2)Å Ti1-O3-P: 140.637(0)°
 Ti2-O2 x 3: 2.00753(2)Å P-O3: 1.54402(2)Å Ti2-O4-P: 147.713(0)°
 Ti1-O3 x 3: 1.95764(2)Å P-O4: 1.54870(2)Å

T = 300°C

a = 8.29811(16) Å, c = 22.3478(5) Å

	Wyckoff site	x	y	z	U _{equiv} x 100
La*	3a	0	0	0	0.037(3)
Ti1	6c	0	0	0.1484(5)	0.003(1)
Ti2	6c	0	0	0.6409(4)	0.003(1)
P	18f	0.2845(5)	0.0051(5)	0.2516(2)	0.0053(7)
O1	18f	0.1769(6)	-0.0178(5)	0.1933(2)	0.0124(8)
O2	18f	0.0721(5)	-0.1484(6)	0.6961(2)	0.0165(9)
O3	18f	0.1724(5)	0.1873(5)	0.0900(2)	0.0071(8)
O4	18f	0.2158(5)	0.0728(4)	0.5984(1)	0.0055(7)

*2/3 occupancy

R_{wp} = 0.0421 R_p = 0.047 $\chi^2 = 4.282$

La-O1 x 6: 3.2941(3)Å Ti2-O4 x 3: 1.84109(3)Å Ti1-O1-P: 152.643(0)°

La-O2 x 6: 2.50751(4)Å P-O1: 1.53779(3)Å Ti2-O2-P: 142.823(0)°

Ti1-O1 x 3: 1.84398(3)Å P-O2: 1.50097(2)Å Ti1-O3-P: 140.222(0)°

Ti2-O2 x 3: 2.03260(3)Å P-O3: 1.54793(3)Å Ti2-O4-P: 148.936(0)°

Ti1-O3 x 3: 1.98466(3)Å P-O4: 1.56102(3)Å

Table A1.4: NbTi (PO₄)₃

T = 25°C

Space group = R-3c Lattice parameters a = b = 8.5569(1)Å c = 21.9417(4)Å

Cell volume = 1391.34(4)Å³

	Wyckoff site	x	y	z	Occupancy	U _{equiv} x 100
Nb	12c	0	0	.14139(21)	0.5	0.23(5)
Ti	12c	0	0	.14139(21)	0.5	0.23(5)
P	18e	.28160(16)	0	.25	1.0	0.60(5)
O1	36f	.16567(14)	-.03212(13)	.19378(4)	1.0	1.46(5)
O2	36f	.19899(13)	.16793(14)	.09260(4)	1.0	1.21(5)

R_{wp} = 0.0277 R_p = 0.0325 $\chi^2 = 3.141$

Ti-O1 x 3: 1.952(3)Å P-O1 x 2: 1.517(1)Å Ti-O1-P: 155.5(1)°
 Ti-O2 x 3: 1.912(3)Å P-O2 x 2: 1.522(1)Å Ti-O2-P: 153.7(1)°

T = 800°C

Space group = R-3c Lattice parameters a = b = 8.54263(7)Å c = 21.9688 (3)Å

Cell volume = 1388.42(3)Å³

	Wyckoff site	x	y	z	Occupancy	U _{equiv} x 100
Nb	12c	0	0	.14185(26)	0.5	1.39(7)
Ti	12c	0	0	.14185(26)	0.5	1.39(7)
P	18e	.28243(18)	0	.25	1.0	1.45(7)
O1	36f	.16552(19)	-.03280(18)	.19423(5)	1.0	3.92(7)
O2	36f	.19964(17)	.16864(18)	.09285(5)	1.0	3.40(7)

R_{wp} = 0.0291 R_p = 0.0347 χ^2 = 3.251

Ti-O1 x 3: 1.949(4)Å P-O1 x 2: 1.516(1)Å Ti-O1-P: 155.4(2)°
 Ti-O2 x 3: 1.920(4)Å P-O2 x 2: 1.514(1)Å Ti-O2-P: 153.7(2)°

Table A1.5: K_{0.5}Nb_{0.5}Ti_{1.5}(PO₄)₃

Space group R-3c,

T = 20°C

a = 8.4330(2)Å, c = 22.7344(5)

	Wyckoff site	x	y	z	Occupancy	U _{equiv} x 100
K		0	0	0	0.5	2.46(9)
Nb	12c	0	0	0.1539(1)	0.25	0.57(9)
Ti	12c	0	0	0.1539(1)	0.75	0.57(7)
P	18e	0.2823(2)	0	0.25	1.0	0.39(6)
O1	36f	0.1580(2)	0.9528(2)	0.19671(5)	1.0	1.35(6)
O2	36f	0.1983(2)	0.1679(2)	0.09732(5)	1.0	1.28(6)

R_{wp} = 0.0301 R_p = 0.0687 χ^2 = 5.473

K-O2 x 6: 2.707(1)Å P-O1 x 2: 1.519(1)Å Ti-O1-P: 147.3(3)°
 Ti-O1 x 3: 1.846(7)Å P-O2 x 2: 1.523(1)Å Ti-O2-P: 152.5(3)°
 Ti-O2 x 3: 2.023(8)Å

T=700°C

a = 8.4282(2)Å c = 22.7626(7)Å

	Wyckoff site	x	y	z	Occupancy	U _{equiv} x 100
K	6b	0	0	0	0.5	7.88(9)
Nb	12c	0	0	0.1535(1)	0.25	2.57(9)
Ti	12c	0	0	0.1535(1)	0.75	2.57(9)
P	18e	0.2828(2)	0	0.25	1.0	1.00(9)
O1	36f	0.1581(2)	0.9524(2)	0.19715(7)	1.0	3.24(9)
O2	36f	0.1982(2)	0.1688(2)	0.09755(8)	1.0	3.03(9)

R_{wp} = 0.0233 R_p = 0.0448 χ^2 = 2.740

K-O2 x 6: 2.714(2)Å P-O1 x 2: 1.514(2)Å Ti-O1-P: 147.6(5)°
 Ti-O1 x 3: 1.859(1)Å P-O2 x 2: 1.519(2)Å Ti-O2-P: 153.0(5)°
 Ti-O2 x 3: 2.015(2)Å

Table A1.6: Ba_{0.5}Ti₂(PO₄)₃

Space group R-3c,

T =20 °C.

a = 8.3418(1)Å, c = 23.0101(4)Å

	Wyckoff site	x	y	z	Occupancy	U _{equiv} x 100
Ba	6b	0	0	0	0.5	2.78(8)
Ti	12c	0	0	0.1491(2)	1.0	0.67(8)
P	18e	0.2828(2)	0	0.25	1.0	0.39(6)
O1	36f	0.1551(2)	-0.0541(2)	0.19734(4)	1.0	1.71(5)
O2	36f	0.1969(2)	0.1674(2)	0.09845(4)	1.0	1.68(5)

R_{wp} = 0.0244 R_p = 0.0598 χ^2 = 4.107

Ba-O2 x 6: 2.736(1)Å P-O1 x 2: 1.525(1)Å Ti-O1-P: 147.4(9)°
 Ti-O1 x 3: 1.921(2)Å P-O2 x 2: 1.519(1)Å Ti-O2-P: 155.9(1)°
 Ti-O2 x 3: 1.929(2)Å

T= 800°C

a = 8.3667(3)Å, c = 23.0635(8)Å

	Wyckoff site	x	y	z	Occupancy	U _{equiv} x 100
Ba	6b	0	0	0	0.5	6.93(9)
Ti	12c	0	0	0.1478(3)	1.0	1.24(9)
P	18e	0.2828(3)	0	0.25	1.0	1.03(9)
O1	36f	0.1572(4)	-0.0525(3)	0.1976(1)	1.0	3.46(9)
O2	36f	0.1968(3)	0.1676(3)	0.0987(1)	1.0	3.47(9)

R_{wp} = 0.0290 R_p = 0.0645 χ^2 = 4.579

Ba-O2 x 6: 2.747(3)Å P-O1 x 2: 1.516(3)Å Ti-O1-P: 148.2(2)°
 Ti-O1 x 3: 1.954(5)Å P-O2 x 2: 1.526(2)Å Ti-O2-P: 157.0(2)°
 Ti-O2 x 3: 1.910(5)Å

Table A1.7: Ca_{0.25}Sr_{0.25}Zr₂(PO₄)₃

Space group R-3

T= 16°C a = 8.72452(3)Å c = 22.3573(4) Å

	Wyckoff site	x	y	z	Occ.	U _{equiv} x 100
Ca	3a	0	0	0	0.5	3.01(2)
Sr	3a	0	0	0	0.5	3.01(2)
Zr1	6c	0	0	0.1490(2)	1.0	1.39(2)
Zr2	6c	0	0	0.6433(2)	1.0	1.57(2)
P	18f	0.2922(4)	0.0086(5)	0.2524(2)	1.0	1.75(2)
O1	18f	0.1942(4)	0.0019(4)	0.1975(2)	1.0	2.39(3)
O2	18f	0.0584(4)	-0.1581(4)	0.6964(2)	1.0	2.69(3)
O3	18f	0.1794(4)	0.1788(4)	0.0866(2)	1.0	2.08(3)
O4	18f	-0.1653(4)	-0.2187(4)	0.5951(2)	1.0	2.47(3)

R_{wp} = 0.0771 R_p = 0.072 χ^2 = 1.923

Ca-O1 x 6: 2.551(3)Å P-O1: 1.508(5) Zr1-O1-P: 157.1(3)
 Zr1-O1 x 3: 2.027(4)Å P-O2: 1.513(5) Zr2-O2-P: 148.7(3)
 Zr2-O2 x 3: 2.092(4)Å P-O3: 1.536(5) Zr1-O3-P: 141.5(3)
 Zr1-O3 x 3: 2.116(4)Å P-O4: 1.498(4) Zr2-O4-P: 150.9(3)
 Zr2-O4 x 3: 2.061(4)Å

T = 800°C a = 8.7279(1) Å, c = 23.164(1)Å

	Wyckoff site	x	y	z	Occ.	U _{equiv} x 100
Ca	3a	0	0	0	0.5	9.65(3)
Sr	3a	0	0	0	0.5	9.65(3)
Zr1	6c	0	0	0.1496(2)	1.0	3.14(3)
Zr2	6c	0	0	0.6440(2)	1.0	3.13(3)
P	18f	0.2903(4)	0.0045(6)	0.2520(2)	1.0	3.32(3)
O1	18f	0.1902(5)	-0.0075(6)	0.1987(2)	1.0	5.58(4)
O2	18f	0.0532(6)	-0.1638(5)	0.6962(2)	1.0	6.06(4)
O3	18f	0.1831(5)	0.1755(4)	0.0880(2)	1.0	4.72(4)
O4	18f	-0.1688(5)	-0.2145(5)	0.5952(2)	1.0	5.48(4)

R_{wp} = 0.0524 R_p = 0.0504 χ^2 = 1.396

Ca-O1 x 6: 2.570(4) P-O1: 1.486(7) Zr1-O1-P: 157.0(3)
 Zr1-O1 x 3: 2.040(5) P-O2: 1.518(7) Zr2-O2-P: 148.9(4)
 Zr2-O2 x 3: 2.119(5) P-O3: 1.550(6) Zr1-O3-P: 142.4(4)
 Zr1-O3 x 3: 2.093(5) P-O4: 1.482(5) Zr2-O4-P: 152.8(4)
 Zr2-O4 x 3: 2.049(5)

Table A1.8: Experimentally determined polynomial parameters for $\text{Ba}_{0.5}\text{Ti}_2(\text{PO}_4)_3$, $\text{K}_{0.5}\text{Nb}_{0.5}\text{Ti}_{1.5}(\text{PO}_4)_3$ and $\text{Ca}_{0.25}\text{Sr}_{0.25}\text{Zr}_2(\text{PO}_4)_3$

Axis	p2	p1	p
a_{BaTP}	3.35×10^{-8}	2.81×10^{-6}	8.3423
c_{BaTP}	1.37×10^{-7}	-4.74×10^{-5}	23.012
Vol_{BaTP}	1.94×10^{-5}	-1.93×10^{-3}	1386.9
a_{KNTP}	-1.735×10^{-8}	-1.977×10^{-5}	8.4344
c_{KNTP}	7.798×10^{-8}	-1.336×10^{-5}	22.734
Vol_{KNTP}	1.0551×10^{-5}	-7.376×10^{-3}	1400.3
a_{CaSrZP}	4.31×10^{-9}	1.15×10^{-6}	8.7243
c_{CaSrZP}	4.51×10^{-8}	7.01×10^{-5}	23.08
$\text{Vol}_{\text{CaSrZP}}$	4.48×10^{-6}	5.03×10^{-3}	1521.3

Table A1.9: $\text{LiTi}_2(\text{PO}_4)_3$

T = 20°C. Space group R-3c, a = 8.51173(4)Å, c = 20.8524(2)Å

	Wyckoff site	x	y	z	Occupancy	$U_{\text{equiv}} \times 100$
Li	6b	0	0	0	0.76(3)	3.47\$
Ti	12c	0	0	0.1412(2)	1.0	0.43(1)
P	18e	0.2907(3)	0	0.25	1.0	0.80(1)
O1	36f	0.1841(3)	-0.0044(3)	0.1901(1)	1.0	1.31(1)
O2	36f	0.1896(3)	0.1643(2)	0.0805(1)	1.0	0.97(1)
Li	18e	-0.323(9)	0	0.25	0.08(1)	3.47\$

$$R_{\text{wp}} = 0.0715 \quad R_p = 0.0701 \quad \chi^2 = 1.963$$

\$Temperature factors on Li were constrained to be equal to those for equivalent temperatures for K in KTP to stabilise refinements.

$$\begin{array}{lll} \text{Li1-O2} \times 6: 2.264(2)\text{Å} & \text{Li2-O2}: 2.27(2)\text{Å} & \text{Ti-O1-P}: 158.0(6)^\circ \\ \text{Li2-O1}: 2.67(7)\text{Å} & \text{Ti-O1} \times 3: 1.886(4)\text{Å} & \text{Ti-O2-P}: 137.9(4)^\circ \\ \text{Li2-O1}: 2.72(7)\text{Å} & \text{Ti-O2} \times 3: 1.976(4)\text{Å} & \\ \text{Li2-O1}: 2.58(3)\text{Å} & \text{P-O1} \times 2: 1.533(3)\text{Å} & \\ \text{Li2-O2}: 2.73(9)\text{Å} & \text{P-O2} \times 2: 1.519(3)\text{Å} & \end{array}$$

T = 800°C. Space group R-3c, a = 8.51541(3)Å, c = 21.3547(1)Å

	Wyckoff site	x	y	z	Occupancy	U _{equiv} x 100
Li	6b	0	0	0	0.37(3)	8.90\$
Ti	12c	0	0	0.1417(2)	1.0	1.69(1)
P	18e	0.2878(3)	0	0.25	1.0	2.15(1)
O1	36f	0.1778(3)	-0.01804(3)	0.1914(1)	1.0	4.31(1)
O2	36f	0.1923(2)	0.1647(2)	0.0857(1)	1.0	3.70(1)
Li	18e	-0.2800(4)	0	0.25	0.21(1)	8.90\$

$$R_{wp} = 0.0653 \quad R_p = 0.0663 \quad \chi^2 = 2.111$$

Li1-O2 x 6: 2.388(2)Å Li2-O2: 2.39(2)Å Ti-O1-P: 156.9(6)°

Li2-O1: 2.34(3)Å Ti-O1 x 3: 1.917(3)Å Ti-O2-P: 144.2(4)°

Li2-O1: 2.56(3)Å Ti-O2 x 3: 1.944(3)Å

Li2-O1: 2.79(2)Å P-O1 x 2: 1.522(2)Å

Li2-O2: 2.83(9) Å P-O2 x 2: 1.521(2)Å

Table A1.10: KTi₂(PO₄)₃

T = 20°C. Space group R-3c, a = 8.35694(3)Å, c = 23.0724(2)Å

	Wyckoff site	x	y	z	U _{equiv} x 100
Na	6b	0	0	0	3.47(1)
Ti	12c	0	0	0.1490(2)	0.86(1)
P	18e	0.2827(3)	0	0.25	1.20(1)
O1	36f	0.1539(2)	-0.0549(2)	0.1975(1)	1.71(1)
O2	36f	0.1982(2)	0.1676(2)	0.0986(1)	1.80(1)

$$R_{wp} = 0.0805 \quad R_p = 0.0800 \quad \chi^2 = 3.275$$

K-O2 x 6: 2.749(2)Å P-O1 x 2: 1.530(2)Å Ti-O1-P: 147.4(2)°
 Ti-O1 x 3: 1.926(3)Å P-O2 x 2: 1.517(2)Å Ti-O2-P: 156.3(2)°
 Ti-O2 x 3: 1.933(3)Å

(b) at 800°C. Space group R-3c, a = 8.35431(2) Å, c = 23.19006(9)Å

	Wyckoff site	x	y	z	U _{equiv} x 100
K	6b	0	0	0	8.90(2)
Ti	12c	0	0	0.1498(2)	2.13(1)
P	18e	0.2835(2)	0	0.25	2.65(1)
O1	36f	0.1545(3)	-0.0551(2)	0.1980(1)	4.49(1)
O2	36f	0.1989(2)	0.1684(2)	0.0991(1)	4.43(1)

$$R_{wp} = 0.0647 \quad R_p = 0.0619 \quad \chi^2 = 2.278$$

Na-O2 x 6: 2.773(2)Å P-O1 x 2: 1.528(2)Å Ti-O1-P: 147.3(2)°
 Ti-O1 x 3: 1.929(3)Å P-O2 x 2: 1.510(2)Å Ti-O2-P: 156.8(2)°
 Ti-O2 x 3: 1.945(3)Å

Table A1.11: Experimentally determined polynomial parameters for $\text{KTi}_2(\text{PO}_4)_3$ and $\text{LiTi}_2(\text{PO}_4)_3$

Axis	p2	p1	p
a _{KTP}	3.0255E-08	-2.7662E-05	8.3513
c _{KTP}	2.0119E-08	1.3501E-04	23.069
Vol _{KTP}	1.22016E-05	-1.6061E-03	1395.4
a _{LiTP}	-2.5956E-09	6.471E-06	8.5112
c _{LiTP}	0	6.4172E-04	20.824
Vol _{LiTP}	1.0003E-05	3.3204E-02	1307.9

Appendix 2: Materials with the Scandium Tungstate Structure

Table A2.1 - Atom positions for $\text{Al}_2(\text{WO}_4)_3$

Space Group Pnca

T = 20°C

a = 9.1364(2)Å, b = 12.5913(3)Å, c = 9.0560(2)Å

	x	y	z	B*	Multiplicity
Al	0.4668(8)	0.3798(7)	0.2498(9)	0.6(1)	8d
W1	0.25	0	0.4750(8)	0.3(2)	4c
W2	0.1166(5)	0.3571(4)	0.3948(5)	0.3(2)	8d
O1	0.0900(4)	0.1405(4)	0.0878(5)	1.1(2)	8d
O2	0.1223(6)	0.0671(4)	0.3645(5)	1.3(2)	8d
O3	0.0055(4)	0.2572(4)	0.3172(6)	1.2(2)	8d
O4	0.3381(6)	0.4050(4)	0.0885(6)	1.1(2)	8d
O5	0.0697(5)	0.4791(4)	0.3210(6)	1.2(2)	8d
O6	0.3057(5)	0.3308(4)	0.3608(6)	1.2(2)	8d

$R_p = 6.55$ $R_{wp} = 8.88$ $\chi^2 = 3.09$

Al-O1: 1.870(7)Å

Al-O2: 1.881(7)Å

Al-O3: 1.863(7)Å

Al-O4: 1.902(7)Å

Al-O5: 1.919(7)Å

Al-O6: 1.885(7)Å

W1-O2: 1.754(5)Å

W1-O4: 1.771(5)Å

W2-O1: 1.765(5)Å

W2-O3: 1.762(5)Å

W2-O5: 1.729(5)Å

W2-O6: 1.787(5)Å

Al-O1-W2: 149.7(3)°

Al-O2-W1: 171.0(3)°

Al-O3-W2: 154.2(3)°

Al-O4-W1: 147.0(3)°

Al-O5-W2: 174.4(3)°

Al-O6-W2: 141.8(3)°

T = 800°C

a = 9.1267(4)Å, b = 12.6488(6)Å, c = 9.0546(4)Å

	x	y	z	B*	Multiplicity
Al	0.471(1)	0.382(1)	0.246(2)	1.9(2)	8d
W1	0.25	0	0.471(2)	1.4(2)	4c
W2	0.113(1)	0.355(1)	0.392(1)	1.4(2)	8d
O1	0.091(1)	0.138(1)	0.085(1)	3.8(3)	8d
O2	0.132(1)	0.070(1)	0.360(1)	4.8(3)	8d
O3	0.006(1)	0.257(1)	0.316(1)	3.5(2)	8d
O4	0.343(1)	0.410(1)	0.084(1)	3.1(2)	8d
O5	0.065(1)	0.480(1)	0.319(1)	3.8(3)	8d
O6	0.307(1)	0.336(1)	0.356(1)	3.4(2)	8d

$R_p = 6.96$ $R_{wp} = 9.56$ $\chi^2 = 3.72$,

* Equivalent isotropic temperature factor

Al-O1: 1.895(8)Å	W1-O2: 1.715(6)Å	Al-O1-W2: 150.9(4)°
Al-O2: 1.859(8)Å	W1-O4: 1.755(6)Å	Al-O2-W1: 165.2(4)°
Al-O3: 1.870(8)Å	W2-O1: 1.763(6)Å	Al-O3-W2: 153.1(4)°
Al-O4: 1.910(8)Å	W2-O3: 1.720(6)Å	Al-O4-W1: 150.3(4)°
Al-O5: 1.905(8)Å	W2-O5: 1.763(6)Å	Al-O5-W2: 175.3(4)°
Al-O6: 1.891(8)Å	W2-O6: 1.812(6)Å	Al-O6-W2: 146.0(4)°

Table A2.2 - Atom positions for $Y_2(WO_4)_3$

Space Group Pnca

T = 20°C

a = 10.070(1)Å, b = 13.937(1)Å, c = 9.980(1)Å

	X	y	z	B	Multiplicity
Y	0.470(1)	0.381(1)	0.250(1)	0.9(1)	8d
W1	0.25	0	0.475(1)	0.4(2)	4c
W2	0.113(1)	0.357(1)	0.392(1)	0.8(2)	8d
O1	0.089(1)	0.141(1)	0.066(1)	1.8(2)	8d
O2	0.139(1)	0.065(1)	0.371(1)	1.8(2)	8d
O3	0.016(1)	0.265(1)	0.319(1)	2.1(2)	8d
O4	0.339(1)	0.416(1)	0.075(1)	2.5(2)	8d
O5	0.066(1)	0.468(1)	0.324(1)	2.1(2)	8d
O6	0.284(1)	0.337(1)	0.356(1)	2.2(2)	8d

 $R_p = 7.34$ $R_{wp} = 9.26$ $\chi^2 = 1.77$

Y-O1: 2.213(8)Å	W1-O2: 1.772(6)Å	Y-O1-W2: 153.8(4)°
Y-O2: 2.221(8)Å	W1-O4: 1.781(6)Å	Y-O2-W1: 166.9(4)°
Y-O3: 2.198(8)Å	W2-O1: 1.764(6)Å	Y-O3-W2: 156.5(4)°
Y-O4: 2.239(8)Å	W2-O3: 1.768(6)Å	Y-O4-W1: 151.3(4)°
Y-O5: 2.263(8)Å	W2-O5: 1.751(6)Å	Y-O5-W2: 172.2(4)°
Y-O6: 2.232(8)Å	W2-O6: 1.778(6)Å	Y-O6-W2: 149.4(4)°

T = 800°C

a = 9.986(2)Å, b = 13.905(2)Å, c = 9.919(2)Å

	X	y	z	B	Multiplicity
Y	0.472(1)	0.384(1)	0.248(2)	1.7(1)	8d
W1	0.25	0	0.481(3)	1.9(2)	4c
W2	0.111(3)	0.358(2)	0.390(2)	2.4(2)	8d
O1	0.089(2)	0.140(2)	0.066(2)	2.4(2)	8d
O2	0.144(3)	0.066(2)	0.361(3)	4.7(2)	8d
O3	0.021(2)	0.266(2)	0.320(3)	5.1(2)	8d
O4	0.341(3)	0.421(2)	0.081(3)	5.7(2)	8d
O5	0.063(2)	0.462(2)	0.326(3)	4.5(2)	8d
O6	0.286(2)	0.342(2)	0.360(2)	3.7(2)	8d

 $R_p = 7.57$ $R_{wp} = 9.65$ $\chi^2 = 1.98$

Appendix 2: Materials with the Scandium Tungstate Structure

Y-O1: 2.209(9)Å
Y-O2: 2.147(9)Å
Y-O3: 2.251(9)Å
Y-O4: 2.168(9)Å
Y-O5: 2.305(9)Å
Y-O6: 2.244(9)Å

W1-O2: 1.834(7)Å
W1-O4: 1.736(7)Å
W2-O1: 1.762(7)Å
W2-O3: 1.714(7)Å
W2-O5: 1.647(7)Å
W2-O6: 1.781(7)Å

Y-O1-W2: 153.7(5)°
Y-O2-W1: 161.4(5)°
Y-O3-W2: 158.2(5)°
Y-O4-W1: 154.4(5)°
Y-O5-W2: 170.9(5)°
Y-O6-W2: 149.4(5)°

Appendix 3: Microporous Materials

Table A3.1 Results from Profile Fit for Chabazite

Temperature	Merit	Unrestrained	Soft constraints	Rigid body
293K	χ^2	5.840	5.874	6.684
293K	R_{wp}	0.0385	0.0385	0.0411
293K	R_p	0.0484	0.0484	0.0535
473K	χ^2	7.043	7.227	7.951
473K	R_{wp}	0.0626	0.0630	0.0666
473K	R_p	0.0639	0.0631	0.0661
673K	χ^2	1.808	1.864	2.207
673K	R_{wp}	0.0552	0.0554	0.0610
673K	R_p	0.0522	0.0610	0.0558
773K	χ^2	2.265	2.332	2.533
773K	R_{wp}	0.0610	0.0613	0.0645
773K	R_p	0.0601	0.0601	0.0627
873K	χ^2	1.970	2.073	2.269
873K	R_{wp}	0.0567	0.0573	0.0609
873K	R_p	0.0495	0.0492	0.0522

Table A3.2: Experimentally Determined Atomic Co-ordinates for Chabazite

Space group = R-3m

T = 293K

a = 13.5252(3)Å, c = 14.7342(5)Å, Volume = 2334.3(1) Å³

	x	y	z	Ui/Ue*100	Multiplicity
Si	0.2275(4)	0.0009(5)	0.1030(3)	3.7(2)	36i
O1	0.1188(2)	-0.1188(2)	0.1299(3)	-0.17(6)	18h
O2	0.3333	0.0213(3)	0.1667	-0.17(6)	18g
O3	0.1962(4)	0.0981(2)	0.1206(3)	-0.17(6)	18h
O4	0.2592(3)	0	0	-0.17(6)	18f

T = 873K

a = 13.4661(4)Å, c = 14.6395(6)Å, Volume = 2299.0(1) Å³

	x	y	z	Ui/Ue*100	Multiplicity
Si	0.2287(5)	0.0034(5)	0.0988(4)	3.7(2)	36i
O1	0.1204 (2)	-0.1204(2)	0.1314 (3)	1.94(8)	18h
O2	0.3333	0.0209(3)	0.1667	1.94(8)	18g
O3	0.1964(4)	0.0982(2)	0.1195(3)	1.94(8)	18h
O4	0.2615(3)	0	0	1.94(8)	18f

Table A3.3: Experimentally Determined Polynomial Parameters for Chabazite

Axis	p2	p1	p
a	-1.200×10^{-7}	-2.833×10^{-5}	13.526
c	-3.553×10^{-7}	6.862×10^{-5}	14.73
Vol	-9.670×10^{-5}	7.587×10^{-4}	2334

Table A3.4: Experimentally Determined Atomic Co-ordinates for ITQ-4

Space group = I 2/m

T = 95K

a = 18.6876(5)Å, b = 13.5244(3)Å, c = 7.6155(2)Å

Beta = 102.142(2) Volume = 1881.67(7)

	x	y	z	Ui/Ue*100	Multiplicity
Si1	-0.0145(3)	0.1074(3)	0.2763(8)	-0.72(9)	8j
Si2	0.2483(3)	0.1112(5)	0.6223(9)	-0.72(9)	8j
Si3	0.1454(4)	0.1092(4)	0.2480(8)	-0.72(9)	8j
Si4	0.1626(4)	0.2080(5)	-0.1064(7)	-0.72(9)	8j
O1	0.3198(2)	0.1809(3)	0.6350(6)	-0.83(5)	8j
O2	-0.0769(4)	0.1850(4)	0.1940(6)	-0.83(5)	8j
O3	0	0.1205(4)	0.5	-0.83(5)	4h
O4	0.0614(3)	0.1337(3)	0.2234(5)	-0.83(5)	8j
O5	0.1566(4)	0	0.2067(8)	-0.83(5)	4i
O6	0.1861(3)	0.1416(3)	0.4486(5)	-0.83(5)	8j
O7	-0.0404(3)	0	0.2335(8)	-0.83(5)	4i
O8	0.2123(2)	0.1338(3)	0.7989(6)	-0.83(5)	8j
O9	0.2691(3)	0	0.6233(9)	-0.83(5)	4i
O10	0.1796(2)	0.1812(3)	0.1077(6)	-0.83(5)	8j

T=510K

a = 18.6013(5)Å, b = 13.4836(3)Å, c = 7.6372(2)Å

Beta = 101.854(2) Volume = 1874.67(7)

	x	y	z	Ui/Ue*100	Multiplicity
Si1	-0.0098(4)	0.1093(4)	0.2861(8)	0.2(1)	8j
Si2	0.2505(4)	0.1082(5)	0.6239(9)	0.2(1)	8j
Si3	0.1469(4)	0.1094(5)	0.2454(8)	0.2(1)	8j
Si4	0.1602(4)	0.2047(5)	-0.1156(7)	0.2(1)	8j
O1	0.3203(3)	0.1838(3)	0.6460(7)	0.55(6)	8j
O2	-0.0751(3)	0.1850(4)	0.1975(8)	0.55(6)	8j
O3	0	0.1211(5)	0.5	0.55(6)	4h
O4	0.0643(3)	0.1389(3)	0.2311(6)	0.55(6)	8j
O5	0.1557(4)	0	0.1990(8)	0.55(6)	4i
O6	0.1939(3)	0.1429(4)	0.4364(6)	0.55(6)	8j
O7	-0.0323(4)	0	0.2379(9)	0.55(6)	4i
O8	0.2076(3)	0.1311(3)	0.7801(6)	0.55(6)	8j
O9	0.2717(4)	0	0.6263(1)	0.55(6)	4i
O10	0.1797(3)	0.1787(4)	0.0967(6)	0.55(6)	8j

Table A3.5: Experimentally Determined Polynomial Parameters for ITQ-4

Axis	p2	p1	p
a	0	-2.154×10^{-4}	18.712
b	2.529×10^{-7}	-2.489×10^{-4}	13.545
c	-1.310×10^{-7}	1.314×10^{-4}	7.604
Vol	-1.256×10^{-5}	-9.862×10^{-3}	1882.9

Table A3.6 Experimentally Determined Atomic Co-ordinates for CIT-5

Space group I m 2 a

T=30°C

a = 13.6824(2) b = 5.0214(1) c = 25.5223(4)

Cell volume = 1753.50(4)

	x	y	z	Ui/Ui*100	Multiplicity
Si1	0.6382(3)	0.5063(1)	0.7162(2)	-0.47(8)	8c
Si2	0.25	0.018(1)	0.5241(3)	-0.47(8)	4b
Si3	0.4590(4)	-0.0988(9)	0.5580(2)	-0.47(8)	8c
Si4	0.25	0.5223(1)	0.4569(3)	-0.47(8)	4b
Si5	0.5549(4)	0.4081(9)	0.6054(2)	-0.47(8)	8c
O1	0.25	0.3216(9)	0.5025(2)	0.44(5)	4b
O2	0.4758(3)	-0.3873(9)	0.5820(2)	0.44(5)	8c
O3	0.75	0.4774(9)	0.6979(2)	0.44(5)	4b
O4	0.6566(3)	0.4700(9)	0.5781(2)	0.44(5)	8c
O5	0.3444(3)	-0.0357(9)	0.5601(2)	0.44(5)	8c
O6	0.5689(3)	0.4463(9)	0.6669(2)	0.44(5)	8c
O7	0.6159(3)	0.7996(9)	0.7375(2)	0.44(5)	8c
O8	0.5	-0.0868(9)	0.5	0.44(5)	4b
O9	0.5180(3)	0.1130(9)	0.5928(2)	0.44(5)	8c
O10	0.25	0.3286(9)	0.0265(3)	0.44(5)	4b

$$\chi^2 = 3.458 \quad R_{wp} = 0.0614 \quad R_p = 0.127$$

T=700°C

a = 13.7481(3) b = 5.1068(1) c = 25.6350(7)

Cell volume = 1799.81(7)

	x	y	z	U _i /U _e *100	Multiplicity
Si1	0.6390(4)	0.4683(9)	0.7177(3)	3.7(2)	8c
Si2	0.25	-0.0076(9)	0.5253(3)	3.7(2)	4b
Si3	0.4599(5)	-0.0568(9)	0.5574(2)	3.7(2)	8c
Si4	0.25	0.4953(9)	0.4563(4)	3.7(2)	4b
Si5	0.5515(5)	0.4494(9)	0.6061(3)	3.7(2)	8c
O1	0.25	0.2713(9)	0.4982(4)	3.1(1)	4b
O2	0.4889(7)	-0.3055(9)	0.5910(4)	3.1(1)	8c
O3	0.75	0.4668(9)	0.7023(3)	3.1(1)	4b
O4	0.6544(4)	0.4847(9)	0.5783(2)	3.1(1)	8c
O5	0.3436(4)	-0.0422(9)	0.5601(2)	3.1(1)	8c
O6	0.5742(4)	0.4366(9)	0.6664(2)	3.1(1)	8c
O7	0.6103(4)	0.7358(9)	0.7449(4)	3.1(1)	8c
O8	0.5	-0.0705(9)	0.5	3.1(1)	4b
O9	0.4974(7)	0.1948(9)	0.5875(4)	3.1(1)	8c
O10	0.25	0.2821(9)	0.0204(4)	3.1(1)	4b

 $\chi^2 = 4.181$ $R_{wp} = 0.0556$ $R_p = 0.0586$ **Table A3.7: Experimentally Determined Atomic Co-ordinates for ITQ-7**Space group P 4₂/m m c

T = 60°C

a = 12.8474(2) c = 25.2035(5)

Cell volume = 4160.0(1)

	x	y	z	U _i /U _e *100	Multiplicity
Si1	0.1177(5)	0.1171(5)	0.0629(3)	1.4(2)	16r
Si2	0.3046(5)	0.2479(5)	0.9044(3)	1.4(2)	16r
Si3	0.5	0.1204(5)	0.0623(3)	1.4(2)	8p
Si4	0.3808(5)	0.3828(5)	0.1874(2)	1.4(2)	16r
Si5	0.3775(5)	0.3828(6)	0	1.4(2)	8q
O1	0.1413(8)	0.1288(9)	0	1.35(6)	8q
O2	0.1356(8)	0	0.0792(5)	1.35(6)	8o
O3	0	0.1465(9)	0.0743(4)	1.35(6)	8o
O4	0.1979(5)	0.1916(6)	0.0914(3)	1.35(6)	16r
O5	0.3979(4)	0.1633(5)	0.9106(3)	1.35(6)	16r
O6	0.3212(6)	0.3319(6)	0.9495(2)	1.35(6)	16r
O7	0.3151(6)	0.3026(6)	0.8475(3)	1.35(6)	16r
O8	0.5	0	0.0756(5)	1.35(6)	4i
O9	0.5	0.1372(9)	0	1.35(6)	4k
O10	0.5	0.3795(9)	0	1.35(6)	4k
O11	0.3390(9)	0.5	0	1.35(6)	4m
O12	0.3571(5)	0.3571(5)	0.25	1.35(6)	8n
O13	0.5	0.3617(9)	0.1770(4)	1.35(6)	8p
O14	0.3508(9)	0.5	0.1770(4)	1.35(6)	8p

$$\chi^2 = 5.610 \quad R_{wp} = 0.0661 \quad R_p = 0.0676$$

$$T=600^\circ\text{C}, a = 12.8318(3) \quad c = 25.1831(9),$$

$$\text{Cell volume} = 4146.5(2)$$

	x	y	z	Ui/Ue*100	Multiplicity
Si1	0.1141(7)	0.1171(6)	0.0629(3)	1.7(2)	16r
Si2	0.3037(7)	0.2509(8)	0.9064(4)	1.7(2)	16r
Si3	0.5	0.1204(7)	0.0627(4)	1.7(2)	8p
Si4	0.3801(7)	0.3818(7)	0.1875(3)	1.7(2)	16r
Si5	0.3805(8)	0.3773(6)	0	1.7(2)	8q
O1	0.1286(9)	0.1380(9)	0	1.35(6)	8q
O2	0.1295(9)	0	0.0751(7)	1.35(6)	8o
O3	0	0.1562(9)	0.0763(7)	1.35(6)	8o
O4	0.1965(8)	0.1934(9)	0.0920(4)	1.35(6)	16r
O5	0.3982(6)	0.1698(8)	0.9123(4)	1.35(6)	16r
O6	0.3143(9)	0.3387(8)	0.9502(3)	1.35(6)	16r
O7	0.3128(9)	0.3013(9)	0.8488(4)	1.35(6)	16r
O8	0.5	0	0.0769(9)	1.35(6)	4i
O9	0.5	0.1382(9)	0	1.35(6)	4k
O10	0.5	0.3458(9)	0	1.35(6)	4k
O11	0.3748(9)	0.5	0	1.35(6)	4m
O12	0.3573(7)	0.3573(7)	0.25	1.35(6)	8n
O13	0.5	0.3548(9)	0.1796(6)	1.35(6)	8p
O14	0.3659(9)	0.5	0.1758(4)	1.35(6)	8p

$$\chi^2 = 5.900 \quad R_{wp} = 0.0604 \quad R_p = 0.0578$$

Table A3.8: Experimentally Determined Atomic Co-ordinates for ITQ-9

Space group = I -1

T=200°C

a = 14.7375(8) b = 18.2174(9) c = 7.3942(4)

 $\alpha = 89.736(5)$ $\beta = 110.684(5)$ $\gamma = 90.300(6)$,

Cell volume = 1857.2(2)

	x	y	z	U _i /U _e *100	Multiplicity
Si1	0.3922(4)	0.2493(4)	0.9843(9)	0.0(1)	4i
Si2	-0.3897(5)	0.2495(4)	-0.9576(9)	0.0(1)	4i
Si3	0.8891(5)	0.1550(4)	-0.1798(9)	0.0(1)	4i
Si4	-0.9057(6)	0.1546(4)	0.1469(9)	0.0(1)	4i
Si5	0.6433(4)	0.4994(3)	0.2593(9)	0.0(1)	4i
Si6	0.7812(5)	0.1587(4)	0.0833(9)	0.0(1)	4i
Si7	-0.7838(5)	0.1555(4)	-0.1095(9)	0.0(1)	4i
Si8	0.9198(5)	-0.0034(5)	-0.3021(9)	0.0(1)	4i
O1	0.3929(7)	0.2897(6)	0.1765(9)	0.39(6)	4i
O2	-0.3814(7)	0.3022(5)	-0.1258(9)	0.39(6)	4i
O3	0.9896(5)	0.1747(6)	-0.0123(9)	0.39(6)	4i
O4	0.6235(6)	0.4940(6)	0.0343(7)	0.39(6)	4i
O5	0.8855(6)	0.0690(4)	-0.2195(9)	0.39(6)	4i
O6	0.8618(9)	0.0777(4)	0.1458(9)	0.39(6)	4i
O7	0.7998(6)	0.0733(3)	0.1364(9)	0.39(6)	4i
O8	-0.7946(6)	0.0687(3)	-0.2195(9)	0.39(6)	4i
O9	0.6710(5)	0.1772(4)	0.0497(9)	0.39(6)	4i
O10	-0.6724(5)	0.1772(4)	-0.0451(9)	0.39(6)	4i
O11	0.8027(5)	0.1778(4)	-0.1094(9)	0.39(6)	4i
O12	-0.8248(6)	0.1763(6)	0.0563(9)	0.39(6)	4i
O13	0.3452(7)	0.3046(5)	0.8073(9)	0.39(6)	4i
O14	-0.3480(7)	0.2910(4)	-0.7554(9)	0.39(6)	4i
O15	0.4994(4)	0.2285(4)	0.9990(9)	0.39(6)	4i
O16	0.5369(4)	0.5015(6)	0.2728(9)	0.39(6)	4i

$$\chi^2 = 2.602 \quad R_{wp} = 0.0727 \quad R_p = 0.1033$$

T=600°C

a = 14.7034(7) b = 18.1976 (9) c = 7.3871(4)

$\alpha = 89.988(9)$ $\beta = 110.636(5)$ $\gamma = 90.093(9)$

Cell volume = 1849.7(2)

	x	y	z	U _i /U _e *100	Multiplicity
Si1	0.3925(4)	0.2541(4)	0.9728(9)	0.0(1)	4i
Si2	-0.3898(5)	0.2456(4)	-0.9716(9)	0.0(1)	4i
Si3	0.9008(6)	0.1551(5)	-0.1653(9)	0.0(1)	4i
Si4	-0.8913(7)	0.1518(6)	0.1617(9)	0.0(1)	4i
Si5	0.6437(4)	0.5003(4)	0.2540(9)	0.0(1)	4i
Si6	0.7822(5)	0.1606(5)	0.0943(9)	0.0(1)	4i
Si7	-0.7837(5)	0.1540(4)	-0.1043(9)	0.0(1)	4i
Si8	0.9218(5)	-0.0043(5)	-0.2952(9)	0.0(1)	4i
O1	0.3874(8)	0.2949(7)	0.1609(9)	0.39(6)	4i
O2	-0.3880(8)	0.2972(7)	-0.1458(9)	0.39(6)	4i
O3	0.0081(6)	0.1680(6)	-0.0131(9)	0.39(6)	4i
O4	0.6271(7)	0.5040(7)	0.0281(7)	0.39(6)	4i
O5	0.8874(7)	0.0704(5)	-0.2214(9)	0.39(6)	4i
O6	0.8080(9)	0.0774(4)	0.1620(9)	0.39(6)	4i
O7	0.8067(7)	0.0763(3)	0.1586(9)	0.39(6)	4i
O8	-0.7893(7)	0.0666(3)	-0.1316(9)	0.39(6)	4i
O9	0.6680(5)	0.1720(5)	0.0246(9)	0.39(6)	4i
O10	-0.6779(5)	0.1844(5)	-0.0757(9)	0.39(6)	4i
O11	0.8230(7)	0.1790(5)	-0.0737(9)	0.39(6)	4i
O12	-0.8079(6)	0.1768(7)	0.0820(9)	0.39(6)	4i
O13	0.3615(7)	0.3106(5)	0.7946(9)	0.39(6)	4i
O14	-0.3364(7)	0.2868(4)	-0.7721(9)	0.39(6)	4i
O15	0.5009(4)	0.2275(4)	0.0073(9)	0.39(6)	4i
O16	0.5381(4)	0.5038(8)	0.2679(9)	0.39(6)	4i

$$\chi^2 = 2.421 \quad R_{wp} = 0.0676 \quad R_p = 0.0891$$